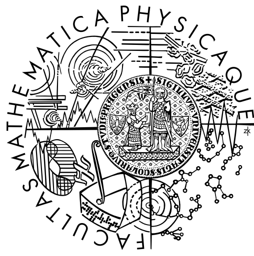

FACULTY
OF MATHEMATICS
AND PHYSICS
Charles University

DOCTORAL THESIS

Michal Zanáška

Probe methods for diagnostics of plasmatic systems for deposition of thin films

Department of Surface and Plasma Science

Supervisor of the doctoral thesis: prof. RNDr. Milan Tichý, DrSc.
Study programme: Physics
Study branch: Physics of Plasma and Ionized Media

Prague 2019

I declare that I carried out this doctoral thesis independently, and only with the cited sources, literature and other professional sources.

I understand that my work relates to the rights and obligations under the Act No. 121/2000 Sb., the Copyright Act, as amended, in particular the fact that the Charles University has the right to conclude a license agreement on the use of this work as a school work pursuant to Section 60 subsection 1 of the Copyright Act.

In .... date .... signature of the author

In the first place, I would like to thank my supervisor prof. RNDr. Milan Tichý, DrSc. for his guidance and constant support throughout my studies and work on the thesis. I am also grateful to doc. Mgr. Pavel Kudrna, Dr. for his willingness to always help with solving various experimental problems. I would like to express my gratitude to Mgr. Zdeněk Hubička, Ph.D. for fruitful discussions and for directing me to several ideas including also the idea of the in-situ impedance spectroscopy method. I am very thankful also to Mgr. Martin Čada, Ph.D.; Ing. Petra Kšírová, Ph.D. and RNDr. Jiří Olejníček, Ph.D. for several discussions and help with diagnostics of thin films. Thanks go also to all other members and colleagues from the Department of Low-Temperature Plasma at the Institute of Physics of the Czech Academy of Sciences for creating a very friendly and enjoyable working environment.

I am grateful to prof. Dr. Markus Münzenberg and prof. Dr. Rainer Hippler who were my hosts during my stay at the University of Greifswald. Although the results are not part of my thesis, the work there was very inspiring.

Title: Probe methods for diagnostics of plasmatic systems for deposition of thin films

Author: Michal Zanáška

Department: Department of Surface and Plasma Science

Supervisor: prof. RNDr. Milan Tichý, DrSc., Department of Surface and Plasma Science

Abstract: The doctoral thesis deals with an experimental study of several diagnostic techniques intended for plasma diagnostics and diagnostics of thin films during reactive sputter deposition. A relatively novel probe diagnostic technique called Floating harmonic probe for measurement of the ion density and electron temperature in technological low-temperature plasma is studied. A Langmuir probe is commonly used, however, its application in conditions where non-conducting films are being deposited can be problematic or unreliable. The floating harmonic probe measurement technique deals with this inherent problem of the Langmuir probe. The Floating harmonic probe results are compared to those obtained by a classical Langmuir probe in non-reactive DC continuously driven discharge, and its applicability in reactive regime during deposition of iron oxide thin films is proved. The work deals also with a modification of the Floating harmonic probe called Phase Delay Harmonic Analysis Method which is intended for diagnostics of pulsed driven discharges. The second part of the thesis is devoted to a new proposed method for in-situ diagnostics of thin films. This method monitors the capacitance and resistance of a thin film during deposition up to the frequencies in the kHz range. This new method could be used for diagnostics of dielectric properties of thin films or could be suitable for studying or control of reactive deposition processes.

Keywords: floating harmonic probe, plasma jet, reactive sputtering, pulsed discharge, in-situ impedance spectroscopy

Contents

Motivation **3**

Aims of the doctoral thesis **7**

1 Theoretical part **8**
1.1 Langmuir probe . . . 8
1.1.1 Langmuir's collisionless theory . . . 10
1.1.2 Collisionless ion current theories . . . 13
1.1.3 Processing the IV characteristics . . . 14
1.2 Floating harmonic probe . . . 17
1.2.1 Single FHP . . . 18
1.2.2 Single FHP for pulsed regime . . . 20
1.2.3 Double FHP . . . 22
1.3 In-situ impedance spectroscopy . . . 25

2 Experimental setup **29**
2.1 Vacuum deposition system . . . 29
2.2 Construction of the probes . . . 32
2.3 Langmuir probe measurement system . . . 32
2.4 Single FHP measurement system . . . 33
2.5 Double FHP measurement system . . . 35
2.6 Evaluation of the waveforms . . . 37
2.7 Phase delay harmonic analysis method . . . 37
2.8 In-situ impedance spectroscopy . . . 39

3 FHP measurements in continuous DC regime **44**
3.1 Dependence on the amplitude of the applied voltage . . . 44
3.2 Dependence on the frequency of the applied voltage . . . 50
3.3 Comparison of FHP and LP - pressure scan . . . 52
3.4 Measurement during deposition of Fe_2O_3 . . . 57

4 FHP measurements in DC pulsed regime **60**
4.1 Single FHP in magnetron discharge . . . 60
4.2 Double FHP measurements . . . 66

5 In-situ impedance spectroscopy **69**
5.1 Impedance spectra . . . 69
5.2 Sheath impedance spectra . . . 72
5.3 Dielectric properties of the films . . . 76
5.4 Ex-situ characterization of the films . . . 82

Conclusion **87**

Bibliography **89**

List of symbols and abbreviations **95**

List of author's publications **97**

Attachments **99**

Motivation

Low-temperature plasmas are of a great importance for many of today's state-of-the-art technologies and industrial processes. The term *low-temperature plasma* is very broad and encompasses both the *isothermic* (thermal) and *anisothermic* (nonthermal) plasmas. The thermal plasmas, defined as being in *local thermodynamic equilibrium* (LTE), are typically used where heat is required, e.g. for welding, cutting or spraying. However, it is rather the feature of nonthermal plasmas that is highly appreciated and has been utilized for myriads of applications such as coating and thin film deposition, plasma etching, surface cleaning, ion implantation, light sources or sterilization and decontamination. In the electronic industry, it is particularly the anisotropic plasma etching that is indispensable and has enabled the fabrication of nano-electronics.

The technological progress in the field of functional layers deposition and coating of numerous conductive or non-conductive materials with specific composition, morphology, microstructure or nanostructure, was tremendous in the last half-century. The application of plasmas for film deposition has led to new technological possibilities, that wouldn't be viable with the "older" conventional methods such as *evaporative deposition* methods or CVD (*chemical vapor deposition*), which might require too high a temperature for the solid precursor materials to evaporate or the gaseous precursors to react, respectively [1]. In contrast, for example the PECVD (*plasma enhanced chemical vapor deposition*) method makes use of the high electron energy of several electronvolts in the nonthermal plasma to excite or dissociate the gaseous precursor molecules while keeping their temperature and the temperature of the substrate significantly lower and possibly close to the room temperature. In the *plasma sputtering* methods, belonging to a broad family of PVD (*physical vapour deposition*) methods, the material to be deposited serves at the same time as a cathode of a glow discharge, which is usually ignited in an argon gas. The cathode is commonly referred to as *target*. The argon ions, that gain energy of several hundreds of eV in the cathode layer, bombard the target and release particles of the target material, which may condense on a substrate. If a reactive gas is added into the discharge, compound materials such as nitrides, oxides or sulfides can be prepared. This process is called *reactive sputter deposition*.

On the other hand, the reactive sputter deposition process is very complex and offers many external degrees of freedom that can be adjusted such as: pressure, partial pressure of the reactive gas, discharge current, spatial arrangement or substrate bias. The excitation of the discharge is typically achieved using DC, RF or pulsed DC voltage. All these external "knobs" influence the internal fundamental parameters. All the details of the deposition process need to be understood and controlled in order to obtain reproducible films with desired properties as a function of the deposition conditions. For this purpose it is essential to use various plasma diagnostic techniques. Besides the basic monitoring of the discharge current, voltage and power, the conventional diagnostics are: the Langmuir probe diagnostics, energy resolved mass spectrometry and OES (*optical*

emission spectrometry). Many various diagnostic techniques and methodologies have been developed so far, aiming at improved real-time control and better understanding of plasma-assisted technological processes for deposition or modification of thin films, and the field of plasma diagnostics is still subject to current research efforts.

The Langmuir probe method is the fundamental diagnostic tool for determining, among others, the electron density and electron temperature in plasmas. When the Langmuir probe is used in processing plasmas when dielectric films are deposited, this method fails as the resistance of the insulating film deposited on the probe's tip rises. The resulting IV (current-voltage) characteristics renders highly distorted and the obtained data unreliable. Although there are well known methods to clean the probe by heating the probe tip by electron current or to utilize ion bombardment by applying negative voltage bias, such procedures are not always effective and may complicate the measurement. In order to make possible measurement of the basic plasma parameters - the electron density and the electron temperature - a range of probe methods operating with an AC voltage have been developed to overcome this problem.

One group of these methods is based on the high-frequency/microwave spectroscopy. In the case of the passive plasma resonance spectroscopy, the probe works as antenna that monitors oscillations of the plasma at electron plasma frequency, e.g. the plasma oscillation probe [2]. The general idea of the active plasma resonance spectroscopy probes is to couple a suitable RF signal into the plasma and detect absorption spectrum. From the frequency of particular peak or peaks in the spectrum the electron density is deduced. One example can be the so-called Hairpin probe [3], which makes use of a frequency shift of a resonance (which already exists in vacuum) due to the dielectric property of plasma depending on the electron density. On the other hand, for example the so-called Multipole Resonance Probe [4] is based on the resonance due to the standing surface waves. In contrast, the Multipole Resonance Probe has been found to be highly affected by deposition of only few nm thick metallic film [5]. Advantage of these methods is a possibility to monitor the plasma technological process in-situ continuously, without the need to measure and process the probe characteristic. General disadvantage of these methods may be the need of microwave instrumentation (a vector network analyzer), comparatively complicated construction and/or large size of the probes listed above.

The second group of methods can be said to be based on the theories of current collection to a probe (e.g. Langmuir theory) and work typically with lower frequencies ranging from the kHz range to several MHz. The probe method developed by Braithwaite et al. [6] is based on the self-biasing effect after applying sufficiently large RF voltage (much larger than the electron temperature) to a floating probe with a DC blocking capacitor. After the RF voltage is turned off, the transient probe current and voltage are recorded, from which the ion flux is typically determined, yet it can be used also for electron temperature evaluation. However, this method is not suitable for diagnostics of pulse discharges, due to its limited time resolution. The so-called Sobolewski probe [7] is based on a similar experimental arrangement, yet the high RF voltage is applied continuously. The

ion flux to the probe is determined from the probe current at instants when the applied voltage reaches minimum value. This technique has been proved useful for measurement of the ion flux even in pulsed discharges, see e.g. [8]. The idea to couple a small AC signal to a DC biased probe is not new and was discovered long time ago. An example of the application of this idea may serve the work [9], where a second harmonic signal was used to measure the EEDF (electron energy distribution function). Relatively recently similar concept has been employed in the work [10] for measurement in processing plasmas where the probe gets coated by an insulating film. A small AC voltage is applied to a floating probe using a DC blocking capacitor and the measured harmonic currents are used to determine both the ion density (ion flux) and electron temperature. This probe diagnostic method is called the *floating harmonic probe* (FHP). A modification of the FHP method called *phase delay harmonic analysis method* suited for pulsed discharges was proposed in [11]. The first part of this doctoral thesis is devoted to experimental study of the FHP and PDHAM measuring methods.

The second part of the thesis is devoted to a new proposed method for in-situ diagnostics of dielectric films during plasma-aided depositions based on the principle of *impedance spectroscopy*. Impedance spectroscopy belongs to the most informative and highly appreciated methods in the field of electrochemistry, among others in the area studying semiconductors, electrolytes and their interfaces [12]. The proposed and studied new diagnostic method of in-situ impedance spectroscopy monitors the resistance and capacitance of dielectric films in-situ during deposition process. Plasma serves as the conductive path for closing the circuit. Provided that the film thickness is known, the dielectric properties of the deposited films, such as the relative permittivity, resistivity/conductivity and the dielectric loss factor can be estimated from the measured impedance spectra in the kHz range. The maximal frequency for which the film dielectric parameters can be obtained in this new method depends on both the properties of the deposited layer (resistance and capacity) and the plasma properties (mainly the electron density and temperature). This system could be used e.g. for real-time diagnostics of the deposition process or/and as a film diagnostic tool, that can be easily applied. The conductivity and dielectric properties deposited films are dependent on various factors. Beside the chemical composition of the film material and its crystallinity, the dielectric constant of the film at these frequencies is influenced by the microstructure and nanostructure of the film due to polarization at grain boundaries. In order to use this new in-situ method, the film must be deposited on a conductive substrate and the obtained parameters characterize the film in the direction of the thickness of the film. This is in contrast with the so called van der Pauw method [13], which is used for ex-situ resistivity measurement of films deposited on non-conducting substrates and the so called sheet resistance in the in-plane direction is obtained. Similar idea was suggested in [14, 15] for diagnostics of processing plasmas, where, however, only the capacitance of a dielectric film is estimated at a single frequency.

In particular, the work is focused on diagnostics during *plasma sputtering* and *reactive plasma sputtering* in two different systems - the planar magnetron system and the HCPJ (hollow-cathode plasma jet system) - both operated in two different regimes - DC continuous regime and DC pulsed regime. The planar magnetron sputtering is a well established industrial technology with many applications e.g. in hard coatings for tools (TiN films), optical and protective coatings or metallic back contacts [16]. The motivation of this work to focus also on DC pulse excitation of the discharges is given especially by the significant progress in the DC pulse excitation in the last 20 years, leading to the so called HiPIMS (*high power impulse magnetron sputtering*) technology [17]. In the HiPIMS regime similar average discharge power is applied just like during continuously driven discharges, however, low duty cycle of the pulses is utilized leading to high power density dissipated only during the short time of the active part of the pulse. This regime is characteristic with high fraction of ionized particles sputtered from the target, which can have positive effect on the properties of the films, e.g. reduced internal stress of the resulting films.

Magnetron sputtering technology makes use of magnetic field near the cathode/target for enhanced confinement of electrons. That results in significantly higher electron concentrations, higher sputtering yields, higher deposition rates when compared to the older DC diode arrangement. Consequently, the discharge can be operated even at low pressures of the order of 0.1 Pa, which may be beneficial due to the line-of-sight trajectory of the sputtered particles, which do not loose their energy in collisions. Similar effect can be achieved using the hollow-cathode plasma jet system. The enhanced confinement of the electron near the cathode/target is achieved primarily by the cylindrical geometry of the cathode with appropriate inner diameter leading to the so called *hollow-cathode effect*. The HCPJ is rather a laboratory technique, however it has been successfully used for preparation of several thin films such as: DLC films [18], TiN tribological films [19], ZnO piezoelectric films [20] or STO and BSTO ceramic ferroelectric films [21].

Aims of the doctoral thesis

- One of the aims of this work is to experimentally study the promising probe diagnostic method of floating harmonic probe and apply it for plasma diagnostics in the continuously driven DC discharge in a hollow-cathode plasma jet system during reactive sputter deposition of dielectric thin films (Fe_2O_3, TiO_2).
- Besides the FHP measurements in continuously driven discharge, the work aims at experimental study of the applicability of the single and double FHP method in pulsed discharges in planar magnetron and hollow-cathode plasma jet by means of the phase delay harmonic analysis method.
- The thesis proposes a new method for in-situ impedance spectroscopy of thin films and the work aims also at experimental study of this method during reactive sputter deposition of TiO_2 and Fe_2O_3 thin films.
- A suitable measurement systems with appropriate controlling software need to be designed and realized in order to accomplish these tasks.

1. Theoretical part

1.1 Langmuir probe

The Langmuir probe (in literature sometimes called cold probe or collecting probe) belongs to the most frequently employed plasma diagnostic methods. The fundamental theory was developed already in the twenties of the 20th century by Langmuir and Mott-Smith [22]. The advantage of this method lies in its relatively simple construction and the ability to gain plenty of essential plasma parameters, such as plasma and floating potentials, electron temperature and electron number density or even the EEDF (*electron energy distribution function*). It is a local method with a relatively good spatial resolution.

Langmuir probe consists essentially of an electrode of well-defined shape (typically cylindrical, planar or spherical) which is immersed in the plasma. The main assumption of this probe technique is that the probe dimensions are relatively small, the probe draws negligible current from the plasma and hence produces only small local plasma perturbations. The method is based on measuring the probe's IV characteristics - a relationship between the collected current I_p from plasma and the probe potential V_p. The circuit is closed through another electrode - *reference electrode* - with much larger area in contact with the plasma. Typically, a grounded chamber containing the plasma serves as the reference electrode. As the resistivity of the plasma itself is typically low enough and can be neglected, the IV characteristics of the Langmuir probe is in effect given by the IV characteristics of a sheath layer surrounding the probe.

A typical IV characteristics of a cylindrical probe in low-temperature electropositive plasma is shown in Fig.1.1. Two characteristic voltages are found on a typical IV characteristics - the *plasma potential* Φ and the *floating potential* V_{fl}, which divide the IV characteristics into three regions. For sufficiently negatively biased probe, $V_p < V_{fl}$, most of the electrons are repelled from the probe. In this region the probe current I_p is dominated by the current of positive ions, which are attracted to the probe. A layer of positive space charge is formed between the probe and the plasma, which is commonly denoted as *plasma sheath.* In our convention, the current of the positively charged ions to the probe is negative. This part of the IV characteristics is commonly called the *ion saturation region.* However, in general, depending on the geometry of the probe, the ion current can't be regarded as saturated and numerous models of ion current exist for particular probe regime and geometry. The *floating potential* denotes the probe potential, at which the ion current and electron current become equal (in absolute value) and thus the net probe current I_p is zero. When a floating electrode (with no external voltage applied) is inserted into plasma, it gets spontaneously charged to the value of the floating potential. When increasing the probe potential above the floating potential, more electrons (according to their EEDF) are able to reach the probe, which leads to an increase of the electron current and consequently of the net probe current I_p. This part of the characteristics, i.e. $V_{fl} < V_p < \Phi$, is called the *transition region.*

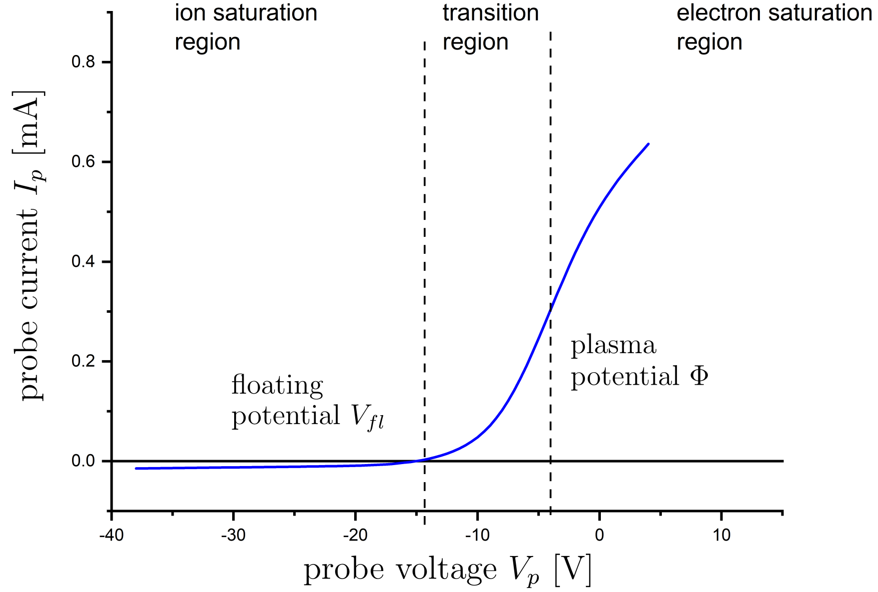

Figure 1.1: The typical course of an IV characteristics of a cylindrical probe recorded in nonmagnetized low-temperature plasma.

At $V_p = \Phi$, the probe potential equals the potential of the plasma itself and the space charge layer around the probe vanishes. The electrons and ions are neither attracted nor repelled from the probe, yet the currents are caused only by the thermal motion of the respective species given by

$$J_{e,i} = \frac{e n_{e,i} \overline{v}_{e,i}}{4} A_p, \tag{1.1}$$

where $n_{e,i}$ denotes the number density of the electrons and ions, respectively, $\overline{v}_{e,i}$ represents their mean thermal velocity and A_p is the probe area. For the case of Maxwell-Boltzmann velocity distribution the mean thermal velocity reads

$$\overline{v}_{e,i} = \sqrt{\frac{8 k_B T_{e,i}}{\pi m_{e,i}}}. \tag{1.2}$$

The electron mass m_e is more than three orders of magnitude lower and the electron temperature is usually much higher than that of the ions. Taking into account the plasma *quasineutrality* ($n_e \approx n_i$), it follows from 1.2 that the probe current at plasma potential is almost entirely comprised by electron current. For this reason, a floating electrode gets negatively charged to to value of the floating potential. Knowing the electron temperature and neglecting the ion current, the electron number density can be evaluated from the probe current at plasma potential using the two relations above.

As the sheath around the probe vanishes a ”knee” on the IV characteristics can be expected due to the change in the slope of the IV characteristics, e.g. in the case of cylindrical probe the course of the IV characteristics changes from convex

to concave. For probe voltages higher than the plasma potential, i.e. $V_p > \Phi$, the electrons are attracted to the probe, a layer of negative space charge is formed and positive ions are repelled from the probe. This part of the IV characteristics is called the *electron saturation region.*

General self-consistent solution of the sheath layer and of the probe current is too complicated [23] and therefore numerous models and approximations for specific plasma and probe conditions have been developed. The Langmuir probe is then said to work in a particular regime. To characterize the regime in which the probe operates, several characteristic quantities need to be taken into account:

- the size of the probe described by characteristic dimension of the probe (e.g. the radius r_p in the case of a cylindrical probe) in relation to the Debye length λ_D characterizing the width of the space charge layer around the probe. A dimensionless parameter known as Debye number $D_\lambda = r_p/\lambda_D$ is commonly used.
$$\lambda_D = \sqrt{\frac{\epsilon_0 k_B T_e}{e^2 n_e}} \tag{1.3}$$
- collisional mean free path $\lambda_{e,i}$ of a particular charged specie, meaning both collisions between the charged particles themselves and collisions between charged particles and neutral gas particles, of which the latter typically dominate in the low-temperature discharges.
- the ratio of the electron temperature to the positive ion temperature also known as the plasma anisothermicity parameter $\tau = T_e/T_i$.
- the cyclotron radius $r_{Le,Li}$ of the respective specie when using the probe in magnetized plasma. Specifically the ratio $\beta = r_p/r_L$ and eventually the orientation of the probe with respect to the magnetic field lines need to be considered [24]. Because the Larmor radius of ions (once charged) is typically larger than that of electrons, the electron current is more influenced (reduced) by the magnetic field than the ion current. Larmor radius of slower particles is lower, ergo the influence of the IV characteristic is more pronounced in the vicinity of the plasma potential than in the tail of the electron energy distribution function.

1.1.1 Langmuir's collisionless theory

The theory developed by Langmuir and Mott-Smith [22] is likely the oldest probe theory whatsoever. It is a *collisionless theory* assuming, that mean free paths of charged species are much larger than the characteristic dimension of the probe and the Debye length, i.e. $r_p \ll \lambda_{e,i} \gg \lambda_D$. Therefore, no collisions of charged particles occur in the sheath around the probe. It is also presumed, that every charged particle reaching the probe surface contributes to the probe current and the probe does not emit electrons (thermo-, photo-, secondary emission). It is further assumed that the currents are independent. Another simplification is that one defines a border of the sheath, which screens the whole probe potential and behind which the plasma is completely undisturbed. Due to the last assumption,

this theory can't be directly applied to the ion current in the saturation region in the case of an anisothermic plasma, where the ion temperature is much lower than the electron temperature, $T_e \gg T_i$).

The analytic evaluation of the probe current is based on determining of the number of charged particles entering the sheath layer through the defined sheath border and reaching the electrode. In the case of a convex shape of the probe surface (more accurately in the case of convex shape of the sheath border) the probe current $I_{e,i}$, formed by electrons and ions respectively, can be determined by:

$$I_{e,i} = A_s e n_{e,i} \int_{w_{x1}}^{w_{x2}} \int_{w_{y1}}^{w_{y2}} \int_{w_{z1}}^{w_{z2}} w_z \, f_{e,i}(\vec{w}) \, dw_x \, dw_y \, dw_z, \tag{1.4}$$

where A_s is the area of the sheath border and $f_{e,i}$ is an isotropic velocity distribution function normalized to 1. The integration limits in the velocity space are specified by the condition, that a particle entering the sheath reaches the electrode.

In the simple case of a planar probe when neglecting edge effects, it follows, that the area of the sheath is independent of the probe voltage and consequently the currents in the respective saturation regions are truly saturated on values given by the relation 1.1.

For the cylindrical and spherical probe the integration limits can be easily worked out using the energy and angular momentum conservation in the field of a central force. For the cylindrical probe in the regions where the given species are repelled from the probe, i.e. the electron current I_e in the range $V_p \leq \Phi$ and the ion current I_i in the range ($V_p \geq \Phi$), the respective currents can be expressed as:

$$I_{e,i} = \frac{A_p n_{e,i} e}{\pi} \iiint\limits_{\substack{u^2 < w_x^2 + w_y^2 < +\infty \\ -\infty < w_z < +\infty}} \sqrt{w_x^2 + w_y^2} \; f_{e,i}(\vec{w}) \; \sqrt{1 \pm \frac{2e\,(V_p - \Phi)}{m_{e,i}(w_x^2 + w_y^2)}} \, dw_x \, dw_y \, dw_z \tag{1.5}$$

$$u = \sqrt{\frac{2e\,|V_p - \Phi|}{m_{e,i}}}, \tag{1.6}$$

where u is minimal velocity that the respective charged particle needs to have at the sheath edge to be able to overcome the repulsive potential and to reach the probe. In the derivation it is assumed, that the length of the probe is much larger than the radius, $l_p \gg r_p$, and the small collecting area at the end of the probe can be neglected. Notice, that the sheath thickness does not need to be known in order to evaluate the current of the given charged species in their respective retarding region.

By performing the integration in formula 1.5 in cylindrical coordinates while using the Maxwell-Boltzmann velocity distribution, the respective currents can be expressed as:

$$I_e = J_e \exp\left(- |\eta|\right) \qquad \text{for } \eta \leq 0 \tag{1.7}$$

$$I_i = J_i \exp(-\tau\eta) \qquad \text{for } \eta \geq 0, \tag{1.8}$$

where the dimensionless probe potential η is defined as:

$$\eta = \frac{e(V_p - \Phi)}{k_B T_e}. \tag{1.9}$$

The exactly same resulting formulas, Eq. 1.7 and Eq. 1.8, are obtained also for planar and spherical geometry.

Similarly, using the equation 1.4 the currents for accelerating probe potentials can be assessed. For cylindrical probe and Maxwell-Boltzmann velocity distribution one gets these results:

$$I_e = J_e \left[\frac{r_s}{r_p} \operatorname{erf} \sqrt{\frac{r_p^2 \eta}{r_s^2 - r_p^2}} + e^{\eta} \operatorname{erfc} \sqrt{\frac{r_s^2 \eta}{r_s^2 - r_p^2}} \right] \qquad \text{for } \eta \geq 0 \tag{1.10}$$

$$I_i = J_i \left[\frac{r_s}{r_p} \operatorname{erf} \sqrt{\frac{r_p^2 \tau |\eta|}{r_s^2 - r_p^2}} + e^{|\eta|} \operatorname{erfc} \sqrt{\frac{r_s^2 \tau |\eta|}{r_s^2 - r_p^2}} \right] \qquad \text{for } \eta \leq 0, \tag{1.11}$$

where $\operatorname{erf} x$ is the error function, $\operatorname{erfc} x = 1 - \operatorname{erf} x$ the complementary error function and r_s expresses the outer radius of the sheath. Ergo, in order to use these expressions, the sheath thickness needs to be known. In practice, two limiting regimes are employed, regarding the sheath thickness in comparison with the radius of the probe - *thick sheath limit* and *thin sheath limit*.

The thick sheath limit is more important from the practical point of view, as it can be easily employed for the evaluation of the number density of the respective particles. In the limit of the *thick sheath*, i.e. $r_s \gg r_p$, the currents according to Eqs. 1.10 and 1.11 for cylindrical probe can be asymptotically, for $|\eta| > 2$, approximated by:

$$I_e \approx J_e \frac{2}{\sqrt{\pi}} (1 + \eta)^{\frac{1}{2}} \qquad \text{for } \eta > 2 \tag{1.12}$$

$$I_i \approx J_i \frac{2}{\sqrt{\pi}} (1 + \tau |\eta|)^{\frac{1}{2}} \qquad \text{for } \tau\eta < -2 \tag{1.13}$$

This thick sheath regime is also referred to as *OML (orbital motion limit)* regime. An empirically used boundary for this regime is $D_\lambda = r_p/\lambda_D = 3$.

In the limit of the *thin sheath*, i.e. $r_s - r_p \ll r_p$, current to the probe is limited by the space charge in the sheath and is given by the surface area of the sheath boundary; for the cylindrical probe, it is given by the relation:

$$I_{e,i} = \frac{r_s}{r_p} J_{e,i} \ . \tag{1.14}$$

The variation of the respective currents in the thin sheath limit with probe voltage is then governed by the change of the sheath thickness [25].

1.1.2 Collisionless ion current theories

The formulas for the ion current for attracting probe voltages, $V_p < \Phi$, derived from the Langmuir theory discussed in 1.1.1 are not valid in anisothermic plasmas where $T_i \ll T_e$. The more detailed analysis of the sheath layer conducted by Bohm [26] by solving the Poisson equation shows, that the attracted ions at the sheath boundary in the limit of cold ions (i.e. $T_i = 0$) need to have at least some minimum velocity c_s, which is the so-called ion acoustic velocity given by Eq. 1.15 (the ion temperature is neglected). This condition is commonly known as the Bohm criterion that expresses a necessary condition for the formation of a stationary sheath in front of a negative absorbing wall [27].

$$c_s = \sqrt{\frac{k_B T_e}{m_i}} \tag{1.15}$$

Ions acquire this speed in the so-called pre-sheath, where they are accelerated by a potential of $k_B T_e / (2e)$. The pre-sheath region penetrates further to the bulk plasma beyond the sheath boundary. The consequence of the Bohm criterion is the fact, that for $V_p < \Phi$ the ion current is not determined by the ion temperature but chiefly by the electron temperature. For a planar probe the saturated ion current is commonly expressed by (see [28]):

$$I_i = \alpha_0 A_p n_i c_s = \alpha_0 A_p n_i e \sqrt{\frac{k_B T_e}{m_i}} \ , \tag{1.16}$$

where $\alpha_0 = \exp(-0.5) \approx 0.61$. Assuming Eqs. 1.16 and 1.7, the floating potential of a planar probe given from the condition $I_p = I_e - I_i = 0$ reads:

$$\frac{e\,(V_{fl} - \Phi)}{k_B T_e} = -\ln\frac{J_e}{I_i} = -\ln\left(\frac{1}{\alpha_0}\sqrt{\frac{m_i}{2\pi m_e}}\right) \approx 5.18 \text{ in argon plasma} \ . \tag{1.17}$$

For cylindrical and spherical probe geometries, several collisionless ion current theories are widely recognized. The ABR (Allen-Boyd-Reynolds) theory [29] assumes cold ions (i.e. $T_i = 0$) and takes into account their radial motion only. Therefore, it does not account for possible reduction of collected current due to the orbital motion. Numerical solutions of the ABR theory for cylindrical probes were published by Chen [30]. The work by Klagge [31] provides analytical approximation of the numerical results applicable in the range $-50 < \eta < -0.5$, $0.25 < D_\lambda < 70$, (this approximation can be found also in [23]). In [32] the ABR theory was used to calculate the floating potential and the corresponding ABR ion current at the floating potential. The ABR ion current at floating potential can be described by Eq. 1.16, however, using different coefficient α depending on the Debye number D_λ and the ion mass m_i. For thick probes, i.e. $D_\lambda \to \infty$, the coefficient α approaches the coefficient used in the planar probe theory, $\alpha \to \alpha_0$. For finite D_λ, the coefficient α is larger than α_0 due to the increased collecting area given by the non-negligible sheath thickness. The work [32] provides also the analytical approximation of α applicable for argon ions.

The theory by Fernández Palop [33] applicable for cylindrical probes, assumes radial motion of ions having a Maxwellian energy distribution. This theory employs the ABR theory in the limiting case of cold ions, $T_i \to 0$.

The effect of orbiting has been included in the theory of Bernstein and Rabinowitz [34] assuming a monoenergetic ion distribution function (isotropic velocity distribution). This theory was further developed by Laframboise [35] who assumed a Maxwellian ion energy distribution function. In the work by Chudáček et al. [36] the analytical approximation of the numerical solutions of the Laframboise theory for cylindrical probe can be found, which is valid for arbitrary η and D_λ.

1.1.3 Processing the IV characteristics

Due to the many different regimes of operation of the Langmuir probe, there are many methods on how to best process the IV characteristics and evaluate the plasma parameters. I will mention only those methods, that have been used in my doctoral thesis and are relevant to the studied plasma conditions. Other methods are discussed e.g. in [23, 37].

Plasma potential

It can be seen in Fig. 1.1, that there is not always an obvious "knee" on the IV characteristics, which could be used to mark the plasma potential. This is mainly due to the fact, that the electron current does not saturate in the electron saturation region, yet it further increases with the increase of the probe potential due to the expansion of the sheath.

As the most accurate method for estimating the plasma potential (e.g. [23]) is considered the derivative method. The plasma potential is estimated as the abscissa of the inflection point of the IV characteristics. This follows from the assumption, that the course of the electron current of a cylindrical probe is convex in the retarding region, while concave in the electron saturation region. In practice, the plasma potential is evaluated from the abscissa of the zero crossing point of the 2. derivative of the IV characteristics. However, one should be aware of effects that can cause rounding of the "knee" at the inflection point. Mainly, this is caused by processes at the probe surface which were heretofore neglected. To these processes count e.g. secondary emission of electrons or the variation of the surface work function along the probe surface, which can be further influenced by adsorbed impurities. Some effect on the rounding have also possible collisions of electrons in the sheath layer.

Electron energy distribution function

The Langmuir collisionless theory discussed in 1.1.1 can be also employed to determine the electron energy distribution function from the probe characteristics. Of course, the same theory holds also for ions but it is usually of no practical application. We will again assume that a cylindrical probe is used and that the electron velocity distribution function is isotropic. Instead of the velocity distribution function $f(w) = f(\vec{w})$ the energy distribution function $f_E(\epsilon)$ is introduced normalized by the relation 1.18. The formula 1.19 expresses a formal relation

between these two distribution functions.

$$\int_{0}^{+\infty} f_E(\epsilon)\, d\epsilon = 1 \tag{1.18}$$

$$f_E(\epsilon)\, d\epsilon = \frac{4\pi\sqrt{2}}{m_e^{\frac{3}{2}}}\sqrt{\epsilon} f\left(\sqrt{\frac{2\epsilon}{m_e}}\right) d\epsilon = f(\vec{w})\, dw_x\, dw_y\, dw_z \tag{1.19}$$

Properly rewriting the equation 1.5 into spherical coordinates, working out the integration in angular variables and differentiating twice by the probe voltage V_p, one gets the so-called *Druyvesteyn relation* [38]:

$$\frac{d^2 I_e}{dV_p^2} = \frac{e^3 A_p}{2\sqrt{2m_e}} \frac{f_E\left(e\left|V_p - \Phi\right|\right)}{\sqrt{e\left|V_p - \Phi\right|}} = \frac{e^3 A_p}{2\sqrt{2m_e}} g\left(e\left|V_p - \Phi\right|\right) \qquad \text{for } V_p \leq \Phi, \tag{1.20}$$

where the function $g(\epsilon)$ is frequently refered to as the *EEPF (electron energy probability function)*. By integration of this relation both the equation for the electron density 1.21 and for the mean electron energy $\bar{\epsilon}$ 1.22 can be obtained.

$$n_e = \left(\frac{2}{e}\right)^{\frac{3}{2}} \frac{m_e^{\frac{1}{2}}}{A_p} \int_{-\infty}^{0} \left|V_p\right|^{\frac{1}{2}} \frac{d^2 I_e}{dV_p^2}\, dV_p \tag{1.21}$$

$$\bar{\epsilon} = \frac{e \int_{-\infty}^{0} \left|V_p\right|^{\frac{3}{2}} \frac{d^2 I_e}{dV_p^2}\, dV_p}{\int_{-\infty}^{0} \left|V_p\right|^{\frac{1}{2}} \frac{d^2 I_e}{dV_p^2}\, dV_p} \tag{1.22}$$

To use these expressions the plasma potential must be evaluated first. In practice, the obtained distribution function is disturbed in the vicinity of the plasma potential as a consequence of the rounding of the characteristics at the inflection point. This causes usually an underestimation of the electron number density and overestimation of the electron mean energy using the above mentioned formulae. Furthermore, one should always keep in mind, that the measured probe current is the sum of electron and ion current. It might happen, that the tail of the EEDF obtained from the 2nd derivative of the net probe current is influenced by the non-negligible 2nd derivative of the ion current. Therefore, it is a good practice to fit the ion current in the ion saturation region and subtract its 2nd derivative in order to obtain the second derivative of the electron current, see [23].

Electron temperature

The electron temperature is a well defined parameter for the case, that the electron distribution function can be described by the Maxwell-Boltzmann distribution function. From Eq. 1.7 it can be seen, that in the semi-logarithmic scale, the electron current in the transition region is linearly dependent on the probe voltage with a slope proportional to $1/T_e$. Though, the electron temperature is often evaluated rather from the slope of the 2nd derivative of the IV characteristics

plotted in semi-logarithmic scale, where the contribution of the 2nd derivative of the ion current is often neglected. Furthermore, according to the Eq. 1.20, the 2nd derivative of the electron current is directly proportional to the EEPF, which in the case of Maxwellian distribution, is a linear function of energy with a slope proportional to $1/T_e$ in the semi-logarithmic scale. In general, the so called effective temperature T_{ef} can be evaluated from the mean electron energy $\overline{\epsilon}$ obtained from Eq. 1.22 even for non-Maxwellian EEDF:

$$k_B T_{ef} = \frac{2}{3}\overline{\epsilon}. \tag{1.23}$$

Electron density

The easiest method to evaluate the electron number density n_e is to use the formula 1.1 for the electron current J_e when the probe potential equals the plasma potential. The magnitude of the ion current is usually several orders of magnitude lower and is commonly neglected. The electron density can be then easily obtained from the net probe current at plasma potential $I_p(\Phi)$ as:

$$n_e = \frac{4I_p(\Phi)}{eA_p}\sqrt{\frac{\pi m_e}{8k_B T_e}} \tag{1.24}$$

When the assumptions of the OML regime are fulfilled, i.e. commonly the condition $r_p/\lambda_D < 3$ is assumed, the electron current in the case of a cylindrical probe can be described by Eq. 1.12. Raising the electron current to the power of two, we get a linear dependence on the probe voltage:

$$I_e^2 = \frac{2e^2 n_e^2 A_p^2}{\pi^2 m_e} k_B T_e \left[1 + \frac{e\left(V_p - \Phi\right)}{k_B T_e}\right]. \tag{1.25}$$

From the slope of the line, the electron density is obtained. Advantage of this approach is, that the electron temperature does not need to be known. Furthermore, this method does not depend on precise evaluation of the plasma potential, unlike the previous method.

Ion density

For the evaluation of the ion density, a proper theory of the ion current should be used, see 1.1.2. It is convenient to use a suitable analytical approximation of the numerical results of the ion current which can be found typically in the form $i_i = i_i\left(D_\lambda, \eta, \tau\right)$, where i_i represents the ion current I_i normalized by $J_i/\sqrt{\tau}$. For estimation of the ion density, the iterative procedure described in [23] was used in this work. The ion density n_i is evaluated from single value of ion current I_i measured at a specific probe voltage η; typically $\eta = -15$ or $\eta = -20$. Such a voltage is usually sufficiently negative to assume, that the electron current is negligible and the ion current I_i is equal to the negative probe current $-I_p$. As the Debye number D_λ depends on the ion density to be estimated, the first step in the iterative procedure is to evaluate D_λ using some initial guess of n_i. One can use the electron density n_e for the initial guess or the ion density estimated from the

simple theory of planar probe, see Eq. 1.16. From the analytical approximation the normalized current i_i is obtained. From the ratio of the measured ion current and the normalized current I_i/i_i the normalization factor $J_i/\sqrt{\tau}$ is estimated from which one can get the first approximation of the ion density according to Eq. 1.1. The iterative procedure repeats by evaluating second approximation D_λ etc. The procedure stops, when the next two following approximations of n_i do not differ much from each other.

1.2 Floating harmonic probe

The basic concept of the so-called floating harmonic probe (FHP) was originally developed for direct-display of the electron temperature fluctuations in the edge plasma of tokamaks [39, 40]. It is based on applying a small ac voltage with frequency much below the ion plasma frequency to a single probe tip through a capacitor and detecting the harmonic currents. In [10], this technique was extended to evaluate also the ion number density and it was proposed to be used in low-temperature processing plasmas during deposition of thin films. Up to now the FHP was found useful e.g. during deposition of DLC thin films [41, 42] and the basic concept of FHP has been further developed into double probe diagnostics [43], method using sideband harmonics generated by dual-frequency input voltage [44, 45] or method applicable to pulsed discharges with temporal resolution below 1 μs [11]. Methods applicable even when the capacitive reactance of the deposited film is not negligible were proposed in [46, 47].

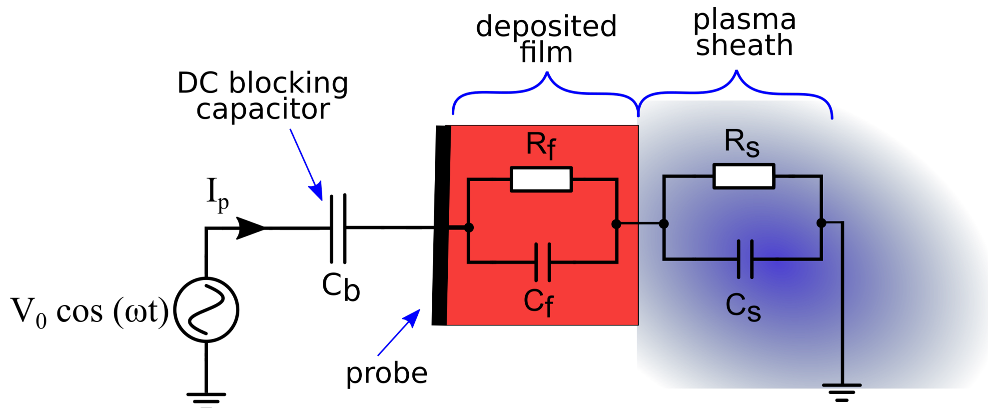

Figure 1.2: Basic illustration of the connection of a probe for the single FHP method. The sheath around the probe and the deposited film is represented by a parallel connection of an ideal resistor and capacitor.

1.2.1 Single FHP

An ac voltage $V_0 \cos \omega t$ of a relatively small amplitude V_0 is applied to the probe, and the resulting probe current I_p is measured. A so called *dc blocking capacitor* is connected between the probe and the harmonic voltage source, see Fig. 1.2. The dc blocking capacitor ensures, that no dc current can flow through the probe and the probe is floating at a certain potential $\bar{V}$ (defined with respect to the plasma potential) close to the floating potential. The capacitance C_b of the dc blocking capacitor must be high enough so as it's impedance and resulting voltage drop could be neglected. The actual potential at the electrode with respect to the plasma potential therefore is

$$V_p = \bar{V} + V_0 \cos \omega t. \tag{1.26}$$

The probe current is assumed to be a sum of the current of positive ions and the electron current

$$I_p = -I_i + J_e \exp\left[\frac{e\left(\bar{V} + V_0 \cos \omega t\right)}{k_B T_e}\right], \tag{1.27}$$

where the electron current is expressed according to the Eq. 1.7 assuming a Maxwellian EEDF. The ion current I_i is supposed to be independent of the probe voltage. According to [48], the periodic exponential term describing the electron current can be expanded into Fourier series in terms of modified Bessel functions $I_k(z)$ of the first kind of integer order k as

$$e^{z \cos \theta} = I_0(z) + 2 \sum_{k=1}^{\infty} I_k(z) \cos k\theta. \tag{1.28}$$

Using this mathematical formula, the probe current gets decomposed into a dc current i_{DC} and harmonic current components $i_{k\omega}$

$$I_p = i_{DC} + \sum_{k=1}^{\infty} i_{k\omega} \cos k\omega t \tag{1.29}$$

$$i_{DC} = -I_i + J_e \exp\left(\frac{e\bar{V}}{k_B T_e}\right) I_0\left(\frac{eV_0}{k_B T_e}\right) \tag{1.30}$$

$$i_{k\omega} = 2J_e \exp\left(\frac{e\bar{V}}{k_B T_e}\right) I_k\left(\frac{eV_0}{k_B T_e}\right). \tag{1.31}$$

Evidently, beside the harmonic current of the fundamental frequency ω, currents of higher harmonic frequencies $k\omega$ are generated due to the non-linear characteristics of the sheath. It follows from Eq. 1.31, that the electron temperature can be evaluated from the ratio of the amplitudes of the harmonic currents $i_{k\omega}$ by numerical solution of the equation

$$\frac{i_{n\omega}}{i_{m\omega}} = \frac{I_n\left(\frac{eV_0}{k_B T_e}\right)}{I_m\left(\frac{eV_0}{k_B T_e}\right)}. \tag{1.32}$$

For clarity, the relation Eq. 1.32 for the ratios $i_{1\omega}/i_{2\omega}$ and $i_{2\omega}/i_{3\omega}$ is shown in Fig. 1.3. Clearly, the relative content of higher harmonic currents increases, with increase of the voltage amplitude V_0.

Due to the DC blocking capacitor, the DC component of the current given by Eq. 1.30 must be zero, i.e. $i_{DC} = 0$, which then leads to the expression of the electron current in terms of the ion current:

$$\frac{I_i}{I_0\left(\frac{eV_0}{k_BT_e}\right)} = J_e \exp\left(\frac{e\bar{V}}{k_BT_e}\right). \tag{1.33}$$

The harmonic currents given by Eq. 1.31 can be then rewritten in terms of the ion current as

$$i_{k\omega} = 2I_i\frac{I_k\left(\frac{eV_0}{k_BT_e}\right)}{I_0\left(\frac{eV_0}{k_BT_e}\right)}. \tag{1.34}$$

The relation Eq. 1.34 can be used to evaluate the probe ion current I_i from one of the harmonic currents $i_{n\omega}$. In chapter 3 the ion currents obtained from $i_{1\omega}$ and $i_{2\omega}$ are compared. The ion density obtained from $i_{1\omega}$ was typically used, as it was in better agreement with the LP data. For the evaluation of the ion density n_i from the ion current I_i, a proper formula for the ion current must be used, see 1.1.2.

In the simple case of a planar probe, the ion current can be described by Eq. 1.16, and the ion density is obtained by

$$n_i = \frac{i_{1\omega}}{2\left(0.61eA_p\sqrt{k_BT_e/m_i}\right)}\frac{I_0\left(\frac{eV_0}{k_BT_e}\right)}{I_1\left(\frac{eV_0}{k_BT_e}\right)} \tag{1.35}$$

When a more complicated theory of the ion current to the probe is to be used, see 1.1.2, the Eq. 1.34 must be solved numerically.

It should be noted, that by applying the AC voltage, the probe no longer floats at its former floating potential V_{fl}, but the probe's mean potential $\bar{V}$ is shifted to more negative voltages. That is the effect known from the asymmetrical capacitively coupled RF discharges where the so called *DC self-bias* is created. The mean potential $\bar{V}$ can be derived from the Eq. 1.33:

$$\frac{e\bar{V}}{k_BT_e} = -\ln\left(\frac{J_e}{I_i}\right) - \ln\left(I_0\left(\frac{eV_0}{k_BT_e}\right)\right) \tag{1.36}$$

The first term of Eq. 1.36 equals the floating potential, when no AC voltage is applied (compare with Eq. 1.17); the second term, see Fig. 1.4, expresses the shift of the DC potential of the probe due to the applied AC voltage.

For the operation of the probe as described above, it is crucial that the capacitance of the sheath C_s can be neglected. This condition, however, limits the maximum operating frequency ω that can be used. Furthermore, the potential drop on the capacitance of the insulating film C_f is in the treatment above also neglected, which limits the maximum thickness of the deposited insulating film.

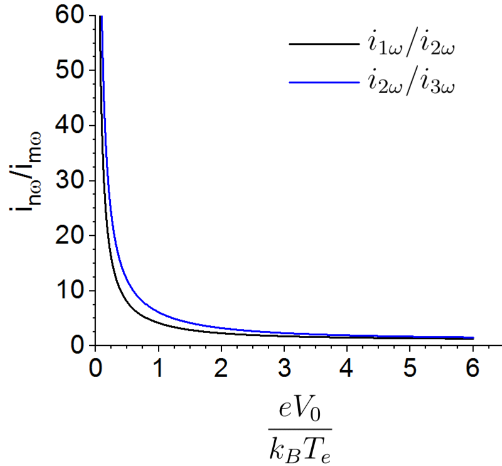

Figure 1.3: Plot of the ratio of harmonic currents according to Eq. 1.32 in dependence of the ratio of the applied AC voltage amplitude and the electron temperature.

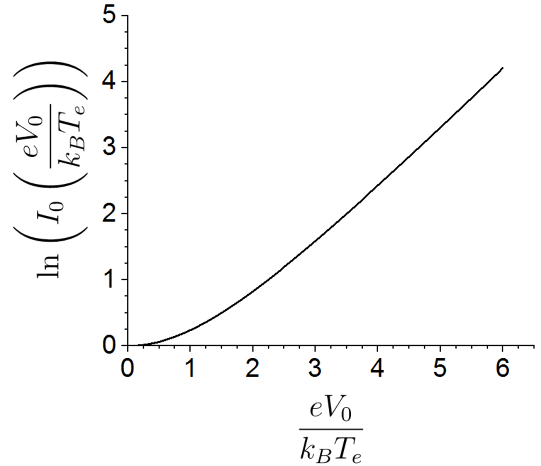

Figure 1.4: The selfbiasing effect according to Eq. 1.36 in dependence of the ratio of the applied AC voltage amplitude and the electron temperature.

As the IV characteristic of the sheath (Langmuir probe) is non-linear, the sheath resistance in this context is defined as the derivative of the probe IV characteristics at the FHP mean potential, see [28]:

$$R_s^{-1} = \frac{dI_p}{dV_p}\left(\bar{V}\right), \tag{1.37}$$

In the case of Maxwellian EEDF it follows from Eq. 1.7 that $R_s \propto T_e/J_e \propto \sqrt{T_e}/\left(A_p n_e\right)$. Similarly, in this context, the sheath capacitance represents the differential capacitance of the sheath at $\bar{V}$, i.e. $C_s = \frac{dQ_s}{dV_p}\left(\bar{V}\right)$. The displacement current arises due to a net positive charge Q_s in the sheath layer that is compensated by electrons on the surface of the probe. As the sheath charge varies during the AC voltage cycle, the surface charge must also vary, causing a current dQ_s/dt to flow in the electrode's electrical connection.

Neglecting possible conductivity of the deposited film $1/R_f$, the FHP operating range is limited by

$$\omega C_f \gg 1/R_s \gg \omega C_s. \tag{1.38}$$

1.2.2 Single FHP for pulsed regime

In continuously driven DC discharges, where the plasma is stationary and the plasma potential is independent on time, the probe current is solely generated by the applied AC voltage sweeping around the probe mean potential $\bar{V}$ which is close to the local floating potential V_{fl}. However, in pulsed discharges the plasma potential variations (and accordingly variations of the local floating potential) during the pulse period can cause the probe not to be able to follow the local floating potential due to an RC delay of the capacitance of the probe to the

ground and the limited probe current (sheath resistance). In that case, the probe does not operate around the stationary mean potential $\bar{V}$, but around a potential $\bar{V} + V_t$, where V_t represents the probe transient voltage. This generates some transient probe current i_t (charging the probe due to its capacitance) that can be measured together with the AC current. In the work [11], the theory of single FHP has been extended to account for the transient current flowing through the probe.

Let's first assume that the frequency of the AC voltage is high enough, so that the plasma parameters do not significantly change during the AC voltage period. Similarly to the theory of single FHP, the probe current reads:

$$I_p = -I_i + J_e \exp\left[\frac{e\left(\bar{V} + V_t + V_0 \cos\omega t\right)}{k_B T_e}\right]. \tag{1.39}$$

Proceeding in similar way as described in 1.2.1 leads to relation identical to Eq. 1.32 for the ratio of harmonic currents $i_{n\omega}/i_{m\omega}$, which is used for evaluation of the electron temperature. On the other hand, the mean current averaged over one period of the AC voltage is not zero ($i_{DC} = i_t \neq 0$), but equal to the transient current i_t caused by the transient voltage V_t:

$$i_t = -I_i + J_e \exp\left[\frac{e\left(\bar{V} + V_t\right)}{k_B T_e}\right] I_0\left(\frac{eV_0}{k_B T_e}\right). \tag{1.40}$$

The positive ion current I_i can be evaluated from one of the harmonic currents $i_{n\omega}$ using the expression:

$$I_i = -i_t + i_{n\omega}\frac{I_0\left(\frac{eV_0}{k_B T_e}\right)}{2I_1\left(\frac{eV_0}{k_B T_e}\right)}. \tag{1.41}$$

This expression is similar to Eq. 1.34, yet the transient current is taken into account. For the actual measurement in pulsed discharge, the PDHAM method was used, see 2.7, which makes possible to use frequencies of the AC voltage, the period of which is longer compared to the temporal changes of the plasma parameters during the pulse.

Notice, that the DC blocking capacitor represents essentially the capacitance of the single probe to the ground, see Fig.1.2. The parasitic capacitance is typically orders of magnitude lower. Generally, better results from the FHP can be obtained, when the FHP is able to certain extent to follow the temporal changes of the floating potential during the pulse, as it is shown in chapter 4. The capacitance of the DC blocking capacitor must be high enough to fulfill the condition

$$\omega C_B \gg 1/R_s. \tag{1.42}$$

The RC constant of the probe near the mean potential $\bar{V}$ is essentially given as $R_s C_B$. Increasing the size of the probe A_p decreases the sheath resistance, however, in order to fulfill the condition Eq. 1.42, the capacitance of the bias capacitor must be proportionally increased. Therefore, in the case of the single FHP, the minimal RC constant at given plasma conditions can't be decreased by increasing the size of the probe A_p.

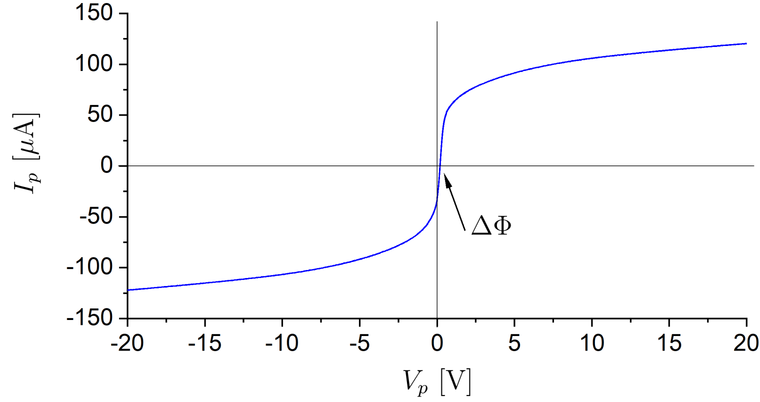

Figure 1.5: The typical course of an IV characteristics of a double probe recorded in electropositive low-temperature plasma with low electron temperature $T_e \approx$ 0.1 eV.

1.2.3 Double FHP

The concept of the single FHP method described in 1.2.1, can be similarly applied also to double probe measurements [43]. The principle of the double FHP method is similar to the single FHP and is based on the theory of double Langmuir probe developed already in [49]. In the double probe method, no reference electrode is needed, unlike in the single probe method. For the further analysis it is assumed, that the double probe consists of two equivalent electrodes (probes) of the same geometry and surface area which are positioned near to each other, so that the ion and electron concentrations and electron temperature at both the probes could be assumed equal. On the other hand, the distance between the probes should be large enough, so that the sheaths around the probes do not overlap and, consequently, the current to both the probes could be described by the single Langmuir probe theory discussed in 1.1.

A typical IV characteristics of double Langmuir probe is shown in Fig. 1.5, where V_p is the voltage applied between the probes and I_p is the measured current. The current I_p can be derived from the fact, that currents flowing through both the probes have to be equal.

$$I_p = I_{1e} - I_{1i} = I_{2e} - I_{2i} \tag{1.43}$$

Assuming Maxwellian EEDF the electron currents I_{1e}, I_{2e} can be written according to Eq. 1.7 as

$$I_{ke} = J_e \exp \frac{e\left(V_k - \Phi_k\right)}{k_B T_e}, k = 1, 2, \tag{1.44}$$

where V_1, V_2 are the respective potentials of the probes fulfilling $V_p = V_1 - V_2$. Generally, the respective plasma potentials Φ_1, Φ_2 might differ; $\Delta\Phi = \Phi_1 - \Phi_2$. Furthermore, assuming that the ion currents $I_{1i} = I_{2i} = I_i$ do not depend on the voltage, it follows from the Eq. 1.43, that the IV characteristic of the double

Langmuir probe can be described by

$$I_p = I_i \tanh \frac{e\,(V_p - \Delta\Phi)}{2k_B T_e}. \tag{1.45}$$

In the double FHP method, an AC harmonic signal is applied between the two probes, i.e. $V_p = V_0 \cos \omega t$. The difference in the plasma potentials $\Delta\Phi$ can be minimized by placing the two probes near each other. In general, however, if a large capacitor is connected in series with the AC voltage source, see 2.6, it will get charged by plasma to compensate this difference and then the following formula for the probe current can be used.

$$I_p = I_i \tanh \frac{eV_0 \cos \omega t}{2k_B T_e}. \tag{1.46}$$

Following the approach suggested in [43], the hyperbolic tangent function in Eq. 1.46 can be for $eV_0 \ll k_B T_e$ approximated by a few first terms of the Taylor series leading to:

$$\frac{I_p}{I_i} \approx \left(a - \frac{a^3}{4}\right) \cos \omega t - \frac{a^3}{12} \cos 3\omega t = \frac{1}{I_i} \left(i_{1\omega} \cos \omega + i_{3\omega} \cos 3\omega\right) \;, \tag{1.47}$$

where

$$a = \frac{eV_0}{2k_B T_e} \;. \tag{1.48}$$

The terms with power higher than a^4 have been neglected. Moreover, for practical experimental reasons only the first four harmonic currents $i_{1\omega}, i_{2\omega}, i_{3\omega}, i_{4\omega}$ are taken into account. As the IV characteristics of the double probe is symmetrical, even harmonics, i.e. $i_{2\omega}, i_{4\omega}$ equal zero and theoretically are not present in the spectrum.

It follows, that the electron temperature can be obtained from the ratio of the third to the first harmonic current, $R = i_{3\omega}/i_{1\omega}$, by using the expression

$$\frac{k_B T_e}{eV_0} = \sqrt{\frac{3R+1}{48R}} \;. \tag{1.49}$$

The ion current is obtained from the first harmonic current by

$$I_i = \frac{i_{1\omega}}{a - \frac{a^3}{4}} \;. \tag{1.50}$$

The ion density can be then obtained from an appropriate ion current theory, see 1.1.2 and 1.1.3.

In order to asses the range of validity of the assumption $eV_0 \ll k_B T_e$ in the derivation of Eq. 1.47, Eq. 1.49 and Eq. 1.50, I have expressed the harmonic currents $i_{n\omega}$ by expanding the Eq. 1.46 into Fourier series:

$$\frac{i_{n\omega}}{I_i} = 2 \left| \int_0^1 \tanh\left(a \cos\left(2\pi t\right)\right)\; \cos\left(2\pi n t\right)\, dt \right| \tag{1.51}$$

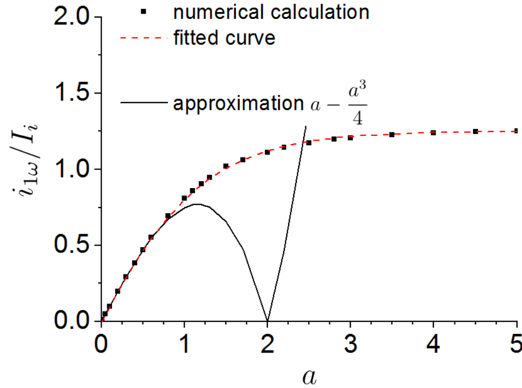

Figure 1.6: Plot of the normalized first harmonic current $i_{1\omega}/I_i$ obtained by numerical integration of Eq. 1.51 (black squares) in comparison with the approximate formula Eq. 1.50 (black line). The red dashed line depicts the fitted curve given by Eq. 1.52.

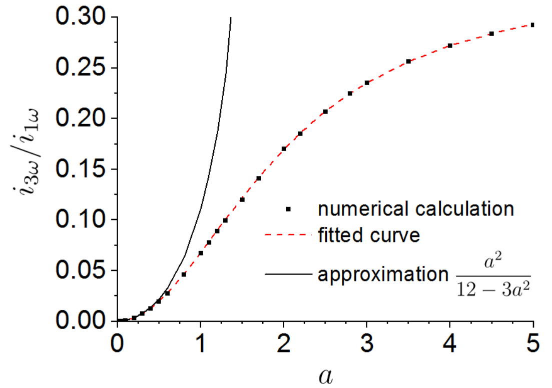

Figure 1.7: Plot of the ratio of the harmonic currents $i_{3\omega}/i_{1\omega}$ obtained by numerical integration of Eq. 1.51 (black squares) in comparison with the approximate formula Eq. 1.49 (black line). The red dashed line depicts the fitted curve given by Eq. 1.53.

By numerical integration of this expression, I have obtained the normalized harmonic currents $i_{1\omega}/I_i$, $i_{3\omega}/I_i$ and their ratio R, which is depicted in Fig. 1.6 and Fig. 1.7 together with the approximations according to Eq. 1.49 and Eq. 1.50. The approximate formulas are in good agreement with the numerical results for $a < 0.5$. At $a = 0.5$ the relative error of $i_{3\omega}/i_{1\omega}$ and $i_{1\omega}/I_i$ amounts to 13% and 0.5%, respectively. I have fitted the numerical data by analytical expressions Eq. 1.52 and Eq. 1.53, which are applicable in the range $0.4 < a < 8$ with maximum relative error of 4%. However, one should be aware of the fact, that a too high voltage amplitude scans the double probe IV characteristics over the range of voltages within which the assumptions of the simple double probe theory might not be satisfied, because the ion current I_i can depend on the probe voltage.

$$\frac{i_{1\omega}}{I_i} = 1.25 - 3.3/\left(1 + \exp\frac{a + 0.35}{0.73}\right) \tag{1.52}$$

$$R = \frac{i_{3\omega}}{i_{1\omega}} = 0.34\left(1 - \frac{4}{4 + a^2}\right) \tag{1.53}$$

$$\frac{k_B T_e}{eV_0} = \frac{1}{4}\sqrt{\frac{0.34}{R} - 1} \tag{1.54}$$

In practice, the electron temperature is evaluated first, which is then used for the determination of the ion current or/and ion density. When the measured ratio $i_{3\omega}/i_{1\omega}$ is lower than about 0.01 (corresponding to $a \approx 0.4$) the approximate expressions Eq. 1.49 and Eq.1.50 can be used. When the ratio $i_{3\omega}/i_{1\omega}$ is greater than 0.01, the expressions Eq. 1.54 and Eq. 1.52 should be used instead.

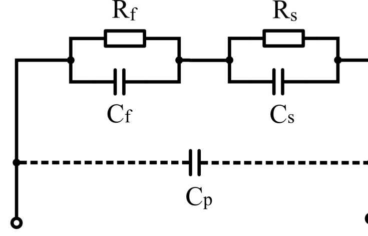

Figure 1.8: The equivalent circuit describing the impedance of the deposited film and the surrounding plasma sheath together with the parasitic capacitance C_p. R_f, C_f represents the film, R_s, C_s represents the sheath.

Similarly to the single FHP method, it is assumed that the deposited film on the probes does not influence the measurement, i.e. the condition Eq. 1.38 has to be fulfilled.

1.3 In-situ impedance spectroscopy

In this method, a conducting substrate is used as an electrode immersed in the processing plasma on which the dielectric film is deposited. Similarly to the FHP method, a small AC voltage referenced to the metal vacuum vessel of a given frequency $V_0 \cos(\omega t + \varphi_1)$ is applied to the electrode/substrate, see Fig. 1.2. That induces current in the circuit consisting of the electrode, the thin film on the electrode, plasma sheath nearby the electrode, bulk plasma and the vacuum vessel. From the amplitude I_0 and phase φ_2 of the measured current signal at the given frequency $I_0 \cos(\omega t + \varphi_2)$, the complex impedance of the equivalent circuit can be obtained as:

$$Z = \frac{V_0}{I_0} \exp(i\varphi), \tag{1.55}$$

where $\varphi = \varphi_1 - \varphi_2$ and i represents the imaginary unit, $i^2 = -1$. The equivalent circuit is composed of the impedance of the dielectric film Z_f, the impedance of the plasma sheath Z_s around the deposited film and possibly also of the parasitic capacitance C_p as indicated in Fig. 1.8. The resistance of the bulk plasma and the impedance of the sheath around the grounded inner wall of the vacuum vessel is not included in the equivalent circuit. The bulk plasma can be expected to have negligible resistance and to be in a good contact with the plasma reactor wall. The sheath impedance around the grounded electrode is negligible due to its much larger area in contact with plasma in comparison to the area of the electrode/substrate. Consequently, the impedance of this part of the circuit can be considered as negligible. The scheme of the equivalent circuit under these assumptions is shown in Fig 1.8.

For the sake of simplicity, it can be assumed that the deposited film impedance can be treated as a parallel connection of an ideal capacitance C_f and an ideal resistance R_f (later the frequency dependence of C_f and R_f of real films will be taken into account). Similarly, the impedance of the sheath is treated as a parallel combination of R_s and C_s. The IV characteristics of the sheath is highly non-

linear and it is a function of the difference between the probe potential and the plasma potential. Therefore, in order to define the sheath impedance correctly, the electrode is kept at a particular potential. That is provided by the large DC blocking capacitor connected in series with the electrode. Hence, for small AC voltage amplitudes $V_0 \ll T_e$ and frequencies lower than the ion plasma frequency $\omega < \omega_i$ the sheath resistance R_s is given by the relation Eq. 1.37.

In this method, the equivalent circuit impedance $Z(\omega)$ is measured in a wide frequency range from 1 Hz to 1 MHz. The so called Nyquist plot (complex impedance depicted in the complex plane with frequency as a parameter) and the Bode plot (absolute value of the impedance and the phase as a function of the frequency) can be used to observe the dependence of the impedance on the frequency. These plots of an exemplary impedance spectrum of the equivalent circuit are shown in Fig. 1.9.

The frequencies f_1 and f_2 are important characteristic frequencies for the equivalent circuit (without parasitic capacitance) given by:

$$f_1 = \frac{1}{2\pi C_f\left(R_f \parallel R_s\right)}, \tag{1.56}$$

$$f_2 = \frac{1}{2\pi R_s C_s}, \tag{1.57}$$

where $\parallel$ indicates a parallel combination $R_f \parallel R_s = R_f R_s / \left(R_f + R_s\right)$. The frequency f_1 characterizes the transition between the low-frequency part of the spectrum dominated by the film impedance and the high-frequency part of the spectrum dominated by the sheath impedance. In order to be able to reliably separate the impedance of the film from the impedance of the sheath the following assumption needs to be fulfilled:

$$f_1 \ll f_2 \tag{1.58}$$

In the case when $R_f \gg R_s$ the condition Eq. 1.58 reduces to $C_f \gg C_s$. If the condition Eq. 1.58 is satisfied, the Nyquist plot of the equivalent circuit impedance can be viewed as to be composed of two semicircles corresponding to the impedance of the film (semicircle at low frequencies) and the impedance of the sheath (semicircle at high frequencies), see Fig. 1.9. The two semicircles can more or less overlap, depending on how well the condition Eq. 1.58 is fulfilled. Then a plateau in the Bode plot of the absolute value of the impedance between the frequencies f_1 and f_2 can be observed, which makes possible to reliably determine the sheath resistance R_s. Provided, that the condition Eq.1.58 is met, the phase of the impedance Z at the frequency f_2 is $-45°$ and the phase at the frequency f_1 is given as

$$-\mathrm{arctg}\left(\frac{1}{2R_s/R_f + 1}\right), \tag{1.59}$$

which is approximately $-45°$ for $R_f \gg R_s$, see Fig. 1.9b.

For real materials the representation of the film impedance by capacitance and resistance as used in the simple model might not be possible, since both the quantities can vary with the frequency. Thus, fitting the complete measured

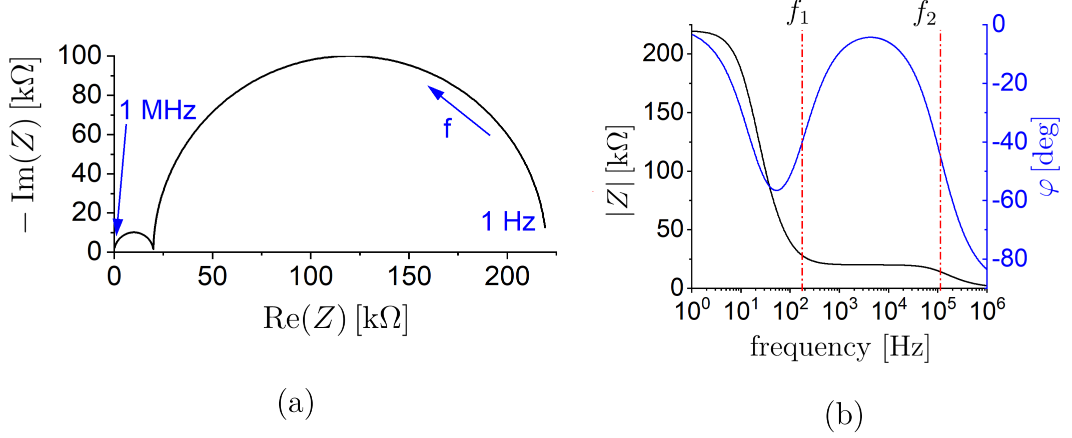

Figure 1.9: Illustration of the (a) Nyquist plot and (b) Bode plot of the equivalent circuit depicted in Fig. 1.8 in the frequency range from 1 Hz to 1 MHz for parameters $R_s = 20$ kΩ, $C_s = 70$ pF, $C_p = 0$ pF, $R_f = 200$ kΩ, $C_f = 50$ nF. At these conditions, the effect of the parasitic capacitance is almost identical to the sheath capacitance, i.e. with changed parameters C_s and C_p in such a way that $C_s + C_p = 70$ pF, the difference in the spectra is negligible. Note, that y-axis represents the negative imaginary part of the impedance.

spectrum to the model would not be reliable for many materials. Therefore, only the high frequency part of the spectrum was fitted to obtain the resistance R_s and capacitance C_s of the sheath. The frequency dependence of the impedance of the film Z_f can be obtained from the measured impedance Z using the relationship:

$$Z_f = Z - Z_s = Z - 1/\left(\frac{1}{R_s} + i\omega C_s\right). \tag{1.60}$$

The film resistance R_f and capacitance C_f at a given frequency are evaluated from the relation:

$$\frac{1}{Z_f} = \frac{1}{R_f} + i\omega C_f. \tag{1.61}$$

The dielectric properties of materials are commonly described using the complex relative dielectric constant [50]:

$$\epsilon_r = \epsilon_r' - i\epsilon_r'' = \epsilon_r' - \frac{i\sigma}{\omega\epsilon_0}, \tag{1.62}$$

where ϵ_0 is the permittivity of vacuum and σ denotes the conductivity caused by migrating charge carriers (the DC conductivity σ_{DC}) with a frequency dependent contribution associated with the dispersion of ϵ_r' (the AC conductivity σ_{AC}).

$$\sigma = \sigma_{DC} + \sigma_{AC} \tag{1.63}$$

The relative dielectric constant relates to the equivalent circuit parameters C_f and R_f by:

$$C_f = \frac{\epsilon_0 \epsilon_r' A_p}{d}, \tag{1.64}$$

$$R_f = \frac{d}{A_p \sigma}, \tag{1.65}$$

where A_p is the area of the deposited film and d its thickness. The losses caused by the non-zero conductivity are often expressed by means of the dielectric loss tangent tg δ:

$$\mathrm{tg}\ \delta = \frac{\epsilon_r''}{\epsilon_r'} = \frac{1}{\omega R_f C_f}. \tag{1.66}$$

2. Experimental setup

Experimental measurements presented in this work, were conducted in the laboratory of prof. Tichý at the Department of Surface and Plasma Science, Faculty of Mathematics and Physics, Charles University, Prague. At first, the basic arrangement of the the low-pressure plasma jet deposition system is described, which was used also for experiments with a planar magnetron. The construction of the probes and the equipment used for Langmuir probe measurements is discussed in 2.2 and 2.3, respectively. The subsequent sections describe the experimental details regarding the FHP measurements and in-situ impedance spectroscopy measurements.

2.1 Vacuum deposition system

The vacuum system with the low-pressure plasma jet is schematically depicted in Fig. 2.2. The system consists of a stainless steel vacuum chamber of cylindrical shape (diameter of 30 cm and height of 30 cm) constructed for UHV conditions. The pumping was provided by an oil-free pumping system consisting of a turbomolecular pump Pfeifer Vacuum TMU 521 P with the maximal pumping speed of 500 l/s for the Ar gas backed up with a rotary pump Leybold EcoDry M15 (15 m^3/s). Before experiments or deposition of films, the system was pumped down to a pressure below 10^{-4} Pa, which was monitored by a full-range gauge Pfeiffer Vacuum PBR 260 (measuring range $\approx 10^{-8} - 10^{5}$ Pa) composed of a combination of a Pirani and Bayard-Alpert hot cathode gauge. For monitoring of the argon pressure (eventually with admixture of oxygen) during experiments, the capacitance gauge Pfeiffer Vacuum CMR 263 was used. The pressure at the inlet of the backing pump was monitored by a Pirani gauge Pfeiffer Vacuum TPR 280. Argon gas of purity of 99.9996 % was used as the working gas for sputtering. For reactive sputtering the oxygen gas of 99.999 % purity was used. The flow of the argon gas was adjusted by flow controller MKS instruments 1259CC (with maximum controllable flow of 2000 sccm for N_2). The flow of oxygen gas was adjusted by flow meter MKS instruments MF1 (with maximum controllable flow of 10 sccm). Both the flow controllers were controlled by the MKS Type 247D Four-Channel Readout unit. The hollow-cathode plasma jet was mounted in horizontal position. The vacuum port at the back side of the vacuum chamber was used either for the probes or for the substrate holder and in both cases it was possible to adjust the position in the radial direction with respect to the plasma jet or magnetron axis as indicated in Fig. 2.2b. The distance between the probes or substrate holder and the plasma jet could be adjusted by moving the plasma jet in horizontal direction, which was provided by edge welded bellow with thread mechanism. For the experiments with planar magnetron, the circular magnetron Lesker TORUS with balanced high-strength magnetic field was mounted in the same system on the upper flange. The magnetron was equipped with a titanium

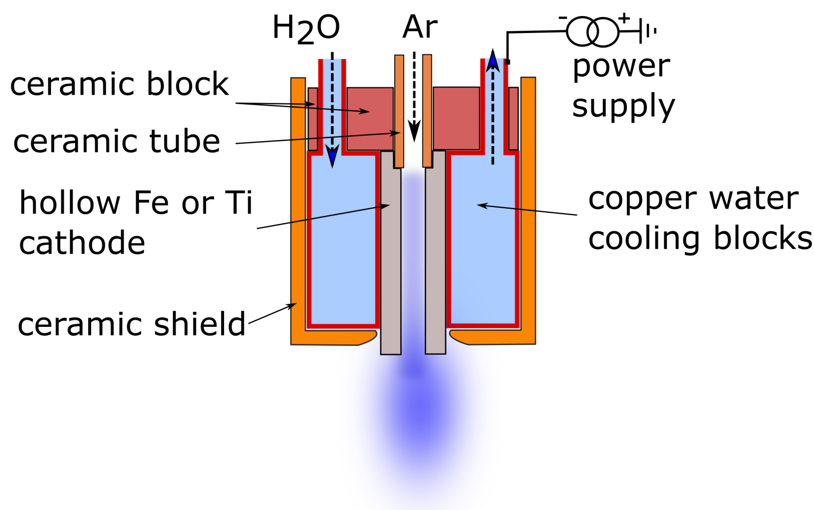

Figure 2.1: Scheme of the hollow-cathode plasma jet.

target (purity 99.995 %) of 5 cm in diameter and 6 mm thick. The distance of the magnetron to the probes or the sample holder could be adjusted by vertical position of the magnetron.

The scheme of the hollow-cathode plasma jet is shown is Fig. 2.1. The cathode has a tubular shape with length of 30 mm, outer and inner diameter of 8 mm and 5 mm, respectively. Depending on the particular experiment, the cathode was made either from iron with purity of 99.99 % or titanium with purity of 99.995 %. The cathode was squeezed between two copper blocks which were cooled by flowing water. The cathode was connected to the power supply through the cooling blocks and the tubes supplying the cooling water. This arrangement was possible due to a low conductivity of the common water from the water distribution network. The copper blocks were covered by a ceramic shield, so that they could not serve as a cathode and could not be sputtered. Only the argon gas was fed into the chamber through the hollow-cathode. The oxygen gas was introduced by a separate port to prevent the cathode from poisoning. Introducing oxygen gas directly into the hollow-cathode leads immediately to severe problems with the discharge stability.

The discharge was powered by means of a DC power supply Advanced Energy MDX 500 capable of providing of 500 mA, 500 W and 1.2 kV of maximal current, power and voltage, respectively. During continuously driven DC discharge, the negative output from the power supply was directly connected to the cathode of either the plasma jet or the magnetron and was operated as a constant current source. The grounded vacuum chamber served as the anode.

During experiments in pulsed DC discharge a pulsing unit was connected between the cathode and the power supply. The unit basically consists of a bank of capacitors and of an ultrafast switch constructed from IGBT transistors (insulated gate bipolar transistor). The detailed construction of the pulsing unit is described in [51]. The power supply was operated as a constant voltage source, which charged the capacitor bank. The frequency and duty cycle of the pulses

were controlled by pulses from a function generator Agilent 33220A. A 2Ω series resistor was already included in the pulsing unit. During magnetron discharge, the pulsing unit was directly (with the 2 Ω resistor) connected to the magnetron cathode. During the pulsed hollow-cathode discharge additional 4 Ω resistor was connected between the pulsing unit and the cathode in order to better protect the pulsing unit from possible electric sparks which could damage the pulsing unit. Moreover, for better stability of the pulsed hollow-cathode discharge a 2.2 kΩ resistor was connected parallel to the pulsing unit which causes a small (< 20 mA) DC discharge current to flow even in the pulse-off phase of the discharge.

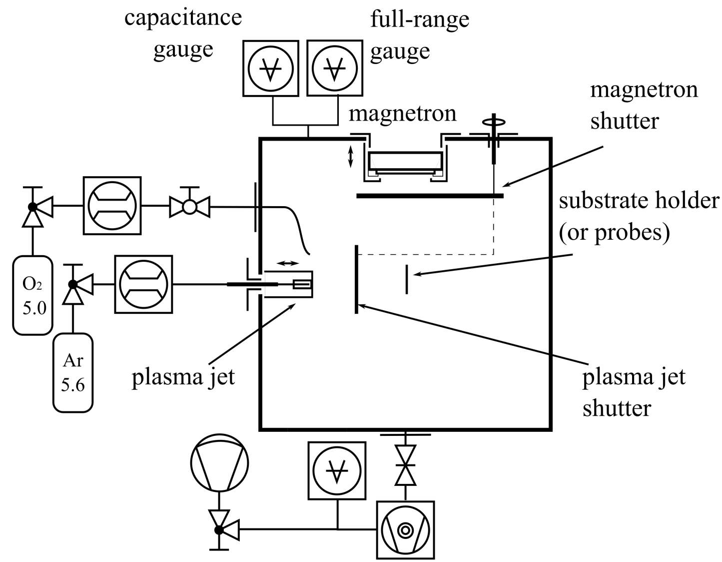

(a)

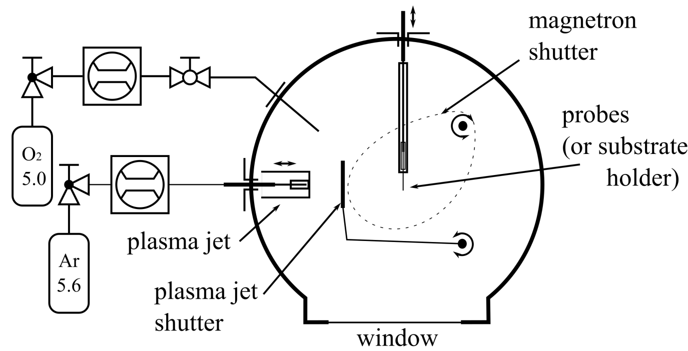

(b)

Figure 2.2: Basic scheme of the experimental system of the low-pressure plasma jet shown from the front view (a) and the top view (b). The planar magnetron has been mounted on the upper flange of the vacuum system. Note that the different objects are not drawn to scale.

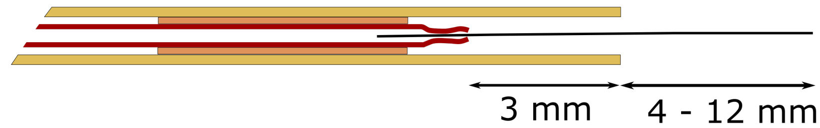

Figure 2.3: Schematic drawing of a cylindrical probe of 50 μm in diameter.

2.2 Construction of the probes

Cylindrical probes were used for plasma diagnostic measurements by means of the Langmuir probe method and the floating harmonic probe method. Typical construction of a probe is schematically depicted in Fig. 2.1. It was made of a tungsten wire of diameter of 50 μm which was inserted into a ceramic tube with outer diameter of 1.2 mm and inner diameter of 0.8 mm. The tungsten wire was inserted into one end of a thin copper tube, which was then squeezed to ensure a good electrical and mechanical contact. The copper tube was then connected to wire insulated by Teflon. The length of the probe, i.e. the part of the wire which was not shielded by the ceramic tube, ranged typically from 4 to 12 mm depending on the particular experiments. The tungsten wire was centered inside the ceramic tube, to avoid contact of the tungsten wire with the ceramic tube which gets covered by conducting layer of Fe or Ti during experiments without O_2. Furthermore, the probe was positioned perpendicular to the axis of the plasma jet (and parallel to the magnetron target) to minimize deposition inside the ceramic tube. During experiments with double probe, two probes were constructed in similar way and positioned next to each other with distance of about 5 mm between the tungsten wires.

The thick probe used in experiments discussed in Chapter 3 was constructed from a tungsten rod (800 μm in diameter) in a similar way, except from the fact, that the copper tube need not to be used. Larger ceramic shielding tube of outer diameter of 3 mm and inner diameter of 1.6 mm was used.

2.3 Langmuir probe measurement system

As the reference electrode for single Langmuir probes measurements served always the walls of the grounded vacuum chamber. For measurement of IV characteristics of Langmuir probe in the continuously driven DC discharge, Agilent B2901A SMU (source - measurement unit) was employed, which served as both the voltage source and the current measuring device. Moreover, it can be applied also for floating measurements; for example for measurement of IV characteristics of a double probe. The device was connected to a computer and controlled by means of the program Quick I/V Measurement Software provided by the device manufacturer.

For time resolved Langmuir probe measurements in pulsed discharge, an in-house constructed measurement system was used, based on the system used by Jan Klusoň, see [52]. Several parts of this system together with the controlling software were further modified by Zdeněk Turek, see [53]. The electronic circuitry

of this system is shown in Fig. 2.4. The voltage to the probe is supplied by a floating voltage source (± 60 V) so that the measurement is not burdened by noise present at the ground. The whole measuring system is controlled by a computer with a data acquisition card Adlink DAQe 2010 connected to PCI-Express bus. The probe voltage is adjusted by a 12bit D/A converter, the signal of which is optically transferred by means of an isolating amplifier ISO 100CP and amplified by a high voltage operational amplifier powered by the floating source. As the system is floating, the probe current must flow through the resistor in the feedback of the operational amplifier TL071, connected as a current to voltage converter. It was possible to choose from several values of resistors in the feedback by a switch and adjust the maximal range of the measured probe current. The signal from the current to voltage converter is sensed by a differential input of an A/D converter (14bit, 2MS/s) of the acquisition card.

The data acquisition card was controlled by a program developed in the graphical dataflow programming software Keysight VEE (formerly known as Agilent VEE). For a given probe voltage applied to the probe the system records the time evolution of the probe current during the active pulse and for some time after the active pulse with the sampling rate - one sample per 0.5 μs. The measurement was triggered by the same signal that was used for controlling the pulsing unit. Several current waveforms (typically 10) were recorded and averaged for a given probe voltage to reduce noise. This procedure is then repeated for different probe voltages with a constant voltage step. From the probe current waveforms measured at different probe voltages, IV characteristics for different instants during and after the active pulse are obtained.

2.4 Single FHP measurement system

For the measurements employing the single FHP technique described in 1.2.1, the electronic circuitry shown in Fig. 2.5 was made. The probe current was sensed on a 500Ω resistor and the current signal was amplified by a low noise, low bias current, high speed and high CMRR (common mode rejection ratio) instrumentation amplifier AD8421ARZ by a factor of 100–300. The gain of the differential input signal of the amplifier is adjusted by an external resistor R_G. The high CMRR allows extraction of low level signals even in the presence of common-mode signal. The negative feedback line in the operational amplifier NE5532 is hooked up at the end of the sensing resistor. This connection ensures that only the voltage of the fundamental frequency ω was applied on the probe and generation of voltage amplitudes of higher harmonic frequencies due to the voltage drop on the sensing resistor were suppressed. Such a connection is not needed, if the impedance of the sensing resistor is much lower that the impedance of sheath R_s. To let the probe floating and get it self-biased, a DC blocking capacitor of 15 μF was connected between the measuring circuitry and the probe. This capacitance was sufficiently high to render the voltage drop on the DC blocking capacitor negligible at all the used frequencies. In the experiments during measurement in pulsed discharges discussed in 4, measurements with different DC blocking capacitors of smaller capacitance was also preformed. The sinusoidal voltage $V_0 \cos \omega t$ of a given am-

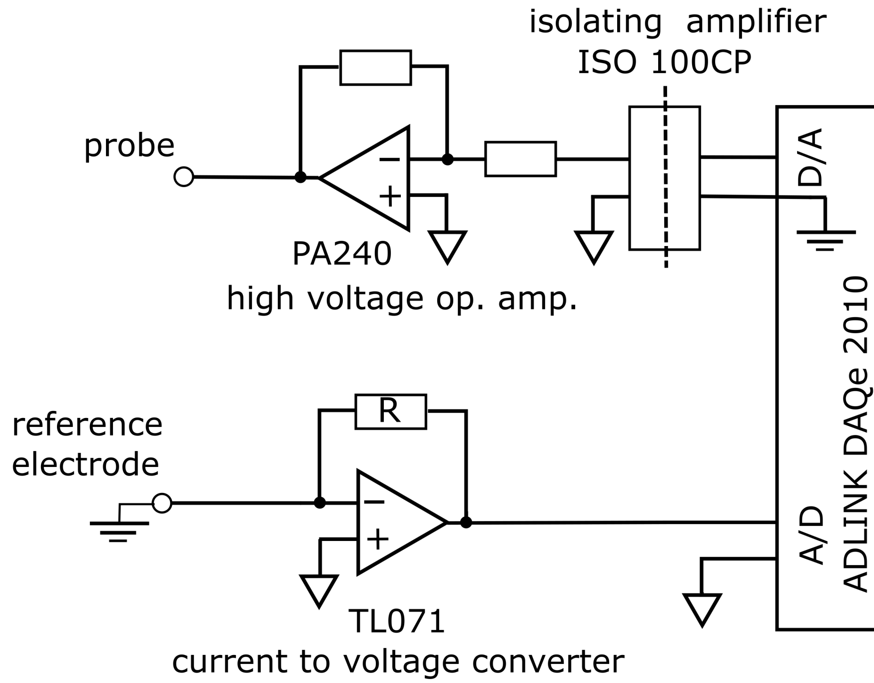

Figure 2.4: Principal scheme of the circuitry for time-resolved Langmuir probe measurement. The symbol of the triangle ∇ represents the common ground of the floating voltage source that is not shown in the scheme.

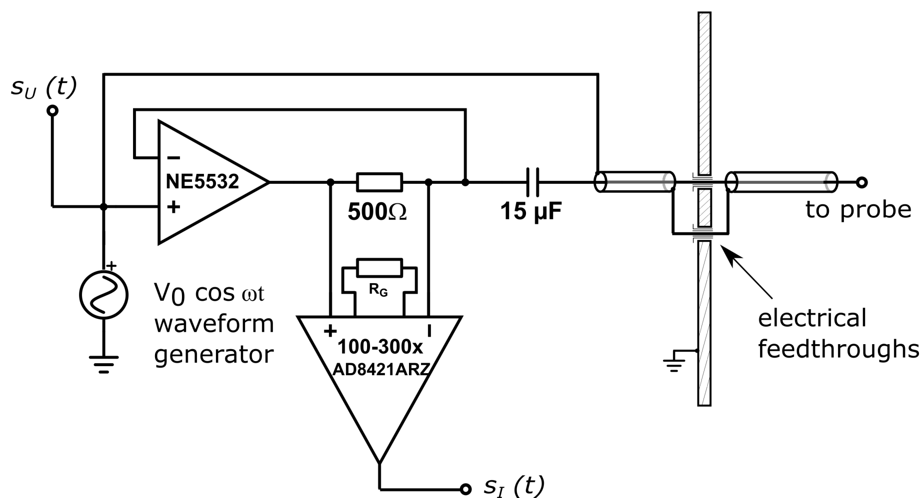

Figure 2.5: Scheme of the circuitry used for single floating harmonic probe measurement.

plitude and frequency was generated by a waveform generator Agilent 33250A. The measuring circuit was connected to the probe through a coaxial cable, with the outer shielding conductor being connected to the same AC voltage as the inner conductor. This shields the inner conductor from the plasma and minimizes the parasitic capacitive current of the inner conductor to ground.

The single-ended signal from the instrumentation amplifier was recorded by a 4 channel digital oscilloscope Agilent DSO-X 2004A with a maximum sampling rate of 2 GS/s (2×10^9 samples per second). However, the actual sampling rate of the obtained signal was lower according to the internal memory of the oscilloscope and the given time interval of measurement, which changed for different frequencies applied. The voltage waveform at the output of the waveform generator was also recorded.

When measuring in continuously driven discharge, typically 20 periods of the signal were acquired. Moreover, the oscilloscope was operated in the averaging acquisition mode that typically averaged over 64 waveforms (ensemble average). From the recorded voltage waveform $s_U(t)$ and current signal waveform $s_I(t)$, the precise amplitude of the applied voltage V_0 and amplitudes of the harmonic currents were obtained by means of the discrete Fourier transform as described in more detail in 2.6. The measured voltage waveform $s_U(t)$ was identical to the applied voltage to the probe. The circuit was calibrated with a resistor of 50 Ω in the frequency range 1 kHz - 1 MHz to obtain the calibrating coefficients which were used to evaluate the probe current from the measured current signal $s_I(t)$. The measurement procedure in pulsed discharges is described in 2.7.

When the discharge was off, a parasitic current of the fundamental frequency ω was observed. This parasitic capacity was evaluated to $C_p \approx 30$ pF and the parasitic current was being numerically subtracted from the obtained data.

2.5 Double FHP measurement system

For the measurement with the double FHP the electrical circuitry schematically depicted in Fig 2.6 was constructed. The system must be floating to be used for the double probe measurement. For coupling of the generated voltage to the floating part of the circuitry, the optocoupler HCNR201 is used. The optocoupler consists basically of one input LED (light emitting diode), one input photodiode and one output photodiode. The input photodiode intended mainly for feedback elimination of the non-linearity of the LED (see [54]) is not used and is not drawn in the scheme. A small sinusoidal voltage signal of given frequency ω is generated by the waveform generator Agilent 33250A together with a DC offset voltage of +3 V that is used to set the working point of the LED. The current signal from the photodiode is converted to voltage signal by the operational amplifier AD8058 connected as current to voltage converter. This voltage is amplified 10 times by the second operational amplifier. Both the operational amplifiers are powered by a floating voltage source of ±3 V consisting of two batteries. The DC current from the photodiode is compensated by current from the floating source. The probe current was sensed on a 10 Ω resistor, whose resistance could

be neglected compared to the impedance of the sheath, and amplified 100-1000x by the instrumentation amplifier AD8421ARZ. This is the same type of the instrumentation amplifier that was used also for single FHP measurement, see 2.4. The voltage applied to the double probe was sensed by a second instrumentation amplifier of the same type. Both the instrumentation amplifiers were powered by a grounded power source of ±18 V. The inputs of the instrumentation amplifiers can't be left floating, as some small DC bias current flowing from/to the inputs is needed for proper operation. Therefore, the floating part of the circuit was grounded through a 20 MΩ resistor. Moreover, the probes of the double probe were connected through DC blocking capacitors of 22 μF. This capacitance was sufficiently high to render the voltage drop on the DC blocking capacitors negligible at all the used frequencies. Moreover, the DC blocking was needed in order to compensate the possible difference in the plasma potentials $\Delta\Phi$ (or floating potentials) of the probes as explained in 1.2.3, see Fig. 1.5.

The amplitude of the sinusoidal voltage V_0 at the output of the circuit was approximately equal to the voltage amplitude generated from the waveform generator. The content of amplitudes of higher harmonic frequencies in the voltage at the output of the circuit was lower by more than 60 dB compared to the amplitude of the fundamental frequency when voltage amplitudes lower than 0.6 V were applied.

The signals from the instrumentation amplifiers were detected by the digital oscilloscope. Measurements in continuously driven discharges proceeded in a similar way as the measurement with single FHP described in 2.4. The measurement procedure in pulsed discharges is described in 2.7.

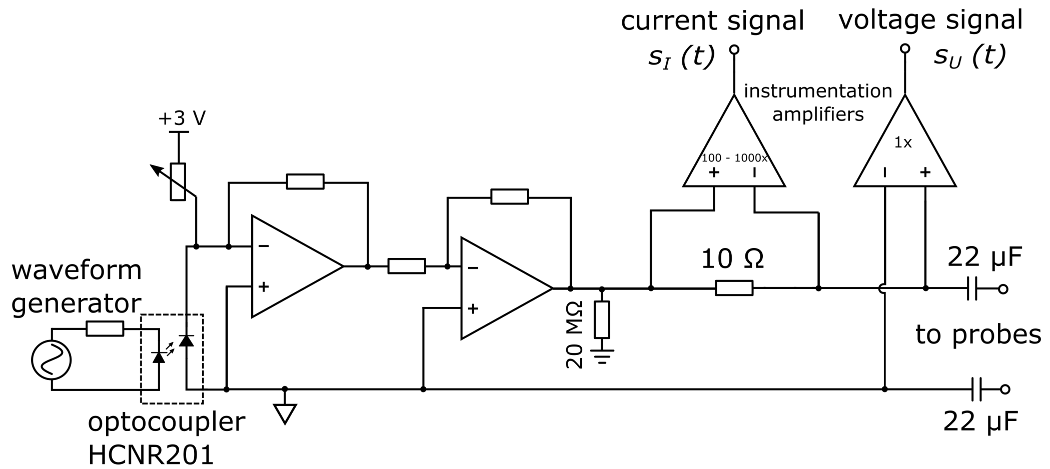

Figure 2.6: Scheme of the circuitry employed for measurement with the double FHP method. The symbol of the triangle ∇ represents the common ground of the floating voltage source of ±3 V (two batteries).

2.6 Evaluation of the waveforms

The waveform generator that was used for generating the sinusoidal signal to the probe and the digital oscilloscope were connected to a computer (by means of the USB bus) which controlled the applied voltage amplitude V_0, the frequency ω and retrieved the sampled voltage signal $s_U(t_k)$ and the current signal $s_I(t_k)$ waveforms measured by the oscilloscope. For this purpose a program written in the programming language Python (version 3) was employed. The complex amplitudes $\hat{U}, \hat{I}_{n\omega}$ of the signals at particular harmonic frequency $n\omega$ were evaluated according to the DFT (discrete Fourier transform) by computing the sum directly from the definition:

$$\hat{U} = \frac{2}{N} \sum_{k=1}^{N} s_U(t_k) \exp\left(-i\omega t_k\right), \tag{2.1}$$

$$\hat{I}_{n\omega} = \hat{C}_{n\omega} \frac{2}{N} \sum_{k=1}^{N} s_I(t_k) \exp\left(-in\omega t_k\right), \tag{2.2}$$

where i represents the imaginary unit, $i^2 = -1$, N the number of samples and $\hat{C}_{n\omega}$ a complex calibration factor that was obtained by calibrating the particular measuring circuit using a resistor of 50 Ω. The voltage signal s_U was already equal to the actual applied voltage to the probe. Note, that the sampled data need not be multiplied by any special window function, hence basically, the rectangular window function was used. Moreover, the simple rectangular window has the lowest equivalent noise bandwidth of all the windows, i.e. the rectangular window achieves lowest noise accumulated due to the spectral leakage, see [55]. The following simple relationships apply to the AC voltage amplitude V_0 and probe harmonic currents $i_{n\omega}$:

$$\begin{aligned} V_0 &= \left|\hat{U}\right| \\ i_{n\omega} &= \left|\hat{I}_{n\omega}\right|. \end{aligned} \tag{2.3}$$

In the in-situ impedance measurements, the measured complex impedance Z_m was evaluated simply as:

$$Z_m = \frac{\hat{U}}{\hat{I}_{1\omega}} \tag{2.4}$$

2.7 Phase delay harmonic analysis method

Due to the sheath capacitance and partially also due to the parasitic capacitances of the measuring circuitry and electrical leads to the probe, which also complicate the measurement, the operating frequency of the input ac voltage is limited to roughly about 100 kHz. Even if just one period of the applied signal was used to evaluate the plasma parameters, the temporal resolution in this case couldn't be better than roughly about 10 μs, which is still too much to reliably capture the changes during 100 μs and/or shorter HiPIMS pulses.

An alternative measurement technique named PDHAM – Phase Delay Harmonic Analysis Method was recently proposed in [11]. Similarly to the conventional time-resolved Langmuir probe method, it is assumed that the plasma is

generated repeatedly with reproducible parameters and that, consequently, measurement during several discharge periods can be used for obtaining the temporal evolution of the plasma parameters.

In this method the AC input voltage is synchronized with the triggering signals of the discharge pulses. In the first trigger the AC voltage with no phase delay is applied to the probe and the probe current is measured. In the subsequent triggers the applied voltage is incrementally delayed by some integer phase fraction of 2π. After several discharge pulses when reaching the phase delay of 2π, one period of the applied voltage can be reconstructed in the phase domain at any time sampled during the discharge period as illustrated in Fig. 2.7. Similarly, the corresponding one period current waveform can be reconstructed in the phase domain. The one period waveform is then used for the evaluation of the harmonic currents according to Eq. 2.2 and the transient current i_t as the average value of the current waveform. The electron temperature and ion number density can be then evaluated according to the theory of the FHP (1.2.2) or double FHP (1.2.3). The time resolution in this case is limited by the sampling frequency during recording of the current waveforms by the oscilloscope (i.e. possibly also by the internal memory of the oscilloscope), and by the ion plasma frequency (similarly to the conventional Langmuir probe method).

The harmonic signal of given frequency was supplied by the waveform generator Agilent 33220A, synchronized with the triggering pulses controlling the discharge pulses and operating in the so-called burst mode. In this mode only several periods of the harmonic input voltage fitting in the discharge period were generated after the pulse trigger. Moreover, the phase of the signal can also be easily adjusted. The oscilloscope (triggered by triggering pulses controlling the discharge pulses) was operated in the averaging acquisition mode that averaged typically over 32 waveforms (ensemble average). Both the waveform generator and the oscilloscope were connected to a computer which automatically controlled the whole measurement – controlling the incremental change of the input voltage phase and retrieving the waveform data from oscilloscope. From the current waveforms in the time domain the waveforms in the phase domain were then constructed, from which the amplitudes of the harmonic currents were obtained by means of the DFT as described in 2.6.

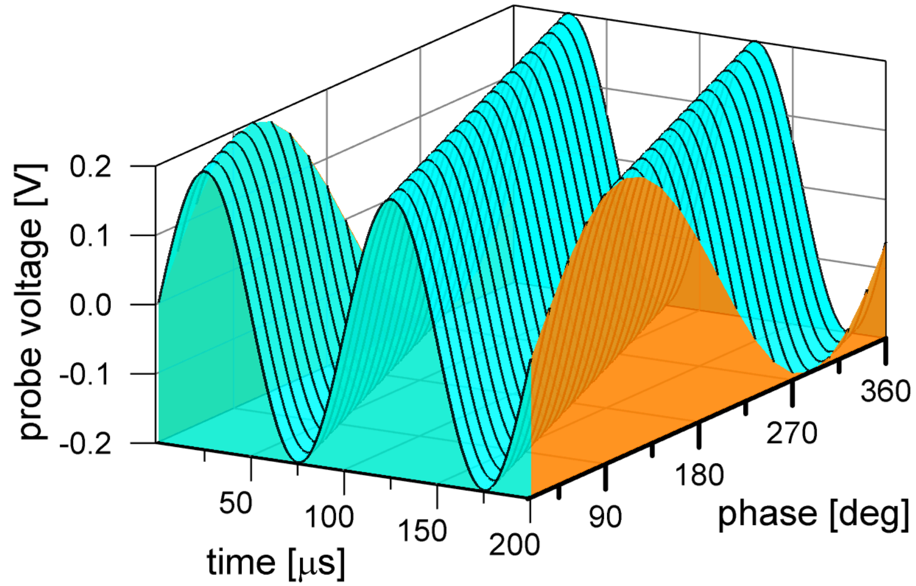

Figure 2.7: Illustration of several 10 kHz AC harmonic input voltage waveforms with different phase delays. One period of the voltage signal can be reconstructed in the phase domain at any time sampled during the discharge period.

2.8 In-situ impedance spectroscopy

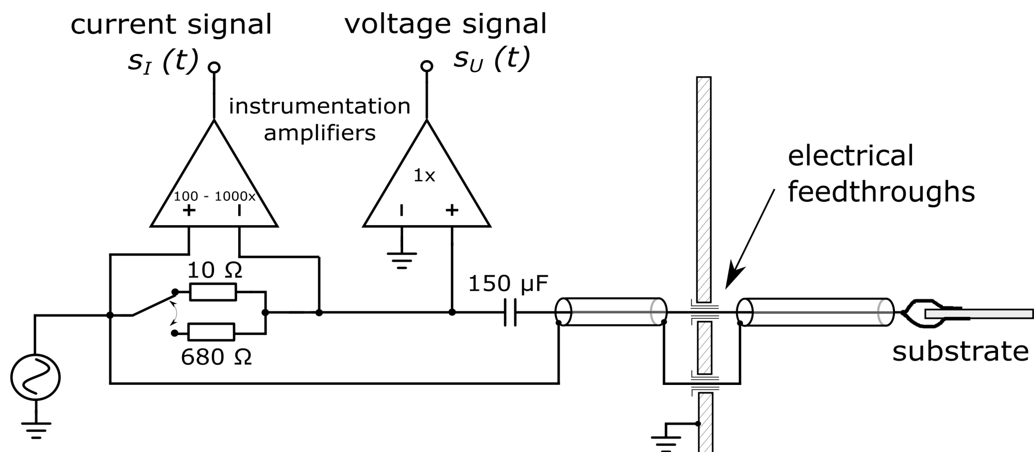

Figure 2.8: The scheme of the circuitry employed for in-situ impedance spectroscopy measurements. The connection to the substrate by a coaxial cable through the vacuum chamber is also shown.

For the in-situ impedance spectroscopy measurements the electrical circuitry depicted in Fig. 2.8 was used. A sinusoidal signal generated from the waveform generator Agilent 33220A was applied. The current was sensed either on a 10Ω resistor or 680Ω resistor which could be switched in order to cover the high range of current magnitudes to be measured. The instrumentation amplifiers AD8421ARZ were used in the same manner as for the double probe measuring circuit, see 2.5. A capacitor bank of approximately 150 μF was used as the DC blocking capacitor.

The measuring circuit was connected to the substrate through a coaxial cable, with the outer shielding conductor being connected to the same AC voltage as the inner conductor. This shields the inner conductor from the plasma and minimizes the parasitic capacitive current of the inner conductor to ground. Therefore, most of the parasitic capacitance was caused by the measuring circuit. The parasitic capacitance of $C_p \approx 30$ pF has been measured with plasma off. As a signal-recording device the digital oscilloscope Agilent DSO-X 2004A was used. Both the waveform generator and the oscilloscope were connected to a computer, which in a programmed way performed the frequency scan, i.e. controlled the frequency of the waveform generator and retrieved the waveform data of current and voltage signals from the oscilloscope. For this purpose a program in Python (version 3) has been written. At frequencies higher than approximately 1 kHz the waveform acquisition was performed with averaging over 32 waveforms (ensemble average, waveform-to-waveform averaging). In order to perform the measurement of one frequency scan fast enough, at the frequencies lower than approximately 1 kHz, I have utilized averaging using the oversampled data in the High resolution acquisition mode of the oscilloscope (sample-to-sample averaging), which also yields higher number of bits of resolution. At the lower frequencies only a few periods of the signal were recorded, typically 3 or 5 periods. At higher frequencies more periods were recorded, typically from 20 to 60 periods. One impedance frequency scan was performed always beginning at 1 MHz and going down to 1 Hz. As the frequency was decreased, the current signal decreased due to the increasing impedance of the deposited film. When the current signal was too low, the 680Ω resistor was used instead of the 10Ω resistor by manually switching the switch.

The complex impedance Z_m was obtained from the DFT as described in 2.6 according to Eq. 2.4. The measuring circuit has been calibrated using a 50Ω resistor. To obtain the equivalent circuit impedance Z, the impedance of the DC blocking capacitor (which may influence the measurement at low frequencies) and the effect of the parasitic capacitance (which influences the measurement at high frequencies) was numerically subtracted by this simple formula:

$$\frac{1}{Z} = \frac{1}{Z_m - 1/\left(i\omega C_B\right)} - i\omega C_p, \tag{2.5}$$

where $C_B \approx 150\mu$F is the capacitance of the blocking capacitor and $C_p \approx 30$ pF the parasitic capacitance measured when the discharge was turned off.

As the dependence of the various parameters (C_f, R_f, ϵ_r' etc.) on the measured

impedance Z_m is not trivial, it is of great importance to observe, to what extent the obtained parameters are valid considering certain error in the measurement of Z_m. I have chosen the following maximal errors considering the estimation of the phase $\arg(Z_m) = \varphi_m$ and the absolute value $|Z_m|$ of the measured impedance: $\Delta|Z_m| = \pm 4$ %; $\Delta\varphi_m = \pm 0.5°$ (for frequencies lower than 10 kHz), $\Delta\varphi_m = \pm 1.5°$ (for frequencies higher than 10 kHz).

An error of a specific parameter was evaluated without estimating the analytical form of the partial derivatives, yet a computer calculation method was used, see [56]. Assuming, that the parameter to be estimated, e.g. R_f, is calculated by a function $R_f = R_f(|Z_m|, \varphi_m, ...)$, the maximal error ΔR_f is then evaluated as:

$$\Delta R_f = |a| + |b| + ...$$

$$a = R_f(|Z_m| + \Delta|Z_m|, \varphi_m, ...) - R_f(|Z_m|, \varphi_m, ...)$$

$$b = R_f(|Z_m|, \varphi_m + \Delta\varphi_m, ...) - R_f(|Z_m|, \varphi_m, ...)$$

The error evaluated by this method is shown as an error bar. The error caused by the remaining noise present on the recorded waveforms is not covered in the error bars, yet it is apparent from the scatter of the data. The accuracy of the measurement was tested on various discrete resistors and capacitors. One example of the measured impedance spectra (corrected on the parasitic capacitance and DC blocking capacitance according to Eq. 2.5) obtained when the circuit was tested on discrete components is shown in Fig.2.10. A discrete capacitor of capacitance of approximately 9 pF in parallel with a resistor of approximately 14.8 kΩ was connected at the end of the coaxial cable at the point where the substrate is normally connected and the other end was connected to the grounded vacuum chamber, i.e. simulating the linearized plasma sheath impedance. The obtained impedance data were fitted with the expected model of an ideal resistor in parallel with an ideal capacitor. The fitted spectrum lies within the error bars and perfectly agrees with the measured data in the whole range of frequencies, see Fig. 2.10. The capacitance and resistance obtained from the fit (9 pF and 14.7 kΩ) is in agreement with the values of the discrete components used. Similar testing measurements were performed with various testing resistors up to 10 MΩ.

The spectra were fitted by means of the Levenberg-Marquardt algorithm (using the function optimize.leastsq from the Python's Scipy library [57]. The sum of the squares of the differences of the real parts and imaginary parts of the impedance were minimized.

As the substrate/electrode served an FTO (fluorine-doped tin oxide) coated sodalime glass (sheet resistance of 15 Ω, Solaronix) substrate 2x1 cm in dimension. Approximately one half of the substrate was used to make a connection to the conducting FTO layer, see Fig. 2.8, which was isolated from the plasma by at least 0.8 mm thick layer of Teflon (PTFE) tape, see Fig. 2.9. The area of the remaining part of the FTO substrate exposed to plasma, on which the film was deposited, was approximately between 1x0.7 cm^2 and 1x0.8 cm^2. The deposited area of the film was more precisely deduced from a photo of the deposited film. The temperature of the substrate was monitored by a thermocouple positioned near the electrical connection to the substrate. In order to test the Teflon and

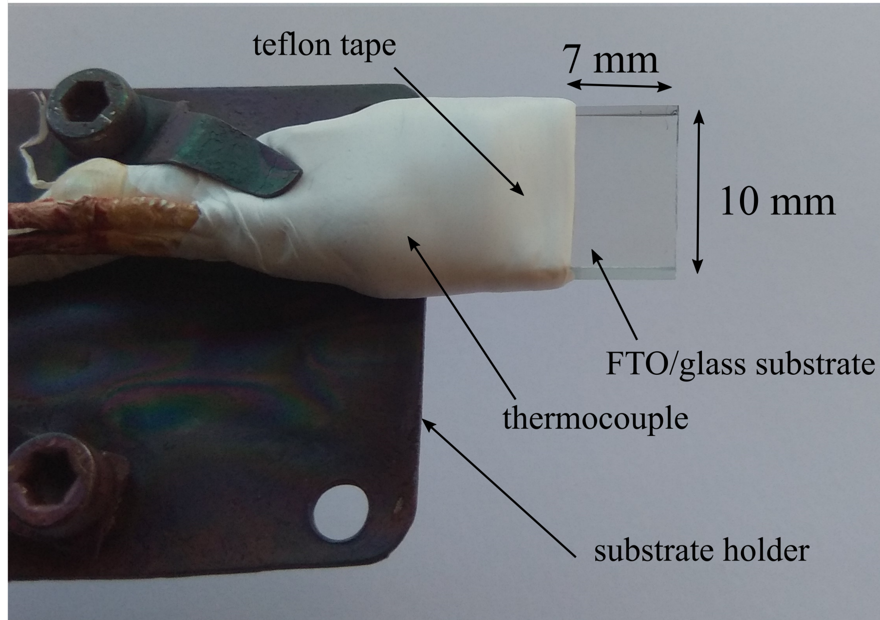

Figure 2.9: Photo of the substrate holder together with the glass/FTO substrate connected to the measuring circuit before deposition. The connection is insulated by a Teflon tape.

cable insulation, I have insulated the whole glass/FTO substrate. In such a case, no difference in the measured spectra in the whole range of frequencies (1 Hz - 1 MHz) and substrate temperatures (up to 100 °C) was observed when the discharge was turned on compared to the spectrum when the discharge was off.

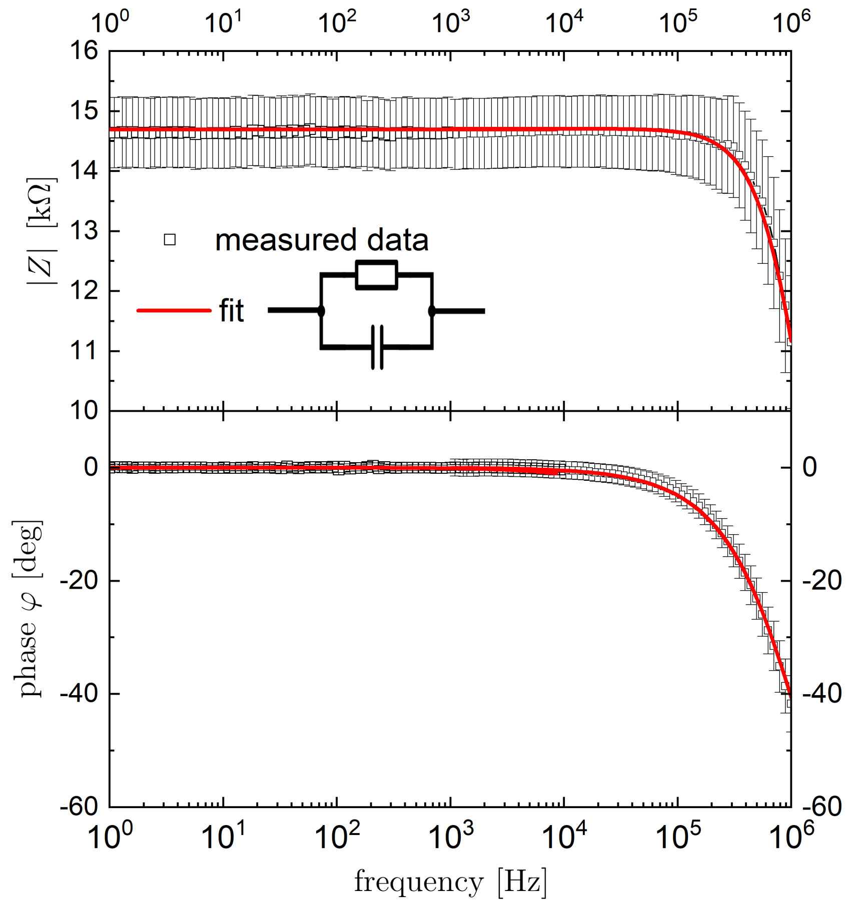

(a)

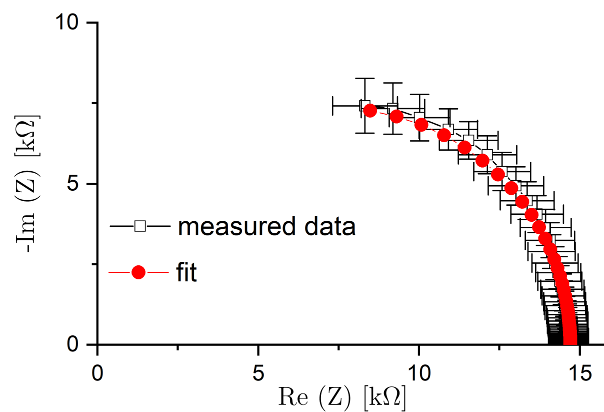

(b)

Figure 2.10: Measured impedance spectrum of a parallel connection of 9 pF capacitor and 14.8 kΩ resistor: (a) Bode plot (b) Nyquist plot. The red line depicts the fitted model data.

3. FHP measurements in continuous DC regime

The purpose of these experiments was to assess the accuracy of the FHP method in comparison with a standard LP and show the applicability of the FHP during reactive sputtering, when an insulating layer of iron oxide is deposited on the probe. The experiments were performed in the hollow-cathode plasma jet DC discharge with a Fe cathode.

To study the FHP method I have chosen to use cylindrical probes, as they can be easily constructed small enough to achieve a good spatial resolution. Typically, however, the ion current in the ion saturation region of a thin cylindrical probe is not constant as the simple theory of FHP presumes. In order to make the experiment as general as possible and study also the influence of the non-constant ion current, two cylindrical probes of different diameters were used: one 4.4 mm long and of diameter 50 μm (hereafter called the thin probe) and 3.4 mm long and 800 μm in diameter (hereafter called the thick probe). Both the probes were studied simultaneously and were positioned next to each other (with a distance of approximately 5 mm) in the plasma plume at the system axis at the distance of 4 cm downstream from the nozzle exit perpendicular to the plasma flow. Both probes were used in the FHP regime as well as in the regime of a standard LP.

As the measurement with the LP method in the reactive sputtering regime is hampered by the deposition of the insulating film, the comparative measurements of the plasma parameters obtained from the FHP data and LP method discussed in the following three sections (3.1, 3.2, 3.3) were performed in the nonreactive regime without oxygen, i.e. in argon discharge only. In section 3.4 I discuss the FHP probe measurements in the reactive regime when an iron oxide film was deposited on the probe.

3.1 Dependence on the amplitude of the applied voltage

The following measurements of the dependence of the FHP data on the AC voltage amplitude V_0 applied to the probe were performed at a fixed frequency of the applied voltage of 20 kHz at argon gas pressure 7 Pa, argon flow 120 sccm and discharge current 300 mA.

The electron temperature was evaluated according to Eq. 1.32 from the ratio of amplitudes of harmonic currents $i_{1\omega}/i_{2\omega}$ and $i_{2\omega}/i_{3\omega}$ and is depicted in Fig. 3.1. For both the probes, the electron temperature evaluated from the ratio $i_{2\omega}/i_{3\omega}$ is slightly lower than that obtained from the ratio $i_{1\omega}/i_{2\omega}$ and can be said to be in a very good agreement with the electron temperature obtained from the IV characteristics, which equals to approximately 0.13 eV. As in fact the ion current in the ion saturation region is not constant, besides the AC electron current, some AC ion current is also generated, which adds to the AC electron current

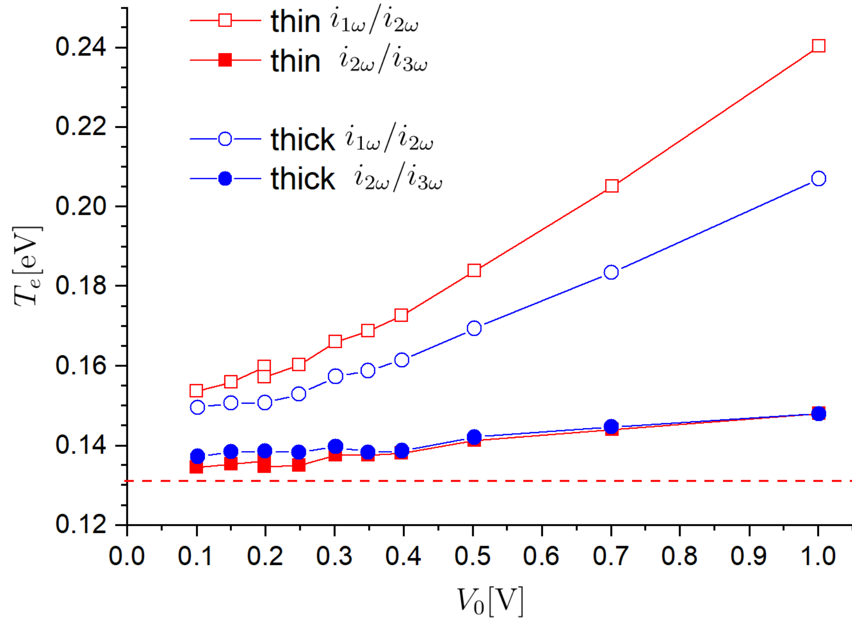

Figure 3.1: Electron temperature estimated from the ratio of harmonic currents $i_{1\omega}/i_{2\omega}$ and $i_{2\omega}/i_{3\omega}$ measured by the thin and thick probe in dependence on the applied voltage amplitude V_0. The dashed horizontal line depicts the electron temperature obtained from IV characteristics.

and increases the respective measured harmonic current amplitudes. The relative contribution of the AC ion current is highest for the current of the fundamental frequency, $i_{1\omega}$, and therefore the ratio $i_{1\omega}/i_{2\omega}$ is more affected by the AC ion current than the ratio $i_{2\omega}/i_{3\omega}$. The ratios of harmonic currents in dependence on the AC voltage amplitude V_0 are shown in Fig. 3.2 together with the theoretical dependencies as given by Eq. 1.32 evaluated using the reference temperature from IV characteristics of 0.13 eV. The values of $i_{2\omega}/i_{3_\omega}$ are in good accord with the theoretical curve; the values of the ratio $i_{1\omega}/i_{2\omega}$ are higher than the theoretical dependence and consequently correspond to higher electron temperatures. Notice, that according to Fig. 3.2 and Fig. 1.3, a deviation in the harmonic current ratio leads to a higher deviation in the estimated electron temperature for higher voltage amplitudes V_0. That is most likely the main reason for the relatively steep dependence of the electron temperature evaluated from the ratio $i_{1\omega}/i_{2\omega}$ on the AC voltage amplitude observed in Fig. 3.1. Somewhat surprisingly, there is not much difference between the thick and the thin probe in the slope of the trends. Another contribution to the dependence of the evaluated electron temperature on the AC voltage amplitude is the self-biasing effect. Increasing the applied AC voltage leads to a shift of the DC potential of the probe to more negative values, see Eq. 1.36 and Fig. 1.4. At last, the measurement might be also affected by a possible non-Maxwellian tail of the EEDF. However, in the particular measurement shown in Fig. 3.1, the electron temperature data evaluated from the ratio $i_{2\omega}/i_{3\omega}$ show only little dependence on the AC voltage amplitude.

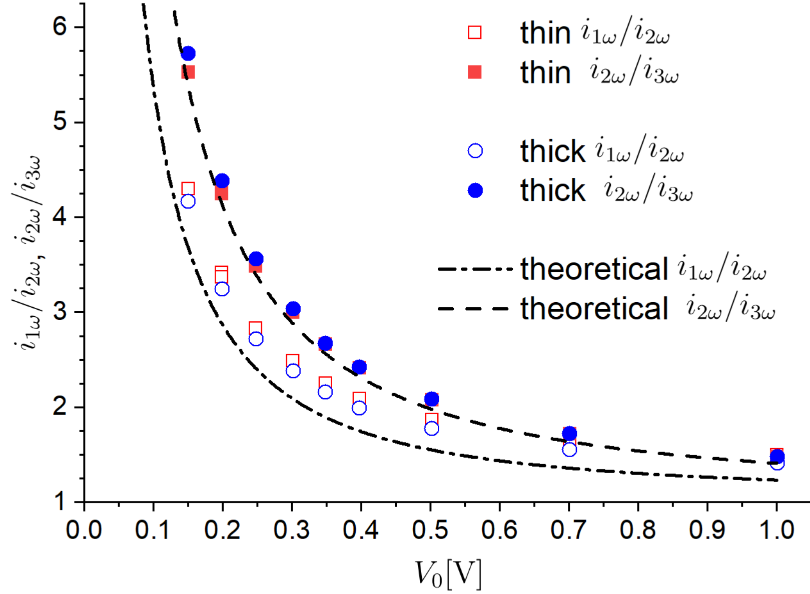

Figure 3.2: The measured ratios of amplitudes of harmonic currents $i_{1\omega}/i_{2\omega}$ and $i_{2\omega}/i_{3\omega}$ from both the thin and thick probe in dependence on the applied AC voltage amplitude V_0. The black lines depict the theoretical dependencies according to Eq. 1.32 evaluated using the reference temperature from IV characteristics of 0.13 eV.

In order to obtain the ion density n_i from the FHP data, the ion current I_i needs to be evaluated first using Eq. 1.34. Fig. 3.3 and Fig. 3.4 show the ion current I_i of the thin and thick probe, respectively, evaluated from the harmonic currents $i_{1\omega}$, $i_{2\omega}$ and $i_{3\omega}$ in dependence on the AC voltage amplitude V_0. The electron temperature of 0.13 eV was used in the calculation of the ion current. The error bars depict a theoretical error in the ion current estimation, when an error of ±5 % in the electron temperature is supposed. This error decreases with increasing AC voltage amplitude and is higher when the ion current is evaluated from currents of higher harmonic frequencies. For both the probes, the ion current estimated from the $i_{1\omega}$ is higher than that obtained from $i_{2\omega}$ and $i_{3\omega}$. That can be attributed to the contribution of the AC ion current predominantly to the AC current of the fundamental frequency $i_{1\omega}$.

From Fig. 3.3 and Fig. 3.4 it is apparent, that the ion current estimated from all the three harmonic currents linearly increases with a similar slope with increasing the applied AC voltage amplitude. For comparison, in both the figures the ion current obtained from the respective IV characteristics is shown. The Laframboise theory of the ion current was used, in order to extrapolate the ion current from the ion saturation region and evaluate the ion current near the floating potential, see Fig. 3.6 and Fig. 3.7. The ion current from the IV characteristics was then evaluated at probe voltages shifted from the floating potential

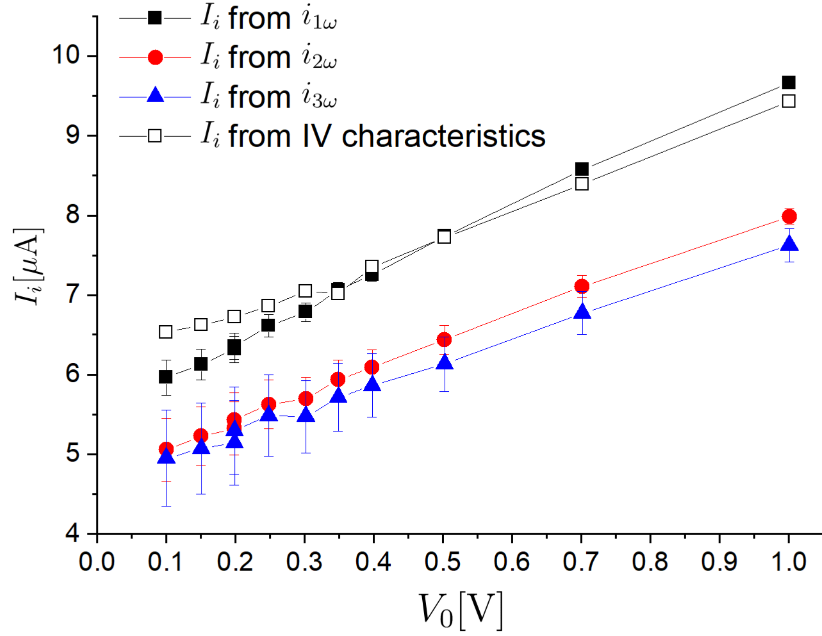

Figure 3.3: Ion current I_i to the thin probe estimated from the harmonic current amplitudes $i_{1\omega}$, $i_{2\omega}$ and $i_{3\omega}$ in dependence on the AC voltage amplitude V_0. The open squares depict the ion current estimated from the IV characteristics of the thin probe shown in Fig. 3.6 taking into account the self-biasing effect.

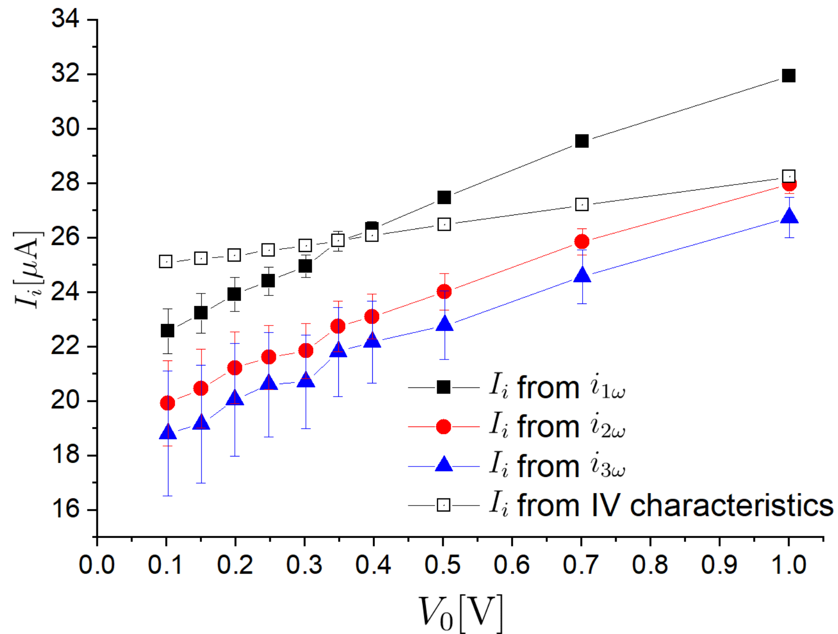

Figure 3.4: Ion current I_i to the thick probe estimated from the harmonic current amplitudes $i_{1\omega}$, $i_{2\omega}$ and $i_{3\omega}$ in dependence on the AC voltage amplitude V_0. The open squares depict the ion current estimated from the IV characteristics of the thick probe shown in Fig. 3.7 taking into account the self-biasing effect.

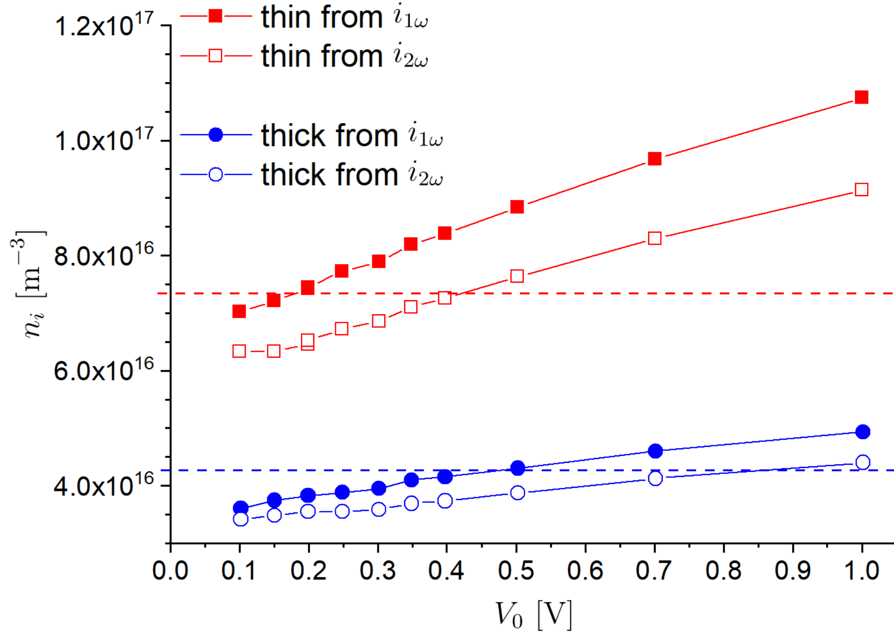

Figure 3.5: The ion density according to the Laframboise theory obtained from the thin and thick probes employing the FHP method using $i_{1\omega}$ and $i_{2\omega}$ in dependence on the amplitude of the applied AC voltage. The dashed lines depict the ion density obtained from the respective IV characteristics according to the Laframboise theory with the working point chosen at $\Phi - 20k_BT_e/e$.

by a voltage given by the self-biasing effect according to Eq. 1.36. For both the probes, the ion current obtained from the current of the fundamental frequency $i_{1\omega}$ is in better agreement with the ion current from the IV characteristics than the ion current evaluated from $i_{2\omega}$ and $i_{3\omega}$. In the case of the thin probe, the slope of the ion current data from the IV characteristics is comparable to the slope of the ion current evaluated from the harmonic currents. This result suggests, that the increase of the harmonic currents with increasing the AC voltage amplitude could be related mainly to the self-biasing effect. In the case of the thick probe, the relative increase of the ion current according to the IV characteristics of the thick probe is lower compared to the thin probe. That is related to the fact, that the increase of the effective collecting probe area due to the expansion of the sheath layer has lower effect on the relative increase of the collected current for the thick probe compared to the thin probe. However, it can be clearly seen in Fig. 3.4, that the ion current data from the harmonic currents of the thick FHP increase much steeper with the AC voltage amplitude than does the ion current data from the IV characteristics. Hence, on the contrary, the results from the thick probe suggest, that the increase of the evaluated ion current with increasing the AC voltage amplitude can't be explained by the self-biasing effect only.

In order to obtain the ion density from the ion current measured by FHP, the numerical procedure described in 1.1.3 was applied. The working point was chosen to be $\Phi - 5.19k_BT_e/e$, i.e. a value of the floating potential in argon

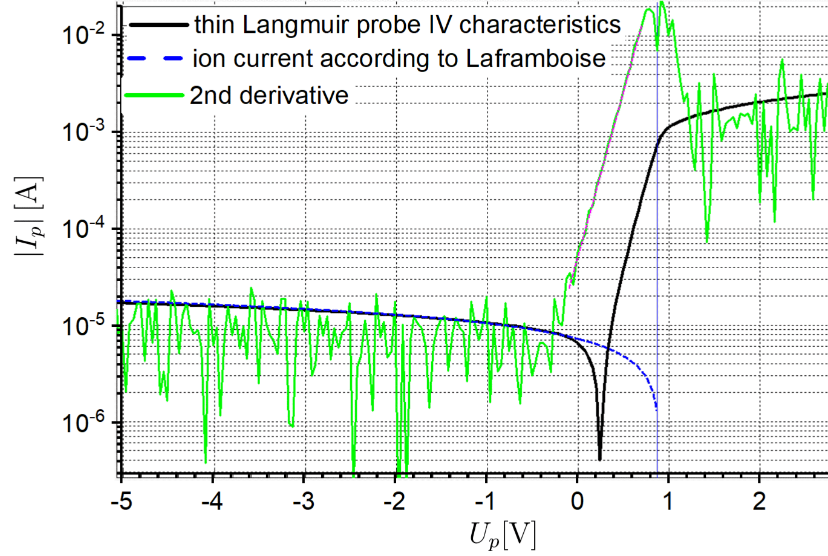

Figure 3.6: The IV characteristics of the thin probe (black line); the absolute value of the probe current in logarithmic scale is shown. The green line represents the 2nd derivative of the IV characteristics and the blue dashed line depicts the ion current according to the Laframboise theory.

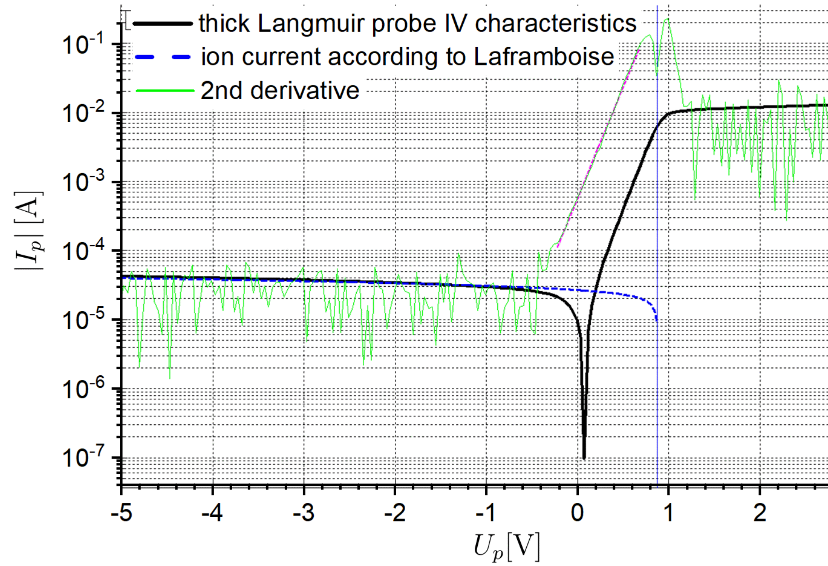

Figure 3.7: The IV characteristics of the thick probe (black line); the absolute value of the probe current in logarithmic scale is shown. The green line represents the 2nd derivative of the IV characteristics and the blue dashed line depicts the ion current according to the Laframboise theory.

plasma derived for planar probe, see Eq.1.17. Furthermore, the shift of the DC potential of the FHP probe due to the self-biasing effect was neglected. Fig. 3.5 shows the ion density according to the Laframboise theory evaluated from $i_{1\omega}$

and $i_{2\omega}$ from both the probes. The temperature obtained from $i_{2\omega}/i_{3\omega}$ was used for the calculation of the ion density instead of the temperature from LP, which causes, that equations Eq. 1.34 for $k = 2, 3$ are then not independent, and the ion density (and also ion current) evaluated from $i_{2\omega}$ and $i_{3\omega}$ are equal. Practically, the evaluated ion density in dependence on the AC voltage amplitude follows the same trend as do the corresponding ion currents as discussed above. Notice, that the ion density determined from the thick probe by both the FHP and LP method, is approximately two times lower, than that from the thin probe. The discussion of this discrepancy is made in section 3.3.

3.2 Dependence on the frequency of the applied voltage

The dependence of the electron temperature and the ion density determination on the frequency of the applied AC voltage was also investigated; the results can be seen in Figs. 3.8 and 3.9. The measurements were performed at a fixed AC voltage amplitude of 0.25 mV, at argon gas pressure 5 Pa, argon flow 100 sccm and discharge current 300 mA.

It follows from the obtained data, that in the studied frequency range the electron temperature evaluated from $i_{2\omega}/i_{3\omega}$ and ion density evaluated from $i_{2\omega}$ can be said to be almost independent of the AC voltage frequency. On the other hand, these plasma parameters obtained from $i_{1\omega}/i_{2\omega}$ and $i_{1\omega}$ increase with the increasing frequency of the AC voltage. This increase is pronounced especially for frequencies larger than 100 kHz for both the thick and thin probe. The increase of the obtained values with frequency can be explained by the increase of the first harmonic current due to the sheath capacitance, i.e. the right part of the inequality in Eq. 1.38 at higher frequencies is not fulfilled. The results displayed indicate that the electron temperature obtained from the ratio $i_{2\omega}/i_{3\omega}$ corresponds reasonably well to the electron temperature obtained from the standard LP characteristics (the data from the thin and the thick LP correspond to each other; indicated by red dashed line) and that it does not seem to be influenced by the sheath capacitance in the studied frequency range. The fact, that the thick probe underestimates the ion density compared to the thin probe is discussed in 3.3.

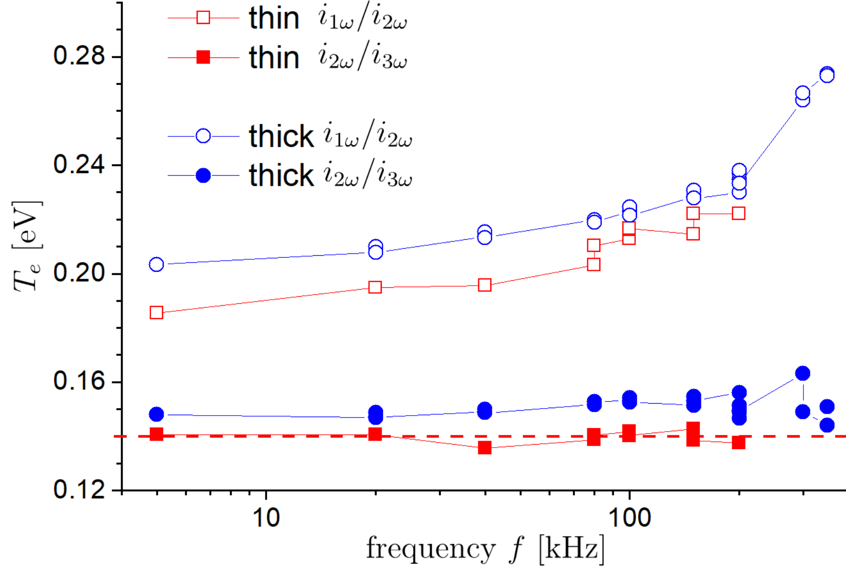

Figure 3.8: Electron temperature estimated from the ratio of harmonic currents $i_{1\omega}/i_{2\omega}$ and $i_{2\omega}/i_{3\omega}$ measured by the thin and thick FHP in dependence on the frequency of the applied AC voltage. The dashed horizontal line depicts the electron temperature obtained from IV characteristics.

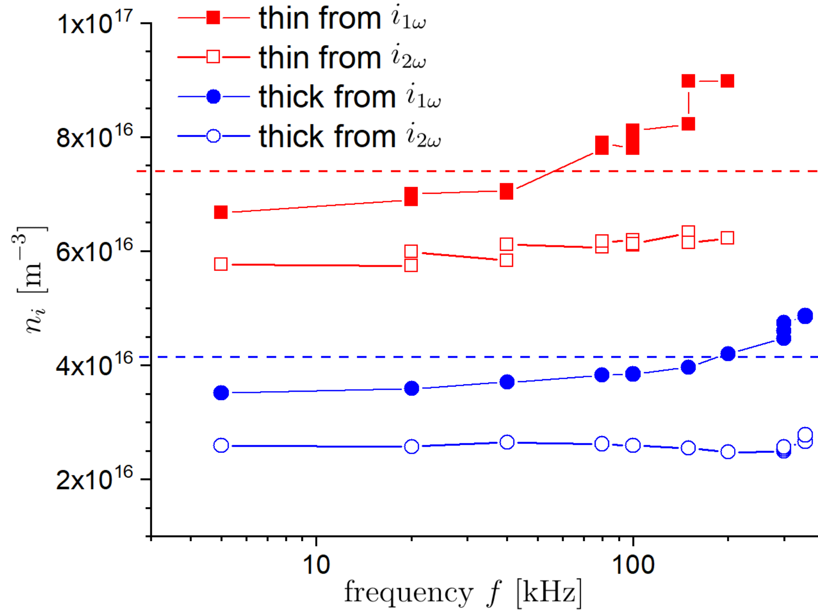

Figure 3.9: The ion density according to the Laframboise theory obtained from both the thin and thick FHP using $i_{1\omega}$ and $i_{2\omega}$ in dependence on the amplitude of the applied AC voltage. The dashed lines depict the ion density obtained from the respective IV characteristics according to the Laframboise theory with the working point chosen at $\Phi - 20T_e$.

3.3 Comparison of FHP and LP - pressure scan

The accuracy of the FHP method compared to the LP method was studied also in a wider range of discharge conditions, as the argon gas pressure in the chamber was varied. The argon gas flow through the plasma-jet was set constant at 120 sccm and the pressure was adjusted by opening and closing the gate valve between the chamber and the turbomolecular pump. The discharge current was set constant at 300 mA. The FHP measurement shown were performed with the AC voltage amplitude 0.25 mV and frequency 20 kHz.

The comparison of the measured electron temperature as the pressure inside the chamber was varied is shown in Fig. 3.10. For clarity, the electron temperature from the thick LP is not shown, as it was in a very good agreement with the electron temperature obtained from the thin LP. The EEPFs determined from the 2nd derivative of the thin probe at two pressures of 1.5 Pa and 5 Pa are shown in Fig. 3.11. The EEDF determined for pressures higher than about 2 Pa, can be reasonably well described by a Maxwellian distribution with the electron temperatures about 0.11 - 0.13 eV in the entire range of energies where the obtained EEDF can be trusted. For pressures lower than about 2 Pa, the measured EEDF is clearly non-Maxwellian; the majority of the electrons (the bulk of the EEDF) can be still described by a Maxwellian distribution with the low temperature of about 0.12 eV, yet electrons with energies higher than about 0.8 eV can be described with a Maxwellian distribution with higher temperature of about 0.45 eV. The existence of the tail of the bi-Maxwellian EEDF leads to an increase of the electron current at the corresponding probe voltages and consequently to a shift of the floating potential of the LP to more negative potentials. In the case of Maxwellian EEDF, the floating potential corresponds to the energy at which the EEDF can be described by the low temperature, however, in the case of a bi-Maxwellian EEDF, the floating potential corresponds to energies at which the EEDF is described by the higher temperature; as indicated by the vertical dashed lines in Fig. 3.11. The electron temperature from LP data in Fig. 3.8 indicates the temperature of the bulk of the EEDF. The electron temperature obtained from the ratio $i_{2\omega}/i_{3\omega}$ by the FHP method agrees reasonably well (within 10%) with the LP data, except for pressures lower than about 2 Pa, where the electron temperature obtained from $i_{2\omega}/i_{3\omega}$ agrees well with the temperature of the tail of the bi-Maxwellian EEDF. The fact that the FHP is, at certain experimental conditions, theoretically capable of measuring the temperature of the exponential approximation of the tail of the EEPF at the electron energy corresponding to the floating potential, can be readily seen, when the electron current in Eq. 1.27 is expressed using the temperature of the exponential approximation (linear approximation in logarithmic scale) of the tail of the EEPF. For higher pressures, the electron temperature evaluated from $i_{1\omega}/i_{2\omega}$ from both the thick and thin probe is overestimated by about 50% due to the AC ion current as was discussed in 3.1. Observe, that at low pressure when the EEDF is bi-Maxwellian, the electron temperature evaluated from $i_{1\omega}/i_{2\omega}$ is even more overestimated, because, as the AC electron current decreases due to the higher temperature of the EEDF tail, the relative contribution of the AC ion current to the measured AC current

of the FHP increases.

A comparison of the ion densities determined by FHP and LP method as the pressure inside the chamber was varied is shown in Figs. 3.12,3.13. For the evaluation of the ion density from FHP data, the corresponding temperature from $i_{2\omega}/i_{3\omega}$ was used. Only the ion density estimated from $i_{1\omega}$ is shown; the ion density evaluated from $i_{2\omega}$ was systematically lower, similarly to the measurement shown in Fig. 3.5. As far as the estimation of the ion density is concerned, one has to be aware of the effect of the collision of ions with neutral particles in the probe sheath. Since I was interested mainly in a gross comparison between the FHP and the LP method, the evaluated data of ion densities were obtained without taking collisions into account. The ion density according to the Laframboise theory and ABR theory is shown in Fig. 3.10 and Fig. 3.13, respectively. It can be seen that for the larger pressures where the EEDF can be described reasonably well as Maxwellian, the ion density obtained using the FHP method is in good agreement with the data from the respective IV characteristics (LP) for both the thick and thin probe, regardless of which ion current theory was used. For the case of the bi-Maxwellian EEDF, observed at low pressures, the theory of the FHP for the ion density estimation is not applicable and the evaluated ion density should be generally underestimated and not reliable. It is clearly seen that for low pressures the thick FHP highly underestimates the ion density in comparison with that estimated from the IV characteristics. Although the thin FHP shows a good agreement with the LP data in this particular measurement even at the low pressure of 1.5 Pa with bi-Maxwellian EEDF, it should be considered rather as a coincidence and not as a reliable measurement.

It is reasonable to assume quasineutrality of the plasma $n_i = n_e$, hence, the electron density is also shown for comparison. The difference in electron density evaluated from the Langmuir probe current at plasma potential between the thick and thin probe was maximally 20 %, hence only the data from the thin probe are shown. The Debye number of the thin probe varies in the range $D_\lambda = 1 - 5$, which is around the empirical limit of $D_\lambda < 3$ for which the OML theory can be used. Nevertheless, the electron density using the OML theory, see Eq. 1.25, is in satisfactory agreement with the electron density estimated from the electron current at plasma potential, see Fig. 3.13.

There is a clear discrepancy in the ion density obtained from the thin probe and the thick probe, regardless of the collisionless ion current theory used. The plasma flow velocity in the hollow-cathode plasma jet was measured in [58, 52]. At the slightly lower argon gas throughput of 100 sccm, pressure of 3 Pa and at the distance of 4 cm from the hollow-cathode, the observed plasma flow velocity was about 600 m/s, which is comparable and even exceeds the expected ion thermal velocity of about 500 m/s (assuming $T_i \approx 450$ K, see [59, 60]). Moreover, with the decrease of the pressure inside the chamber, the flow velocity is expected to steeply increase. Consequently, the ion collection efficiency at the downstream side of the thick probe can be reduced due to the shadow effect, hence reducing the effective collection area of the thick probe. Consequently, the apparent ion density comes out smaller both in the case of the ion density evaluation from the

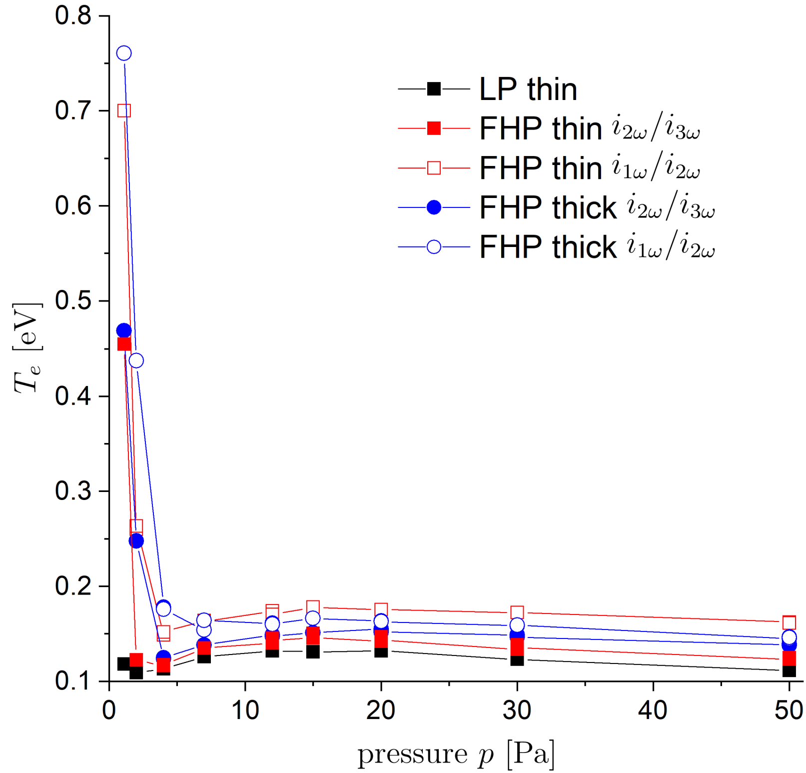

Figure 3.10: Pressure dependence of the electron temperature obtained by the FHP method in comparison with the temperature evaluated from 2nd derivative of the thin LP. The electron temperature from the 2nd derivative of the thick probe is not shown as the points mostly overlapped with that obtained from the thin probe.

FHP as well as from the IV characteristics. Another effect that should be taken into account when discussing the discrepancies in the evaluated ion densities, are the possible collisions of the ions with neutral particles in the probe sheath. For instance at 20 Pa the ratio of the sheath thickness calculated according to [61] and the ion mean free path (assuming $T_i \approx 450$ K) is about 0.7 for the thick probe whereas it is only 0.35 for the thin probe. Hence it follows, that the thick probe is expected to be more influenced by the ion collisions in the sheath than the thin probe, which could be the reason for the ion density discrepancy between the thick and thin probe for the higher pressures.

In the case of the thin probe, the ion density determined using the Laframboise theory (OML) fits very well with the electron density data, while applying the ABR theory (radial) results in underestimated ion density data even by a factor of 2. The use of the radial theory by Fernández Palop [33] to account for a possible influence of the non-negligible ratio T_i/T_e ($T_i \approx 450$ K ≈ 0.04 eV) in the ABR theory, would lead to further decrease of the estimated ion density.

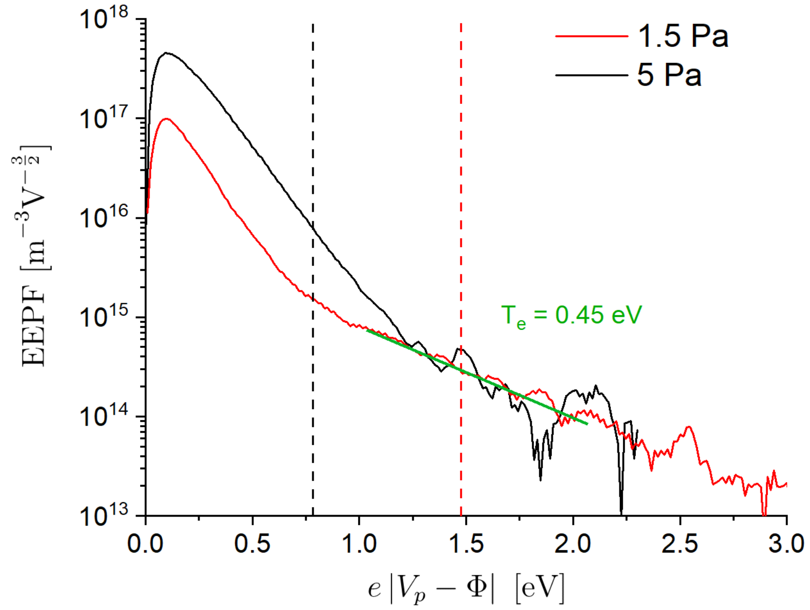

Figure 3.11: The EEPF evaluated by Eq. 1.20 from the IV characteristics of the thin probe at two different pressures 1.5 and 5 Pa. The vertical bars show the respective floating potentials of the LP probe, i.e. approximately the potential around which the AC voltage was applied in the FHP method. The green line depict the linear fit of the tail of the EEPF measured at 1.5 Pa corresponding to electron temperature of 0.45 eV

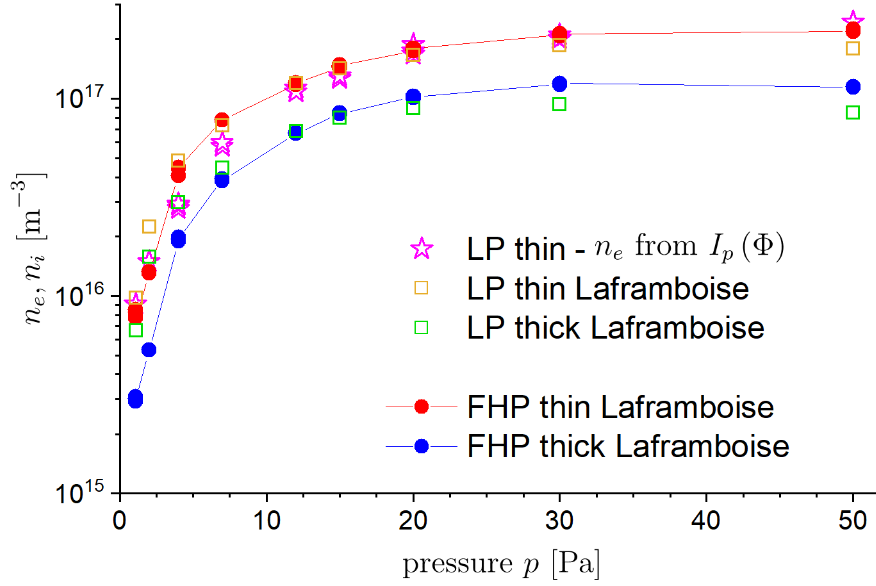

Figure 3.12: The pressure dependence of the ion density according to the Laframboise theory obtained by the FHP method from $i_{1\omega}$ in comparison with the ion density evaluated from the IV characteristics (at the working point $\Phi - 20k_BT_e/e$). The electron density n_e estimated from the LP current at plasma potential is also shown.

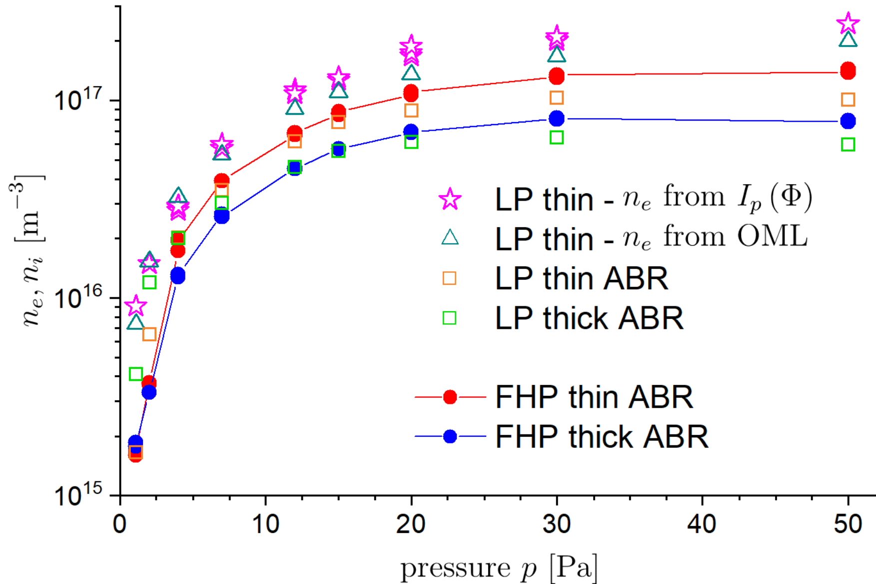

Figure 3.13: The pressure dependence of the ion density according to the ABR theory obtained by the FHP method from $i_{1\omega}$ in comparison with the ion density evaluated from the IV characteristics (at the working point $\Phi - 20k_BT_e/e$). The data of the electron density n_e estimated from the current at plasma potential of the thin LP is the same data as are shown in Fig. 3.12. Moreover, the electron density from the thin LP according to the OML theory is compared.

3.4 Measurement during deposition of Fe_2O_3

The results of measurements of electron temperature and ion density with FHP with the oxygen gas introduced into the discharge chamber are shown in Fig. 3.15 and Fig. 3.16. The data shown were measured at a fixed AC voltage amplitude of 0.25 V at various frequencies and at the discharge conditions: argon gas flow of 100 sccm, pressure 5 Pa and discharge current of 300 mA. Similar results were obtained also when using smaller AC voltage amplitude of 0.15 V. The vertical dashed lines depict the time interval, when the oxygen flow of 3 sccm was turned on and the Fe_2O_3 film was being deposited on the probes. After about 45 min of deposition, the oxygen flow was turned off and the probes were cleaned by ion bombardment in a pure argon discharge for about 5 min when biased at -100 V with respect to ground, while getting covered by sputtered iron. A rather good agreement of the the ion density obtained after probe cleaning with the value obtained before deposition indicate a satisfactory reproducibility of the measurement. The IV characteristics were also recorded during deposition; the IV characteristic of the thin probe can be seen in Fig. 3.14. It is apparent, that already after about 2 minutes of deposition the recorded IV characteristic is clearly distorted. After about 8 minutes of deposition the probe current in the ion saturation region dropped by almost one order of magnitude and the probe current in the electron saturation region dropped by about two orders of magnitude. As the thickness of the deposited iron oxide layer increases during deposition, its impedance also increases (and capacitance decreases) and the left side of the condition in Eq. 1.38 for the proper FHP operation may not be fulfilled. The results in Figs. 3.15, 3.16 clearly show, that for longer deposition times (thicker layer) a higher frequency must be utilized to satisfy the left part of the condition in Eq. 1.38 and to obtain unperturbed data. It should be noted, that for the evaluation of the ion density during measurement with oxygen by means of both the thin and thick probe for all the frequencies of the AC voltage, the unperturbed value of the electron temperature of about 0.12 eV was used (evaluated from the ratio $i_{2\omega}/i_{3\omega}$ by the thick probe at 150 kHz). Both the electron temperature and the ion density measured by the thick probe at the frequencies of about 100 kHz and higher, can be said to be unperturbed by the deposited film even after 45 min of deposition. On the other hand, e.g. the numerical value of the electron temperature obtained by means of the thin probe at the same frequency of 150 kHz at the end of the deposition is almost five times higher, and clearly influenced by the deposited thin film impedance.

This may be explained by the fact, that the left part of the condition in Eq. 1.38 is better met for the thick probe. The deposition rate of the iron oxide film has been estimated by deposition at the same conditions on a glass/FTO substrate and measuring the thickness of the film by a profilometer. Hence, it is expected, that the thickness of the deposited film on the probes was roughly 1.1 μm. Due to the much larger radius of both the probes, the capacitance of the deposited film can be estimated by the simple formula for planar capacitor, see Eq. 1.64. Therefore, the film capacitance is proportional to the area of the respective probe $C_f \propto A_p$. In order to compare the sheath impedance of the two

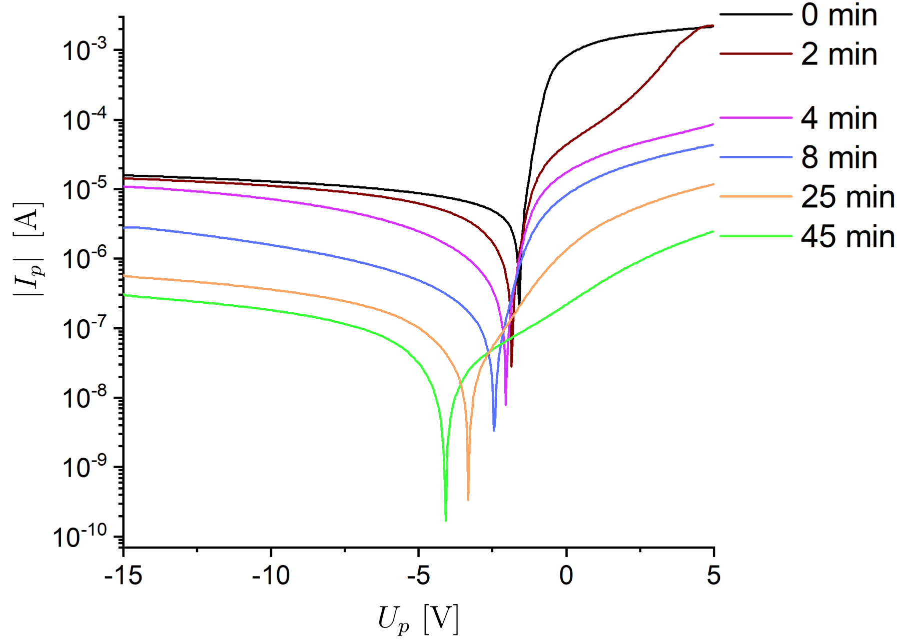

Figure 3.14: The IV characteristic of the thin probe before introducing the oxygen gas into the chamber (characteristic at 0 min) and measured IV characteristics after certain time of deposition of the iron oxide thin film.

probes, the sheath resistance multiplied by the respective probe area, $R_s A_p$, needs to be considered. This quantity is not equal for the thin and thick probe, yet the one of the thick probe is larger. From the derivative of the IV characteristics before deposition, the product of the sheath resistance and the probe area $R_S A_p$ at the floating potential was evaluated to 0.2 kΩ cm^2 for the thin probe and to 1.2 kΩcm^2 for the thick probe. These results are in consent with the sheath resistance obtained directly as $A_p V_0 / i_{1\omega}$. After the oxygen was introduced, the ion density decreased and the value $R_s A_p$ changed to 0.3 kΩcm^2 for the thin probe and to 1.5 kΩcm^2 for the thick probe. The fact, that the value $R_s A_p$ for the thick probe evaluated at the floating potential is 5 - 6 times larger than that for the thin probe can be understood by different ratios of the effective ion collection area with respect to the probe area. The lower relative effective collection area of the thick probe is caused by the relatively lower effect of the sheath expansion on the ion current and partially also by the shadowing effect and ion collisions as discussed in 3.3.

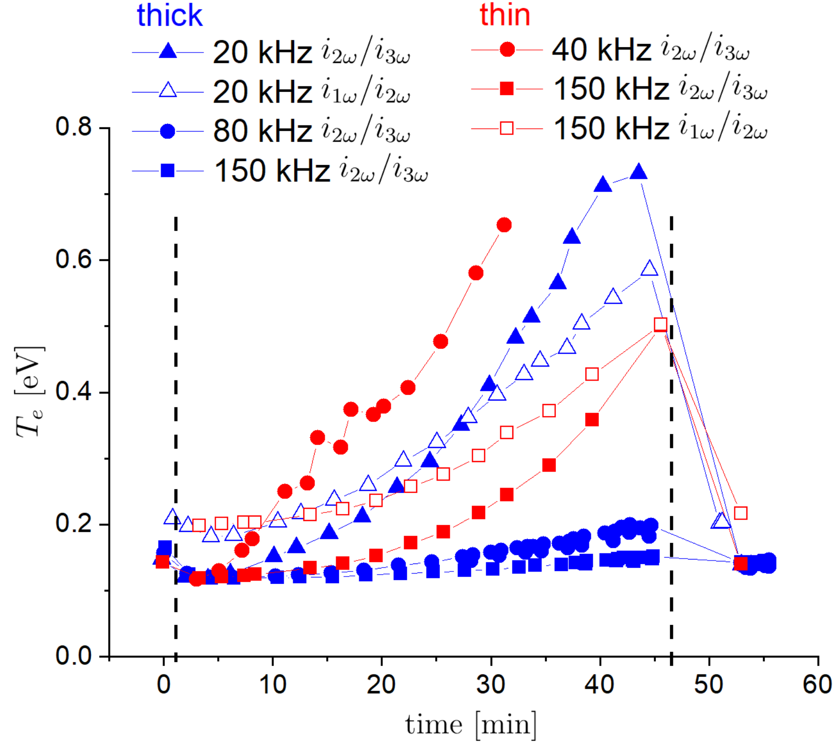

Figure 3.15: The time evolution of the electron temperature measured by FHP using different frequencies of the AC voltage during Fe_2O_3 film deposition. The vertical dashed lines depict the time interval, when the oxygen gas flow was turned on and reactive sputter deposition of Fe_2O_3 film was taking place.

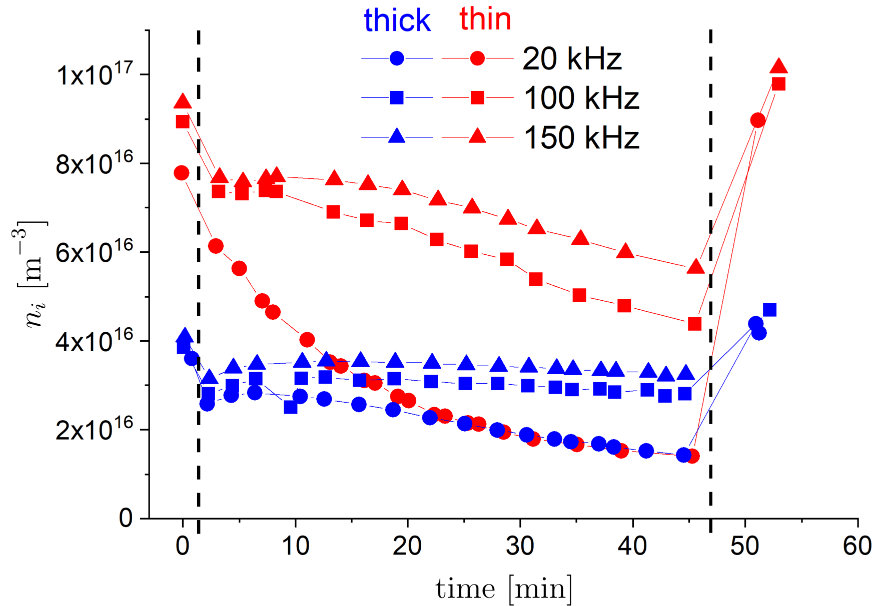

Figure 3.16: The time evolution of the ion density according to the Laframboise theory measured by FHP using different frequencies of the AC voltage during Fe_2O_3 film deposition. The vertical dashed lines depict the time interval, when the oxygen gas flow was turned on and reactive sputter deposition of Fe_2O_3 film was taking place.

4. FHP measurements in DC pulsed regime

In this chapter results obtained with the FHP probe measured in pulsed DC discharge in magnetron and hollow-cathode plasma jet are discussed. The measurements with single or double FHP were performed utilizing the PDHAM method, see 2.7. After measurements made using the FHP technique at given conditions, the probe was subsequently used also as a Langmuir probe. Because the IV characteristics of the Langmuir probe were very noisy in the ion saturation region, they could not be used for evaluation of the ion density. Therefore, the FHP ion density data are compared with the electron density obtained from the LP probe current at plasma potential. The IV characteristics were processed manually, therefore only a few of them selected at particular instants during and after the discharge active pulse were processed. During some measurements the recorded IV characteristic could not be reliably processed typically at the beginning of the active pulsed, hence the data is missing. The first harmonic current $i_{1\omega}$ from FHP was used to evaluate the ion density according to the Laframboise theory.

4.1 Single FHP in magnetron discharge

The results presented below have been measured in non-reactive magnetron discharge with Ti cathode with zero oxygen flow at a constant pulsing frequency of 100 Hz with an active pulse length of 1 ms, i.e. with a duty cycle of 10 %. The average discharge current was in the range $I_{AV} = 230 - 250$ mA. Argon flow was held constant at 30 sccm (the hollow-cathode shutter was closed). Results of measurements at three different pressures (1 Pa, 6 Pa, 15 Pa) are shown and discussed. A tungsten cylindrical probe of 50 μm in diameter and length of 11.7 mm was used for the measurements. An AC voltage of amplitude of 0.4 V and frequency of 20 kHz was applied during FHP measurements. The probe was positioned about 8 cm from the magnetron target approximately at the magnetron axis. The magnitude of the magnetic field was measured by means of a Hall probe A1302KUA-T (13 mV/mT) and at the position of the probe the magnetic field was found negligible (< 1 mT).

First, the measurement performed at pressure of 1 Pa is discussed in more detail. In Fig. 4.1a the measured current of the single FHP is shown when an AC voltage with a given phase shift was applied to the probe. It can be clearly seen that beside the AC current, a transient current i_t was detected. In Fig. 4.1b several one period waveforms in the phase domain are shown, which were evaluated as described in 2.7. Measurements with two different DC blocking capacitors of 50 nF and 5 nF are compared in Fig. 4.2. For understanding of the results it is necessary to see also the temporal evolution of the mean potential $\bar{V}$ and the floating potential V_{fl}, see Fig. 4.2c. The probe potential during FHP measurement was monitored by an ordinary oscilloscope probe (≈ 15 pF). The mean probe potential $\bar{V}$ was evaluated similarly to the transient current, i.e. as the

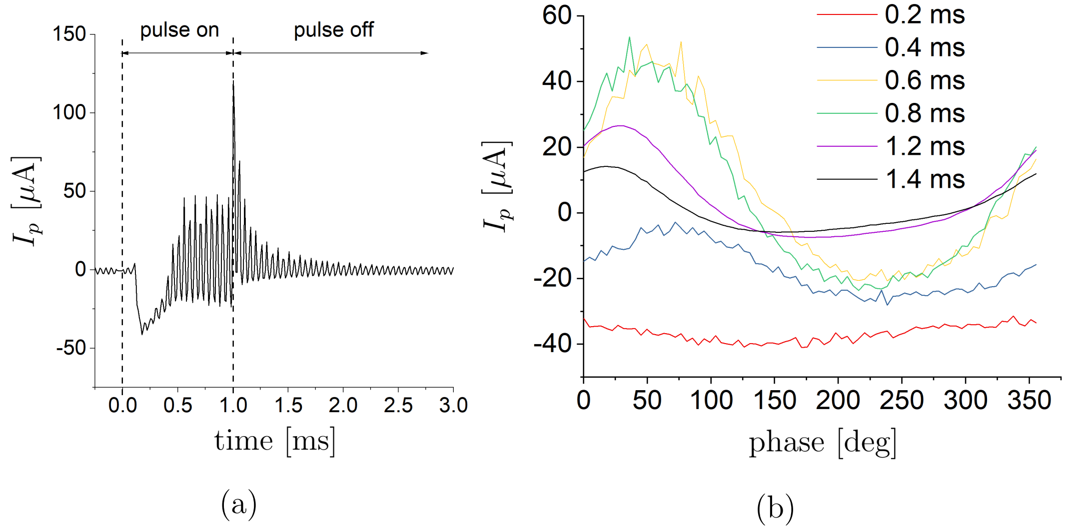

Figure 4.1: (a) Measured FHP current during and after active pulse for a given phase delay of 13.5°. The parasitic current in the shown waveform has been not subtracted and its magnitude can be observed from the measured signal before the start of the pulse. (b) The one period FHP current waveforms at different times during and after the active pulse reconstructed in the phase domain. These data are taken from the same measurement as shown in Fig. 4.2 using the DC blocking capacitor of 5 nF.

mean voltage of the voltage waveform in the phase domain. During measurement of the floating potential V_{fl}, the FHP measuring circuit was disconnected from the probe. The floating potential was usually recorded before and after the FHP measurement and after the LP measurement to be sure that the discharge did not change. At this particular condition, a delay of about 120 μs between the time of application of the discharge voltage and the time of the plasma ignition was observed. This time delay is depicted in Fig. 4.2a,b,c,d by a gray rectangle. This time delay needed to initiate the plasma by secondary electrons to generate Townsend ionization avalanche [62] was seen to decrease, when the argon pressure or applied discharge voltage was increased. After the delay, the floating potential steeply increased. Because the capacitance of the FHP is given predominantly by the relatively large DC blocking capacitor, the probe was not able to follow the steep increase of the floating potential. Therefore, the FHP mean potential $\bar{V}$ was left far in the ion saturation region, several $k_B T_e/e$ more negative than the floating potential, where, however, only small ion current flows to the probe which makes charging of the DC blocking capacitor very slow. Clearly, the FHP using the lower capacitor of 5 nF was able to better follow the temporal evolution of the floating potential. When the probe's mean potential $\bar{V}$ is not equal to the floating potential V_{fl} (for simplicity neglecting the self-biasing effect), a transient current flows through the probe as can be seen in Fig. 4.2d. The measured transient currents are both qualitatively and quantitatively in agreement with the observed temporal evolution of the potentials. Just after the end of the active pulse a steep decrease of the floating potential occurred. The temporal evolution

of the floating potential is supported by the evaluated evolution of the plasma potential from LP. At the end of the pulse during the decrease of the floating potential, the FHP using DC blocking capacitor of 5 nF was able to react faster compared to the transient at the beginning of the pulse. This can be explained easily by the fact, that the mean probe potential $\bar{V}$ was left in the transition region, where the higher electron current can charge the DC blocking capacitor faster.

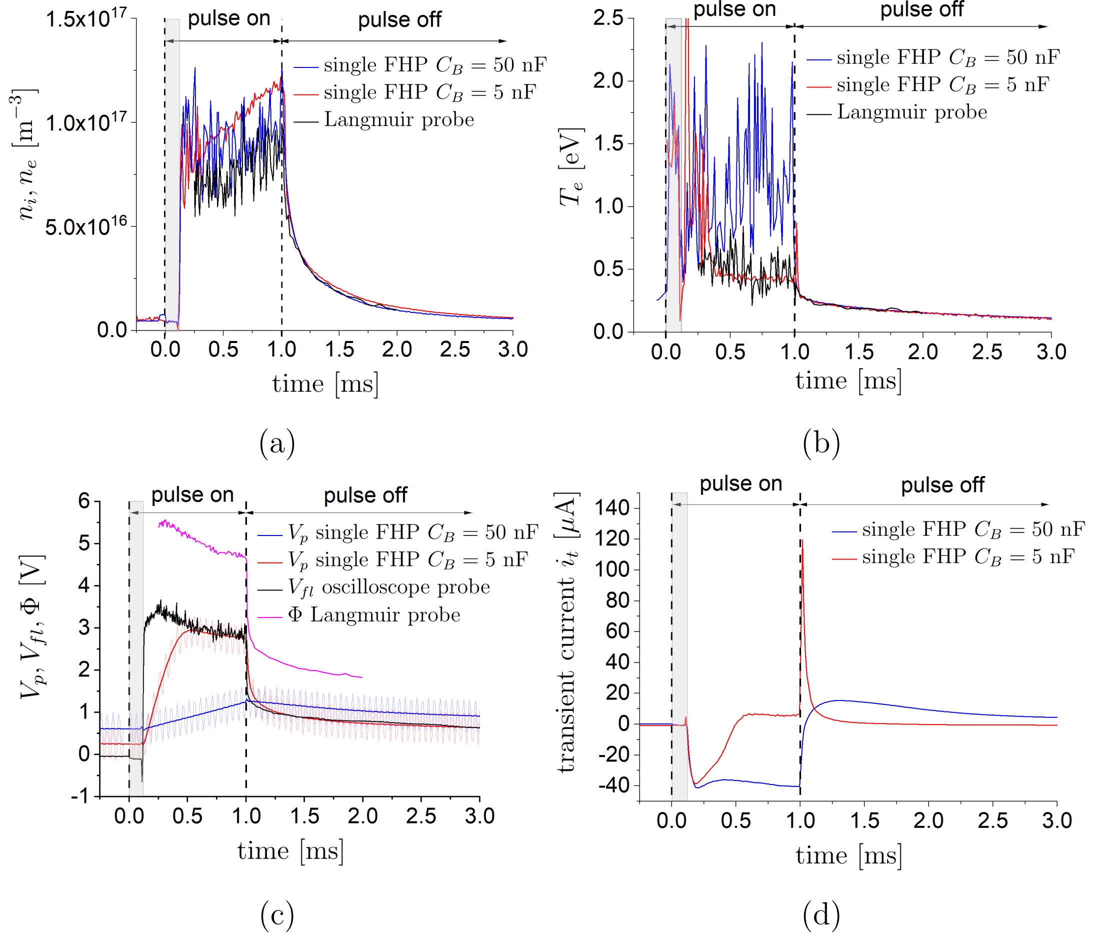

Figure 4.2: Time evolution of several plasma and probe parameters during and after discharge pulse. Two different dc blocking capacitors of 5 nF and 50 nF were used for FHP measurement. (a) Ion density measured by FHP and electron density measured by Langmuir probe obtained from the probe current at the plasma potential (b) Electron temperature from FHP determined from the ratio $i_{1\omega}/i_{2\omega}$, electron temperature by Langmuir probe determined from the slope of 2nd derivative of IV characteristics. (c) V_p - the FHP potential during measurement and its mean value $\bar{V}$, V_{fl} - the floating potential, Φ – the plasma potential. (d) The transient current i_t flowing through the FHP probe. A frequency of 20 kHz and AC voltage amplitude of 0.4 V was used for FHP measurement. Discharge conditions: pressure $p = 1$ Pa, average discharge current $I_{AV} = 250$ mA, discharge voltage $U_D = 400$ V, average discharge power $P_{AV} = 100$ W, pulsing frequency $f_p = 100$ Hz, duty cycle 10 %.

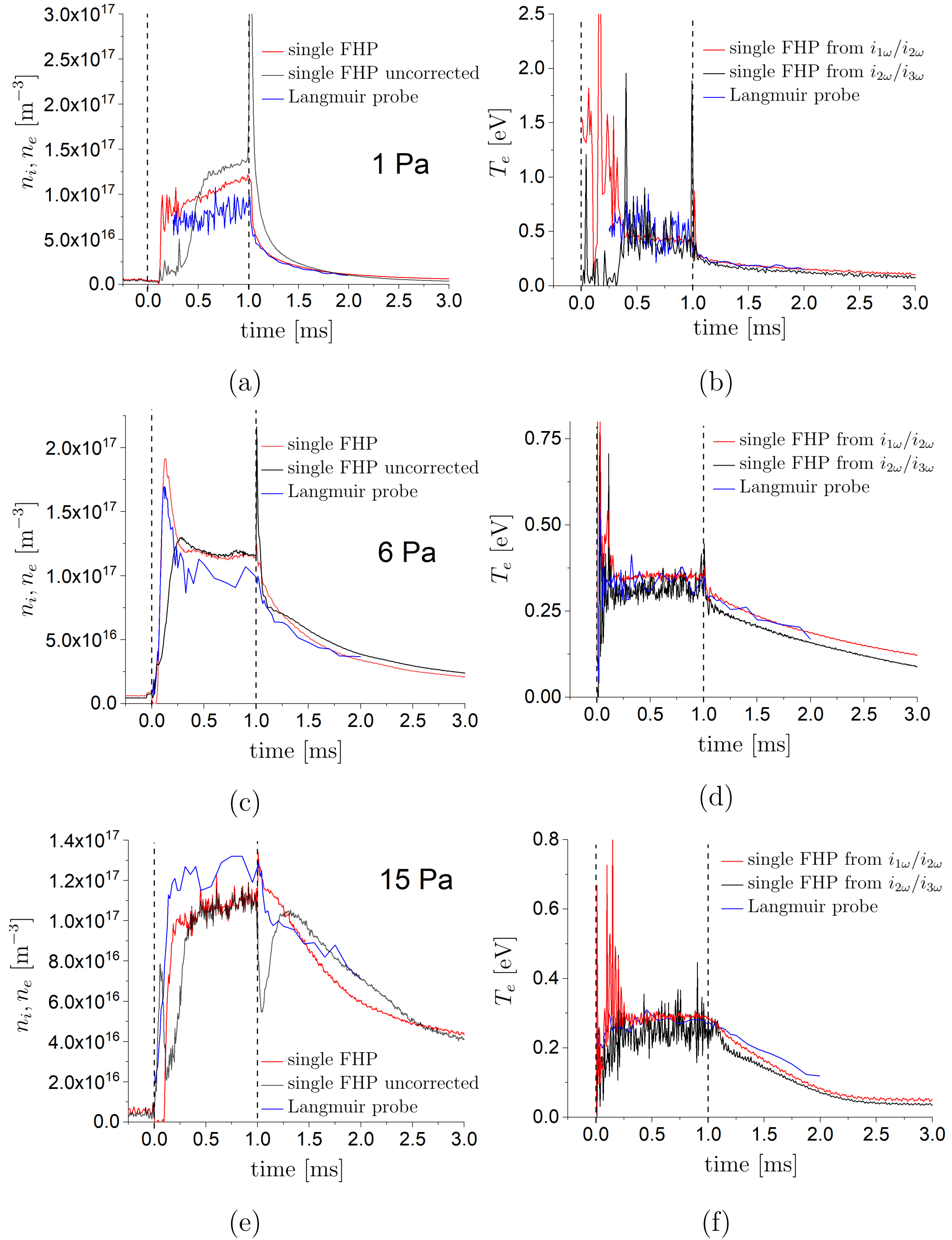

Figure 4.3: The temporal evolution of the ion and electron density (a),(c),(e) and of the electron temperature (b),(d),(f) for three different discharge conditions: (a),(b) $p = 1$ Pa, $I_{AV} = 250$ mA, $U_D = 400$ V; (c),(d) $p = 6$ Pa, $I_{AV} = 230$ mA, $U_D = 290$ V; (e),(f) $p = 15$ Pa, $I_{AV} = 215$ mA, $U_D = 250$ V. The FHP uncorrected ion density stands for the ion density that was obtained from ion current evaluated by means of the formula Eq. 1.34, which does not account for the transient current i_t. All the results shown were made using the DC blocking capacitor of 5 nF. The measurement at 1 Pa is the measurement shown already in Fig. 4.2. All the three measurements were performed in magnetron discharge in non-reactive regime with zero flow of oxygen.

The electron temperature obtained with the 50 nF capacitor is burdened with scatter and its mean value is overestimated for the duration of the active pulse when compared to that obtained from the LP data, see Fig. 4.2b. It has to be noted that during the first 120 μs after start of the voltage, the FHP temperature data for both the capacitors shown are not valid; they represent just noise. When the 5 nF capacitor was used, the temperature was overestimated only at the beginning of the voltage pulse to about 400 μs, approximately until the mean FHP potential reached the floating potential. It is clearly seen, that the FHP measured noisy overestimated unreliable electron temperature only when the FHP mean potential was much lower than the floating potential. Consequently, the FHP was operating far in the ion saturation region, where the electron current and the corresponding harmonic currents are much smaller and more susceptible to noise. Furthermore, the tail of the EEDF may not be Maxwellian anymore. Last but not least, the dependence of the ion current on voltage may also play a role, as the ion current - in this part of the IV characteristic - is higher than the electron current.

The ion densities obtained from FHP is only slightly overestimated when compared to the LP electron density data, see Fig. 4.2a. It can be seen that although the probe with the 50 nF DC blocking capacitor was absolutely not able to follow the changes of the floating potential during the active pulse, the evaluated ion density obtained with 50 nF capacitor is very roughly similar to the results obtained by FHP with 5 nF DC blocking capacitor and by LP. However, when using FHP with 5 nF DC blocking capacitor better results were obtained, which are less noisy and a distinct linear increase of the ion density during the active part of the pulse is clearly recognizable. The slope of the ion density increase during the active pulse measured using 5 nF DC blocking capacitor, coincides with the increase of the electron density measured by LP. After the active pulse the LP data (both the electron temperature and density) are in perfect agreement with the FHP data measured using both the DC blocking capacitors.

Measurements at three different pressures 1 Pa, 6 Pa and 15 Pa are compared in Fig. 4.3. Only the measurements with a 5 nF capacitor are shown. Beside the ion density evaluated from the ion current obtained using the Eq. 1.41, I have shown in the graphs also the ion density evaluated from the ion current obtained by means of Eq. 1.34 which does not take into account the transient current i_t. Hence, one can easily distinguish between the contributions of the AC current $i_{1\omega}$ and the transient current i_t to the evaluation of the ion density. The obtained ion density is in reasonably good agreement with the electron density obtained from LP. The delay observed during measurement at 1 Pa was no longer observed at higher pressures. A distinct peak in the measured ion and electron densities at the beginning of the active pulse was observed during measurement at the pressure of 6 Pa. This indicates a very good reliability of the FHP measurement at these discharge conditions. Notice, that when the transient current is not accounted for in the evaluation, the peak in the ion density is not observed. Beside the electron temperature evaluated from the ratio $i_{1\omega}/i_{2\omega}$, it was possible to reliably evaluate the electron temperature also from the ratio $i_{2\omega}/i_{3\omega}$, except from the

beginning of the pulse measured at 1 Pa, see Fig. 4.3b,d,f. Evidently, during the active pulse the electron temperature evaluated from the ratio $i_{2\omega}/i_{3\omega}$ is seen to be more burdened by noise than that evaluated from the ratio $i_{1\omega}/i_{2\omega}$.

Two FHP measurements in magnetron discharge in non-reactive regime and in reactive regime with 3 sccm flow of oxygen are compared in Fig. 4.4. A comparison with LP in the reactive regime was not possible as the IV characteristics were highly distorted. As can be seen in Fig. 4.4b, the evaluated electron temperature is very noisy and very likely overestimated during the active pulse in reactive regime, although from the measurement of the floating potential and transient currents it follows, that the probe operated near the floating potential for most part of the active pulse in the reactive regime. It is very likely, that the EEDF during measurement in the reactive regime was not Maxwellian and FHP operated in the higher energetic part of the EEDF with higher electron temperature. The noise on the electron temperature data is given mainly due to the low noisy signal from the second harmonic current $i_{2\omega}$. In the afterglow after Maxwellization of the EEDF, the evaluated electron temperature and ion density can be considered reliable even during measurement in the reactive regime. In the reactive regime after the end of the active pulse, the evaluated electron temperature steeply dropped to values much lower than that observed in non-reactive regime. It can be said that the ion density measured during the active pulse in reactive regime is most likely underestimated, yet still of reasonable magnitude, when compared to the ion density measured in the afterglow. No significant changes in the measured values by means of the FHP were observed during more than 20 minutes of measurement in the reactive regime.

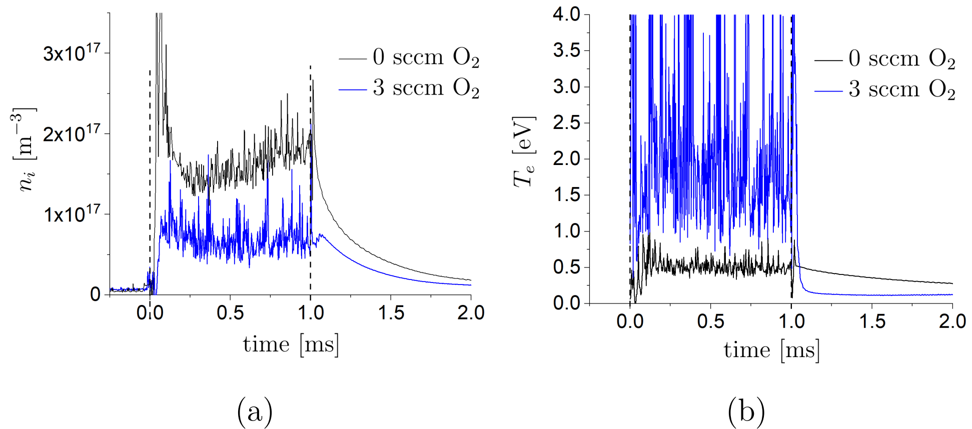

Figure 4.4: Temporal evolution of the ion density (a) and the electron temperature (from $i_{1\omega}/i_{2\omega}$) (b) as measured by the single FHP method during non-reactive regime (0 sccm flow of O_2) and reactive regime (3 sccm flow of O_2). Both the measurements were performed in magnetron discharge at pressure 2 Pa, average discharge current 400 mA, pulsing frequency 100 Hz, duty cycle 10 % and argon flow 30 sccm. The discharge voltage for non-reactive regime was 395 V and in reactive regime 530 V. Frequency 60 kHz, AC voltage amplitude 0.4 V and DC blocking capacitor 5 nF was used for the FHP measurements.

4.2 Double FHP measurements

It was shown in 4.1 that the single FHP is not capable to reliably measure the electron temperature when it operates in the ion saturation region due to the fact, that the probe might not be able to follow the changes of the floating potential fast enough. As in the double probe technique no DC blocking capacitor connected to ground is needed, the capacitance of the probe system to the ground can be much lower and therefore it should be able to better follow the transients of the floating potential. Two tungsten probes of diameter of 50 μm and length of 12 mm were positioned near to each other at the magnetron axis in a distance of about 8 cm from the magnetron Ti target. For measurement with the single FHP and LP methods, one of the probe of the double probe was used. The capacitance to ground of the measuring circuit, see Fig. 2.6, together with the connecting wires was roughly about 100 pF. This capacitance must get charged by the current flowing to the two probes during transients of the floating potential.

Fig. 4.5 shows results from a comparative measurement with double FHP, single FHP and LP. During double FHP measurement both the probes of the doule probe were capable to follow perfectly the temporal changes of the floating potential. It can be seen, that the electron temperature obtained with double FHP is in rather good agreement with that obtained from LP even in the first 500 μs from the beginning of the active pulse. On the other hand, the single FHP was operating far in the ion saturation region in the first 500 μs from beginning of the pulse, which resulted in noisy and overestimated electron temperature estimated during that time interval. On the other hand even when the evaluated temperature by the single FHP was overestimated, the corresponding ion density is in very good accord with the ion density obtained by means of the double FHP. Although the evaluated ion densities from both the single FHP and double FHP are overestimated when compared to the electron density obtained by LP, the course of the temporal evolution of the estimated ion density during and after the pulse is in accord with the temporal evolution of the measured electron density.

Both the single and double FHP were tested also in DC pulsed discharge in hollow-cathode plasma jet system. A higher repetition frequency of 1 kHz was chosen for better stability of the discharge pulses. The probes were positioned at the axis of the plasma-jet in a distance of 8 cm. As can be seen in Fig. 4.6c the floating potential steadily decreased during the pulse and right after the pulse the floating potential increased rapidly almost to the value before the pulse. This observation is in perfect agreement with the temporal evolution of the plasma potential. The double FHP was seen to be capable to follow the rapid increase of floating potential and only small transient current was detected in comparison to the transient current detected during measurement with single FHP, see Fig. 4.6d. However, it must be noted, that only fraction of the transient current flowing through the double FHP to ground is measured due to the fact, that the sensing resistor is connected outside the vacuum chamber. Perfect agreement of the electron temperature obtained by double FHP and LP methods was observed,

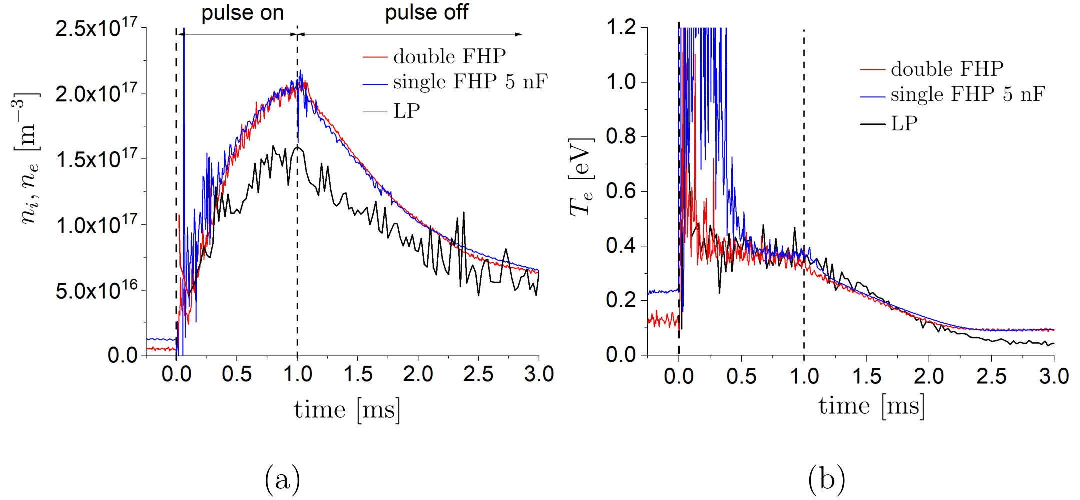

(a) (b)

Figure 4.5: Temporal evolution of the ion and electron density (a) and the electron temperature (from $i_{1\omega}/i_{2\omega}$) (b) as measured by the single FHP, double FHP and LP method. A frequency of 20 kHz and AC voltage amplitude of 0.4 V and 0.45 V was used for single FHP and double FHP measurement, respectively. The measurements were performed in non-reactive magnetron discharge at pressure 10 Pa, average discharge current 300 mA, discharge voltage 285 V, pulsing frequency 100 Hz and duty cycle 10%.

see Fig. 4.6b both during and after the pulse. The single FHP method did not measure very reliable data in the hollow-cathode plasma jet system even at different discharge conditions, which is illustrated on the evaluated evolution of the ion density in Fig. 4.6b. The ion density obtained by means of the double FHP and LP after the pulse are in reasonable agreement. A maximum of the ion density was observed after roughly 300 μs from the end of the pulse. The delay of the peak in the ion density is given by the velocity of the flowing argon gas from the jet and the distance of the probe from the plasma-jet. The average velocity of the flowing plasma to the probe from these data can be estimated to be roughly 200 m/s, which is in accordance with the velocities measured at this system earlier at similar conditions, see [58, 52]. In the active pulse the double FHP measured evidently non-reliable decrease of the ion density which is not in accord with the LP data measuring almost constant ion density.

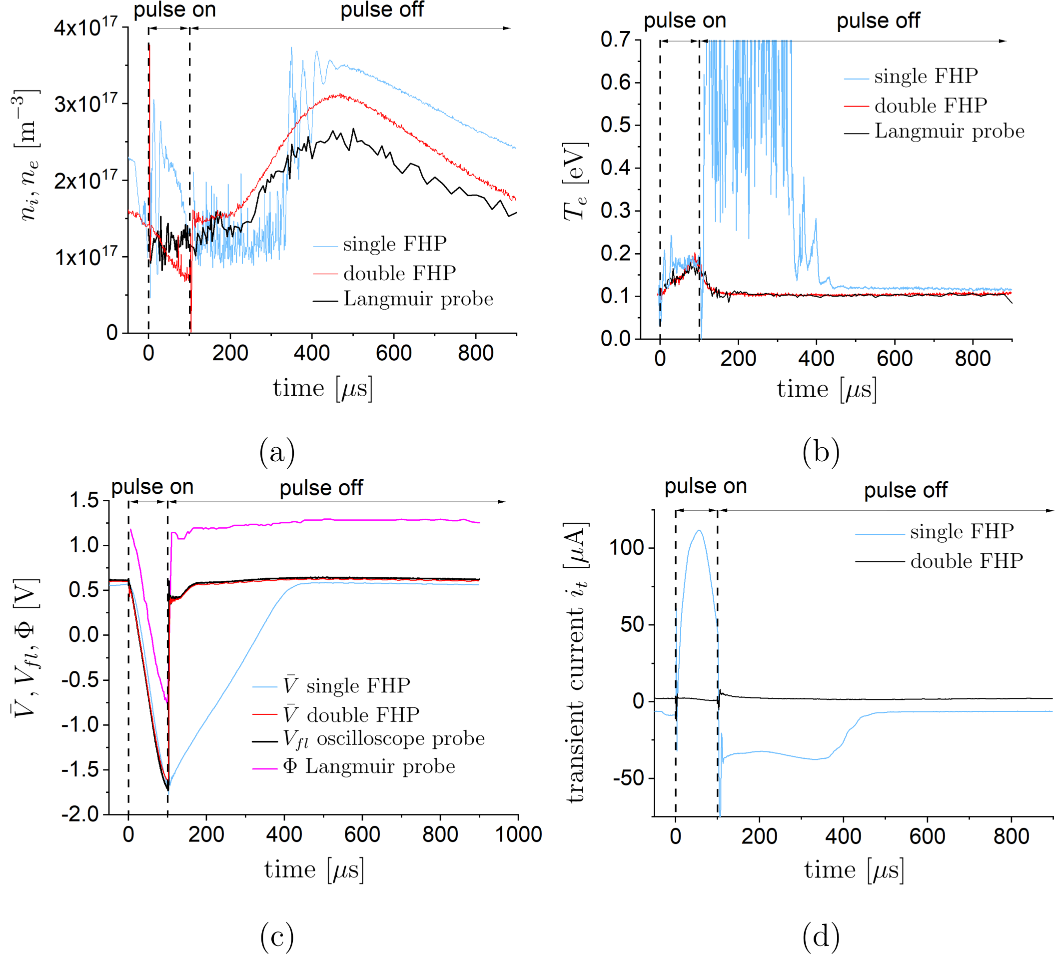

Figure 4.6: Time evolution of several plasma and probe parameters during and after discharge pulse as measured by the single FHP and double FHP. (a) Ion density measured by FHP and electron density measured by Langmuir probe. (b) Electron temperature from FHP determined from the ratio $i_{1\omega}/i_{2\omega}$, electron temperature by Langmuir probe. (c) $\bar{V}$ - the mean FHP potential during measurement, V_{fl} - the floating potential, Φ – the plasma potential. (d) The measured transient current i_t flowing through the single and double FHP probe. A frequency of 30 kHz and AC voltage amplitude of 0.3 V was used for single FHP measurement and 0.6 V for double FHP measurement. A DC blocking capacitor of 5 nF was used for the single FHP measurement. Discharge conditions: pressure $p = 3$ Pa, average discharge current $I_{AV} = 320$ mA, average discharge power $P_{AV} = 100$ W, pulsing frequency $f_p = 1$ kHz, duty cycle 10 %.

5. In-situ impedance spectroscopy

Results of in-situ impedance measurements performed during depositions of three different thin films are presented and discussed in this chapter. For clarity, the deposited films are summarized in Tab. 5.1. The first two films (#1) Fe_2O_3 and (#2) TiO_2 were deposited by the hollow-cathode plasma jet system and the third film (#3) TiO_2 by the planar magnetron. The following conditions were set up equally for all three depositions: argon flow 120 sccm, oxygen flow 3 sccm, pressure 4.5 Pa and discharge current 300 mA. The discharge was operated in DC continuously driven regime for all three depositions. During deposition with the magnetron system, the plasma jet shutter was closed in the vicinity of the plasma jet nozzle exit, see Fig 2.2, so that the flowing argon gas from the plasma jet did not influence the deposition by the magnetron system.

In order to assess, if the applied voltage amplitude was small enough ($V_0 \ll T_e$) to use the linearized model of the sheath impedance, the electron temperature shown in Tab. 5.1 has been determined by the FHP method applied directly to the recorded current waveforms from the impedance spectroscopy measurement. The obtained electron temperature during deposition of (#1) and (#2) films by means of the plasma-jet system are in agreement with electron temperatures observed earlier, see chapter 3. The data evaluated by means of the FHP method together with the previous results also indicate, that in the case of (#2) film the probe operated within the Maxwellian part of the EEDF, however, during the deposition of (#1) film, it operated within the higher-energetic tail of the bi-Maxwellian EEDF. It was not possible to obtain reliably the electron temperature during magnetron deposition (#3) from the data using the FHP method, since the measurement with larger AC voltage amplitude V_0 would be probably needed. However, it was evident from the data that the electron temperature (of the tail of the EEDF) was larger than 0.6 eV.

#	film	deposition method	deposition rate	thickness	substrate distance	T_e
1	Fe_2O_3	plasma-jet	32 nm/min	3.2 μm	7 cm	0.3 eV
2	TiO_2	plasma-jet	21 nm/min	1.5 μm	7 cm	0.15 eV
3	TiO_2	magnetron	2.7 nm/min	330 nm	6 cm	$>$ 0.6 eV

Table 5.1: Table summarizing the experimental conditions during deposition the different films by means of the hollow cathode plasma-jet or the planar magnetron system.

5.1 Impedance spectra

The data presented in Fig. 5.1 and Fig. 5.2 show the temporal evolution of the impedance spectra recorded during deposition of the Fe_2O_3 film (#1). Note,

that the shown impedance data have been corrected for the influence of the DC blocking capacitor and also the contribution of the parasitic capacitance has been subtracted, see Eq. 2.5.

At first glance, the Nyquist plot of the measured impedance spectra reveals similar traits when compared with the Nyquist plot of the simple model shown in Fig 1.9a. The apparent arc at high frequencies corresponds to the plasma sheath impedance and it is evident, that it remained almost constant during the deposition, as can be seen at high frequencies also from the Bode plot in Fig 5.2. On the other hand, the arc at lower frequencies was not distinguishable until about 4 minutes of deposition and then it gradually increased. These results indicate that the low-frequency part of the measured impedance spectra corresponds to the impedance of the growing thin film. As the film grows and its impedance increases, the phase of the impedance decreases at lower frequencies as can be seen from the Bode plot of the phase φ in Fig. 5.2. A plateau, where the absolute value of the impedance is almost constant can be clearly seen even after 74 minutes of deposition. Notice, in Fig. 5.1, that the arcs corresponding to the thin film impedance at 6 and 8 minutes of deposition are distinctly distorted at the low frequencies of few Hz. This is caused by the fact, that recording of one spectrum (in the direction from 1 MHz to 1 Hz) took approximately 1 min during which the film grew.

During the deposition of the TiO_2 (#2) and TiO_2 (#3) films, qualitatively similar spectra to that obtained during deposition of Fe_2O_3 (#1) were obtained. The impedance spectra of TiO_2 (#3) are shown in Fig. 5.3. The spectra obtained during deposition of TiO_2 (#2) are not shown, as they were quantitatively similar to the Fe_2O_3 (#1) spectra.

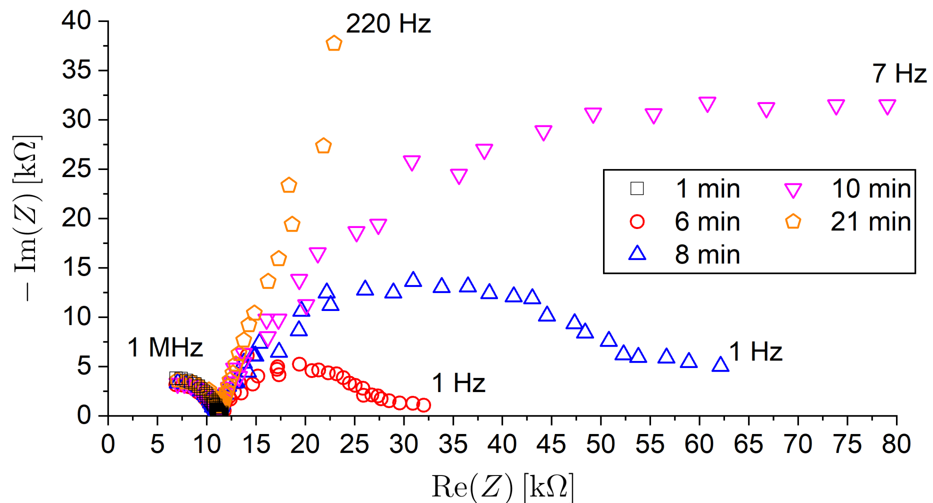

Figure 5.1: Nyquist plot of the impedance spectra during deposition of Fe_2O_3 (#1) film. To make the plot easier to see, only the spectra from the first 21 minutes of deposition are shown.

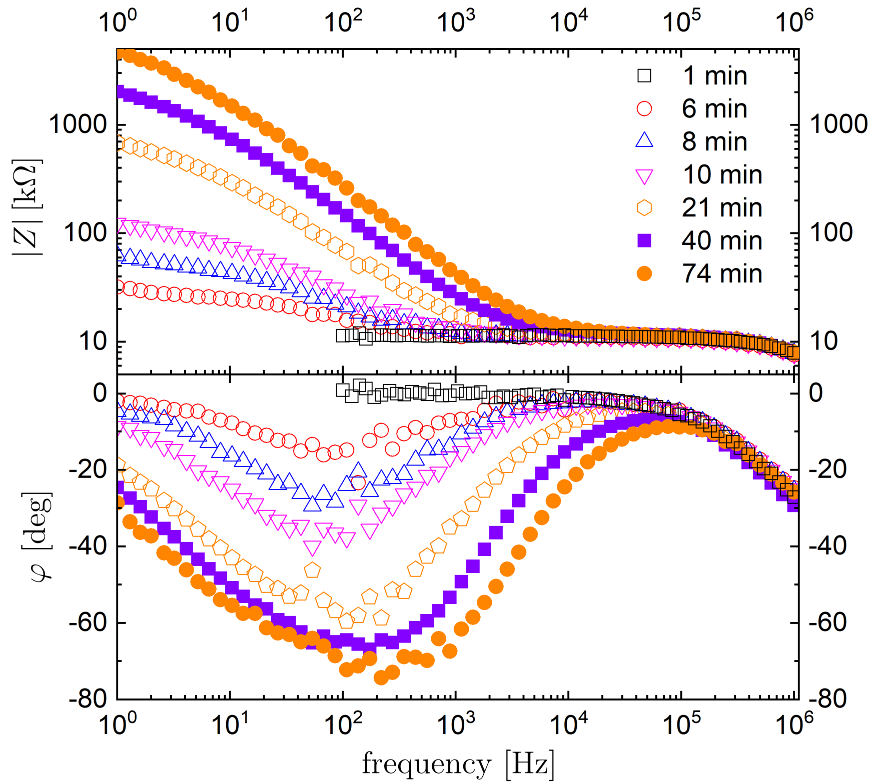

Figure 5.2: Bode plot of the impedance spectra measured during deposition of Fe_2O_3 (#1) film.

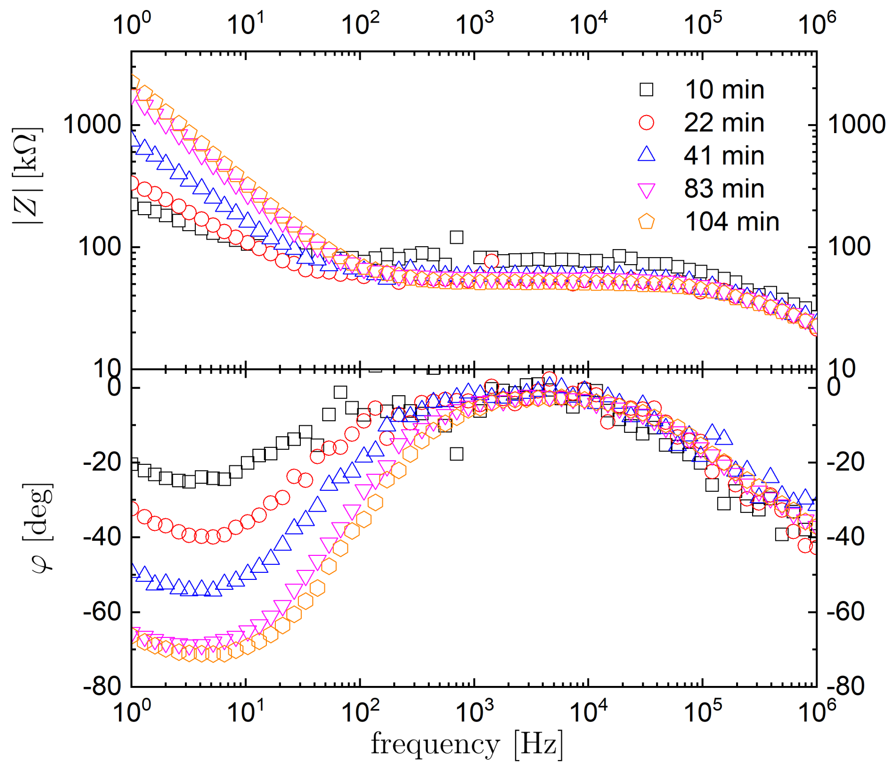

Figure 5.3: Bode plot of the impedance spectra measured during deposition of TiO_2 (#3) film.

5.2 Sheath impedance spectra

In order to evaluate the sheath resistance R_s and sheath capacitance C_s, the impedance spectra were fitted in the complex plane (real and imaginary part) in the high-frequency part of the spectra, where the impedance of the deposited film could be neglected. I decided so also from the fact, that this part of the spectra did not significantly change during deposition. However, it is evident from the data shown in Fig. 5.5 and Fig. 5.6, that the simple model of a parallel combination of an ideal capacitor and ideal resistor did not fit the measured data well and that it does not fit even into the error bars. The error bars were evaluated assuming the errors of the measurement of Z_m described in 2.8. Note, that it can be expected that the measuring circuit is able to measure with better precision at these conditions than depicted by the error bars, as follows from the measurements performed on discrete components of comparable values of R and C, see Fig. 2.10. The spectra of the admittance $Y = 1/Z$ of the same data are shown in Fig. 5.7 and Fig. 5.8. The real part of the sheath admittance $\mathrm{Re}\,(Y) = 1/R_s$ corresponds to $1/R_s$. The imaginary part of the sheath admittance $\mathrm{Im}\,(1/Z_s) = i\omega C_s$ corresponds to the sheath capacitance $i\omega C_s$. For frequencies larger than roughly 100 kHz, a decrease of the corresponding capacitance C_s with increasing frequency was observed. A decrease of the sheath capacitance with increasing frequency in this frequency range (100 kHz - 1 MHz) was observed also in [63]. It is apparent from Fig. 5.7 and Fig. 5.8 that the real part of the sheath admittance corresponding to $1/R_f$ increases with increasing frequency. Hence, the sheath resistance decreases for frequencies larger than roughly 100 kHz. In [63] it is suggested, that such effects might be caused by the non-linearity of the sheath. Due to the sheath non-linearity, the capacitive current can have a component that is in phase with the probe voltage and hence contributes to the evaluated conduction current. However, I did not observe any significant changes in the sheath impedance (admittance) spectra for different voltage amplitudes V_0 as soon as the voltage amplitude was lower than the corresponding electron temperature $V_0 < T_e$, see Tab. 5.1. This observation is illustrated in Fig. 5.4 for deposition (#1). For AC voltage amplitudes V_0 larger than the electron temperature, it was clearly observed, that the evaluated sheath resistance R_s increased with increasing the applied voltage V_0. That is in accord with the formula Eq. 1.34 applied to the first harmonic current $i_{1\omega}$.

It should be noted, that the electron/ion density during the measurements was in the order of 10^{16} m^{-3}, therefore the ion plasma frequency $\omega_i/(2\pi)$ was certainly higher than 3 MHz.

Another possibility, that might cause the decreasing of R_s with frequency, is the effect of stochastic heating [63]. This effect is represented by a resistor in series with the sheath capacitor [63], see the second model schema in Fig. 5.5. This model is in better agreement with the data than the simple one.

Nonetheless, the best correspondence of the observed data for all three depositions has been achieved with the third model, using the simple model with a CPE (constant phase element) instead of an ideal capacitor, see the third model schema in Fig. 5.5. The CPE element is well known and commonly used in the

field of impedance spectroscopy of materials, for example in a model for non-Debye dielectrics [64, 65]. "For many continuous media endowed with properties of conduction and electrical storage mixed in common volume, a phasance type of behavior will be observed", see [64], consequently the CPE element is found to describe impedance spectra of non-homogeneous media with various resistance and capacitance distributions in space. The impedance function of the CPE element is:

$$Z_{CPE} = Q^{-1}\left(i\omega\right)^{-n}, \tag{5.1}$$

where Q is real number and the parameter n ranges from 0 to 1. Note, that for $n = 1$ the CPE describes an ideal capacitor with Q corresponding to its capacitance, while for n=0 i represents an ideal resistor. A characteristic capacitance of the parallel combination of CPE with a resistor R can be determined as [66, 65]:

$$C = \left(QR^{1-n}\right)^{1/n} \tag{5.2}$$

The admittance of the CPE element depicted in the Nyquist plot is generally a straight line with an angle of $n \times 90°$ (relative to the positive real axis).

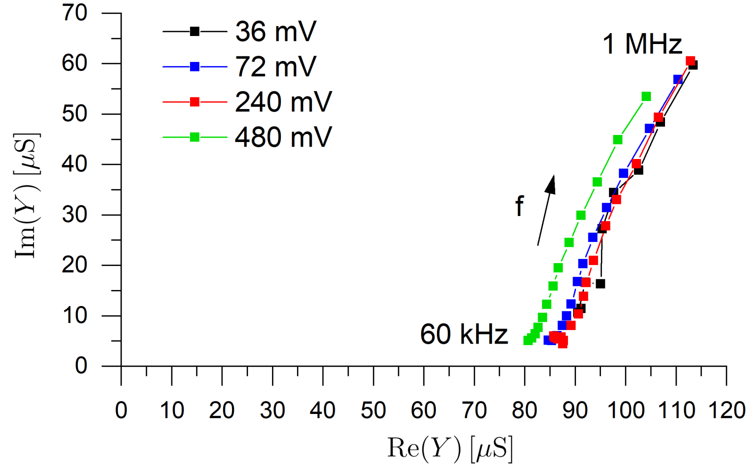

Figure 5.4: Nyquist plot of the admittance $Y = 1/Z$ spectra measured between 35 - 40 minute of deposition of Fe_2O_3 film (#1) for different AC voltage amplitudes V_0 applied. The electron temperature was evaluated by the FHP method to be 0.3 eV, see Tab. 5.1.

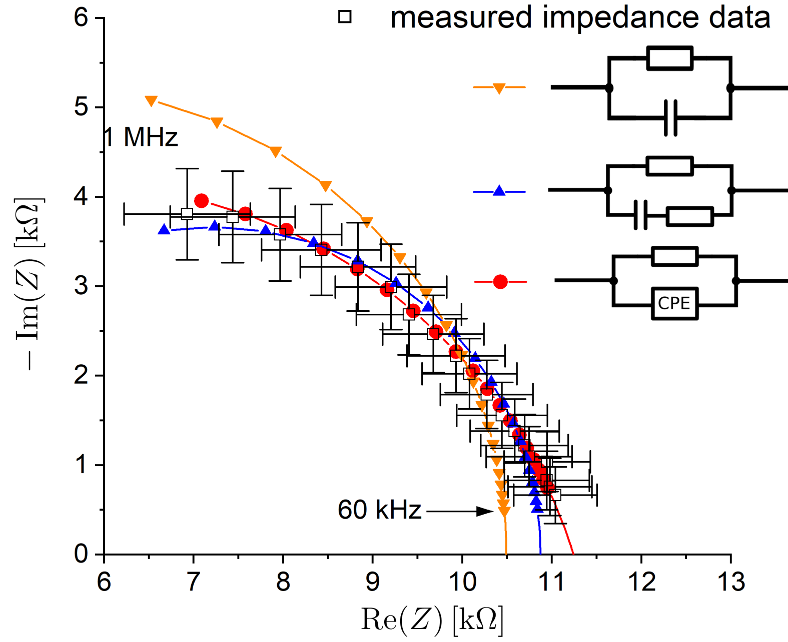

Figure 5.5: Nyquist plot of the high frequency part of the impedance spectrum after 1 minute of deposition of Fe_2O_3 film (#1) and fits of three different models evaluated in the range 60 kHz – 1 MHz. The points of the measured data and points at the fitted curves correspond to the same frequencies. The fitted parameters of the third (red) model are $R_s \approx 11.2$ kΩ, $n \approx 0.8$, $C_s \approx 9$ pF (according to Eq. 5.2).

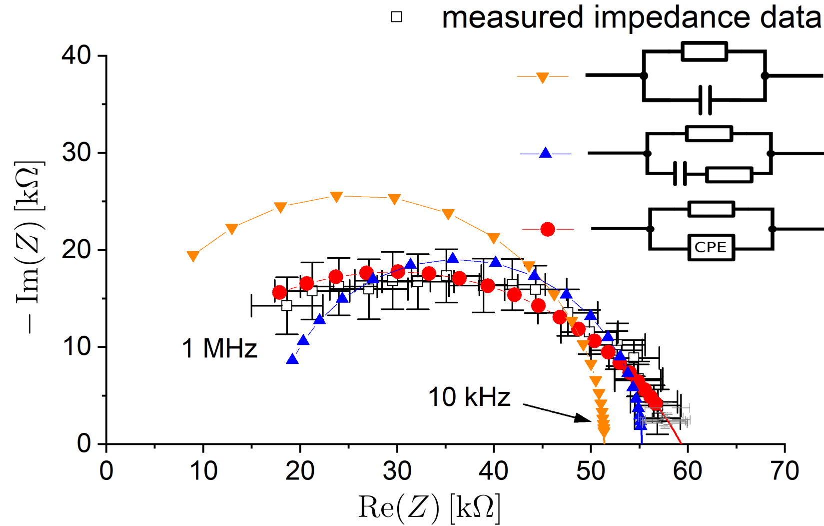

Figure 5.6: Nyquist plot of the high frequency part of the impedance spectrum during deposition of TiO_2 (#3) and fits of three different models evaluated in the range 10 kHz – 1 MHz. The points of the measured data and points at the fitted curves correspond to the same frequencies. The fitted parameters of the third (red) model are: $R_s \approx 59.4$ kΩ, $n \approx 0.7$, $C_s \approx 7$ pF (according to Eq. 5.2).

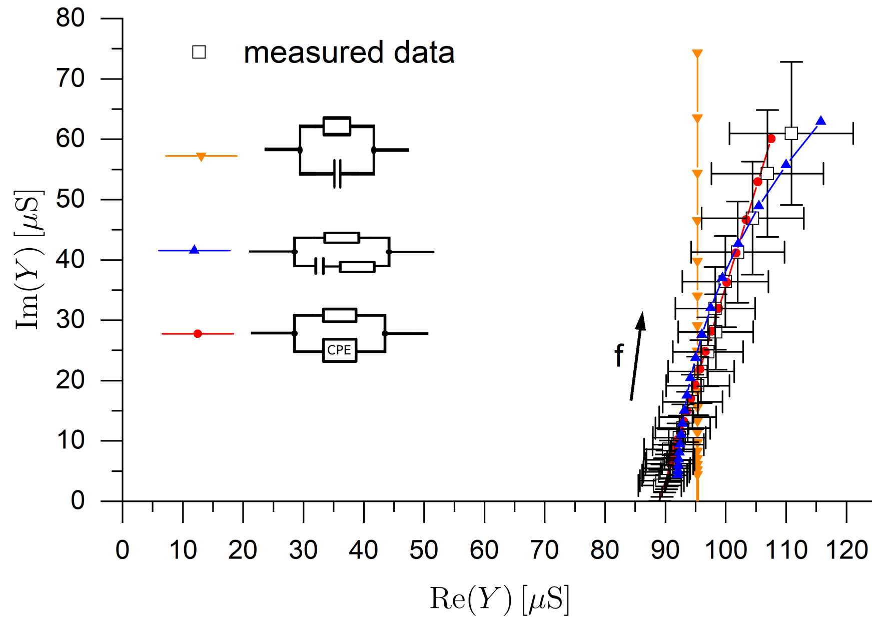

Figure 5.7: Nyquist plot of the admittance $Y = 1/Z$ spectrum after 1 minute of deposition of Fe_2O_3 film (#1) together with the fitted models. These data correspond to the impedance data Z shown in Fig. 5.5.

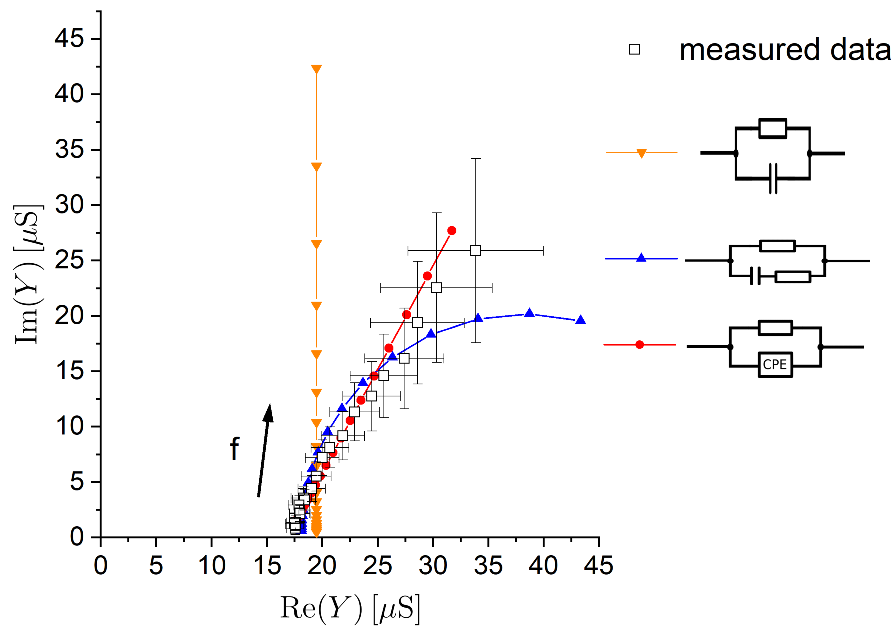

Figure 5.8: Nyquist plot of the admittance $Y = 1/Z$ spectrum during deposition of TiO_2 (#3) together with the fitted models. These data correspond to the impedance data Z shown in Fig. 5.6.

5.3 Dielectric properties of the films

The model of parallel connection of CPE element and ideal resistor was employed to fit the high frequency part of the spectrum corresponding to the sheath impedance Z_s. Interpolation according to this model to lower frequencies was used in order to evaluate the impedance of the deposited film $Z_f = Z - Z_s$. The relative permittivity ϵ_r' and conductivity σ was evaluated according to Eq. 1.64 and Eq. 1.65, respectively. To determine the thickness of the film, it was assumed, that the deposition rate was constant in time. This assumption was supported by subsequent depositions with the QCM (quartz crystal microbalance) positioned in place of the substrate at the same discharge conditions as employed during all three depositions (i.e. for both magnetron and plasma-jet system and Ti and Fe cathode). A linearly decreasing frequency signal from QCM was observed at the time scale of an hour and longer. Moreover, all the depositions were performed at stable discharge conditions (stable discharge voltage).

The deposition rate was obtained from the thickness of the film after deposition, which was deduced from SEM (scanning electron microscope) image of a cross-section of the particular film, see 5.15 and Tab. 5.1.

Figs. 5.9, 5.10 and 5.11 show the frequency dependence of the evaluated dielectric parameters for several selected instants during deposition (different film thicknesses). The error bars of the calculated film properties C_f, ε_r',ε_r'', σ, tg δ were evaluated as maximal errors taking into account the maximal expected errors described in 2.8, together with a supposed error of ± 5 % in R_s and Q obtained from the fits of sheath impedance. However, as it is apparent from the impedance spectra, the two arcs in the Nyquist plots almost do not overlap, and therefore the correction on the sheath capacitance was negligible in comparison to the evaluated errors. For higher frequencies the evaluated errors increase, because two similar impedances Z and Z_s are subtracted according to Eq. 1.60. An error of ± 30 s for the evaluation of the film thickness from the deposition time due to the time spent by measuring of one spectrum was also taken into account (for all the frequencies). That increases the estimated errors mainly at beginning of the deposition when the film is thin. The errors in estimation of the deposited film thickness (and ergo the deposition rate) and possible non-homogeneity of the film thickness is not covered in the error bars because the propagation of this error is straightforward.

The obtained frequency dependencies of the parameters ε_r',ε_r'', σ, tg δ are qualitatively in agreement with expected behavior, see e.g. [65, 50]. The real part of dielectric constant always decreases (or stays constant) with increasing frequency as the slow polarization mechanisms cease to follow the changing electric field and only the faster one's continue to contribute to ε_r'. The reason for the increase of the real part of the dielectric constant ε_r' with decreasing frequency may be caused by interfacial polarization at grain boundaries and inhomogenities in the thin film. The conductivity σ is expected to saturate for very low frequencies at the DC conductivity σ_{DC} which is essentially the conductivity given by bulk material (crystallite) DC conductivity and DC conductivity of grain boundaries and other possible inhomogeneities. Apparently, measurements at even lower fre-

quencies than 1 Hz would be needed to observe saturation of the conductivity. The obtained conductivity for all three samples is in reasonable range observed for semiconductors. The conductivity may change in orders of magnitude and apart from temperature depends e.g. on the amount of impurities, vacancies or grain boundaries. Notice that the evaluated conductivity of the TiO_2 (#3) film is more than one order of magnitude lower than that evaluated for TiO_2 (#2) film.

The loss tangent tg δ decreases with increasing frequency in the observed frequency range, which is mainly due to the decrease of the capacitive reactance $1/(\omega C_f)$ with increasing frequency.

According to recent numerical calculations [67] the static dielectric constants of hematite crystals (α-Fe_2O_3) are $\varepsilon_0^{11} = 26.41$ and $\varepsilon_0^{33} = 17.84$, which correspond to dielectric constant perpendicular and parallel to the c axis of the unit cell, respectively. However, the observed dielectric constant ε_r' of the hematite (#1) film is lower; at the frequency of 2 kHz the evaluated dielectric constant after 21 minutes of deposition is $\varepsilon_r' = 11.5 \pm 1.1$ and it seems to even slightly decrease with increasing the frequency. One possible reason for the lower dielectric constant might be the porosity of the film, which was observed from the SEM cross-section, see Fig. 5.15a,b. Even lower dielectric constants of Fe_2O_3 thin films in the range 1 - 2 were reported in [68].

The evaluated dielectric constant of the TiO_2 (#2) film after 50 min of deposition at 2 kHz is $\varepsilon_r' = 19 \pm 1$. The evaluated dielectric constant of the TiO_2 (#3) film after 104 min of deposition at 100 Hz is $\varepsilon_r' = 16 \pm 1$. Similarly low dielectric constants for amorphous TiO_2 at room temperature were reported in [69] ($\varepsilon_r' =$ 12.4 at 1 kHz) or in [70] ($\varepsilon_r' = 13.7$ at 1 MHz with DC bias; with zero DC bias even 5 times lower). For crystalline TiO_2 usually higher dielectric constants were reported e.g. ≈ 40 for anatase or ≈ 80 for rutile, [71, 72].

As soon as the AC input voltage V_0 was lower than the corresponding electron temperature, I have observed no changes in the obtained data for various V_0.

During deposition of the TiO_2 (#3) film I have also investigated possible dependence of the dielectric constant on the DC bias voltage applied on the thin film. Such measurement was performed after 90 minutes of TiO_2 (#3) film deposition by the following procedure. The measuring circuit was disconnected from the substrate and instead a high input impedance > 1 GΩ voltage follower was connected to the substrate and the floating potential was estimated to be -23.3 V. If the DC blocking capacitor is ideally charged to the same voltage, the DC voltage drop on the film is zero. However, I charged the DC blocking capacitor by an external voltage source to only -18 V and connected it back to the measuring circuit and to the substrate. Due to the much lower capacitance of the film C_f in comparison to the capacitance of the DC blocking capacitor C_B and low conductivity of the film, the film capacitor got charged by electron current to approximately -5.3 V almost suddenly (the characteristic time is approximately given by $R_s C_f \approx 5$ ms), which could be seen by measuring negligible DC current. The characteristic time for the discharge of the thin film capacitor is very large and is given by charging of the DC blocking capacitor through the thin film with a characteristic frequency given by $(R_s + R_f)\,C_B \approx R_f C_B > 300$ s (the resistance

of the film at 1 Hz was used, yet it is clearly apparent from the measured spectra that the DC conductivity of the film was much higher). No significant change in the impedance spectrum and in all the evaluated parameters was observed when the film was DC biased at −5.3 V. Given the thickness of the TiO_2 (#3) film during this experiment was 240 nm, the mean DC electric field in the film can be estimated roughly to 200 kV/cm. After measuring of the impedance spectrum, the voltage on the DC blocking capacitor was still roughly -18 V.

A temporal evolution of the evaluated dielectric parameters during deposition for several selected frequencies is shown in Figs. 5.9, 5.10 and 5.11. Moreover, the temperature of the substrate monitored by a thermocouple is shown. Note that the temperature at the beginning of the deposition is slightly elevated (30 to 40 °C). Even though the sample was hidden behind the shutter, the substrate got heated, when the target was being cleaned in Ar discharge for 15 minutes and more before deposition. As it is apparent from the graphs, the evaluated dielectric constant, conductivity and loss tangent decreases with deposition time (film thickness) for samples (#1) and (#2). For sample (#3) only slight increase of the dielectric constant was observed. The dielectric constant, conductivity and loss tangent seem to saturate as the thickness of the respective film increases; yet with an exception of the dielectric constant at 1 Hz of the sample (#2). From the temporal evolution of all three samples, it seems that the change of the film properties could be related to the increase of the substrate temperature. During deposition of TiO_2 (#3) film, the deposition was purposely interrupted for 40 minutes to let the substrate cool down, see Fig. 5.11b. As the deposition was resumed, the evaluated conductivity was even lower and then slightly increased while the substrate temperature increased. A small decrease in the dielectric constant at 1 Hz and 10 Hz was also detected, which was then seen to slightly increase with the increasing temperature to the original value before cooling. Hence, this experiment showed, that the temporal evolution of the evaluated parameters for the film (#3) can't be explained solely by the change of the substrate temperature. The observed temporal evolution of the film properties might be caused also by structural changes of the film during deposition.

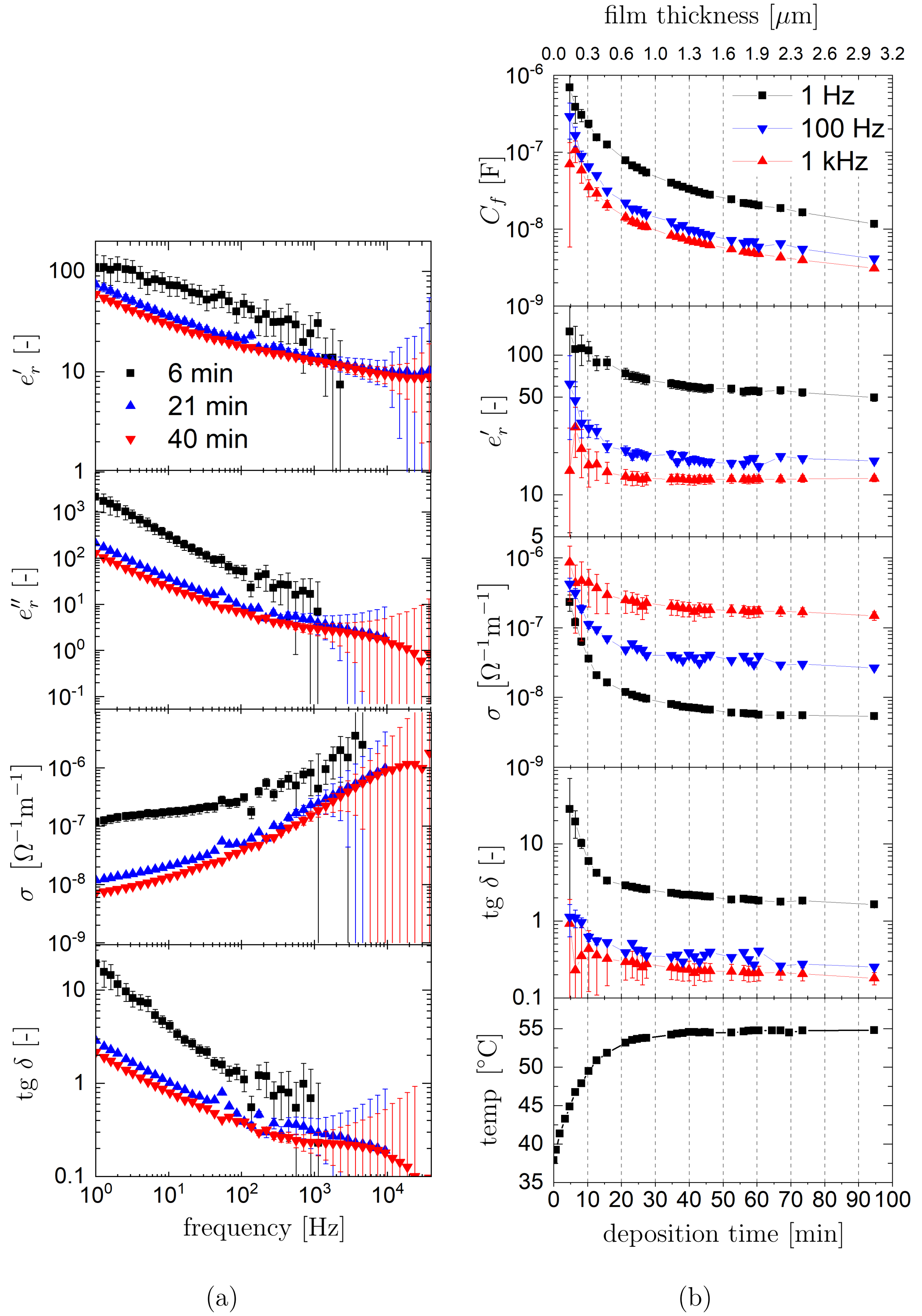

Figure 5.9: Several properties of the Fe_2O_3 (#1) film; (a) frequency dependence for the three instants during deposition, (b) temporal evolution of the film dielectric properties and the substrate temperature during deposition. These data have been retrieved from the impedance spectra some of which are shown in Fig. 5.1 and Fig 5.2.

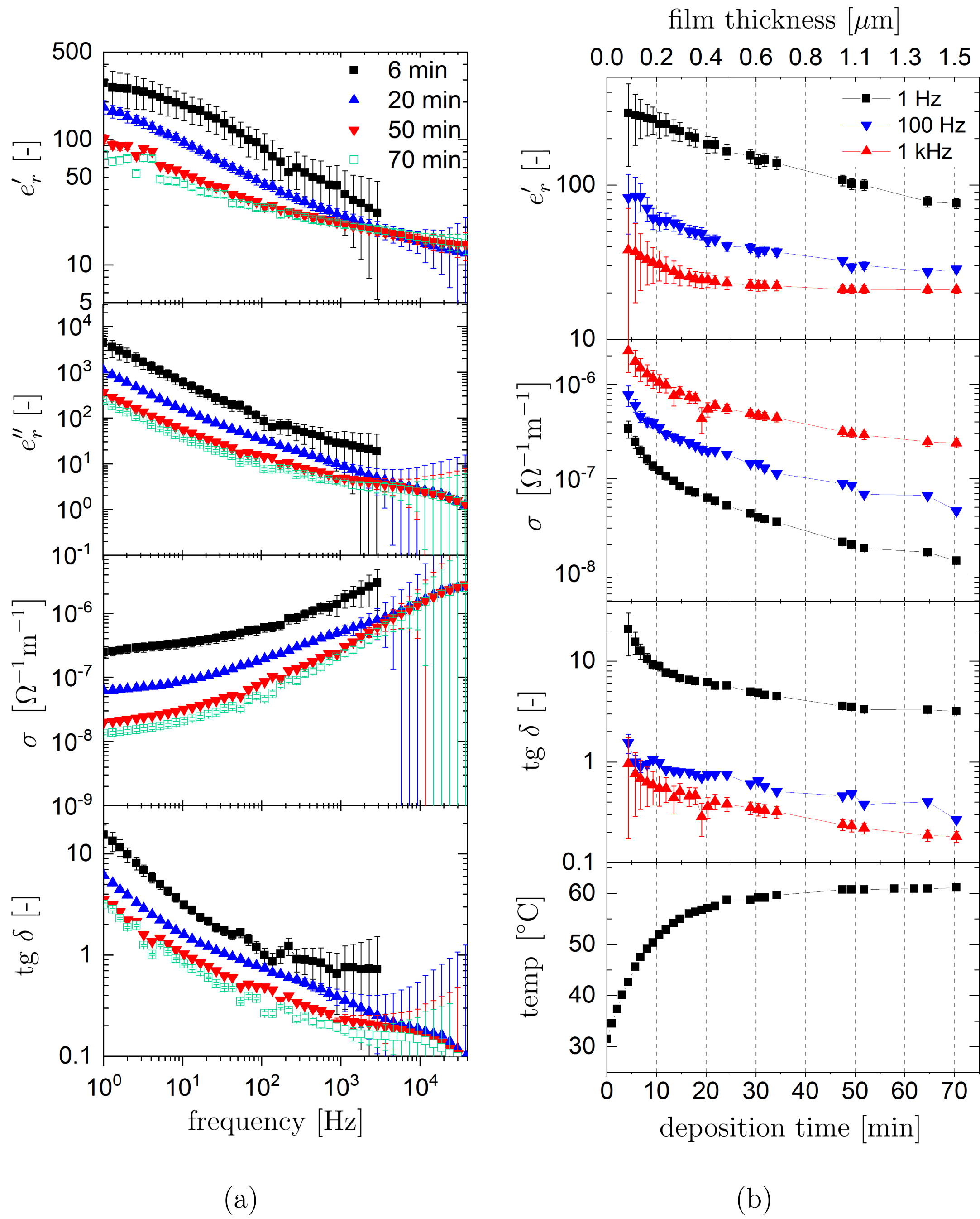

Figure 5.10: Several properties of the TiO_2 (#2) film; (a) frequency dependence for the four instants during deposition, (b) temporal evolution of the film dielectric properties and the substrate temperature during deposition.

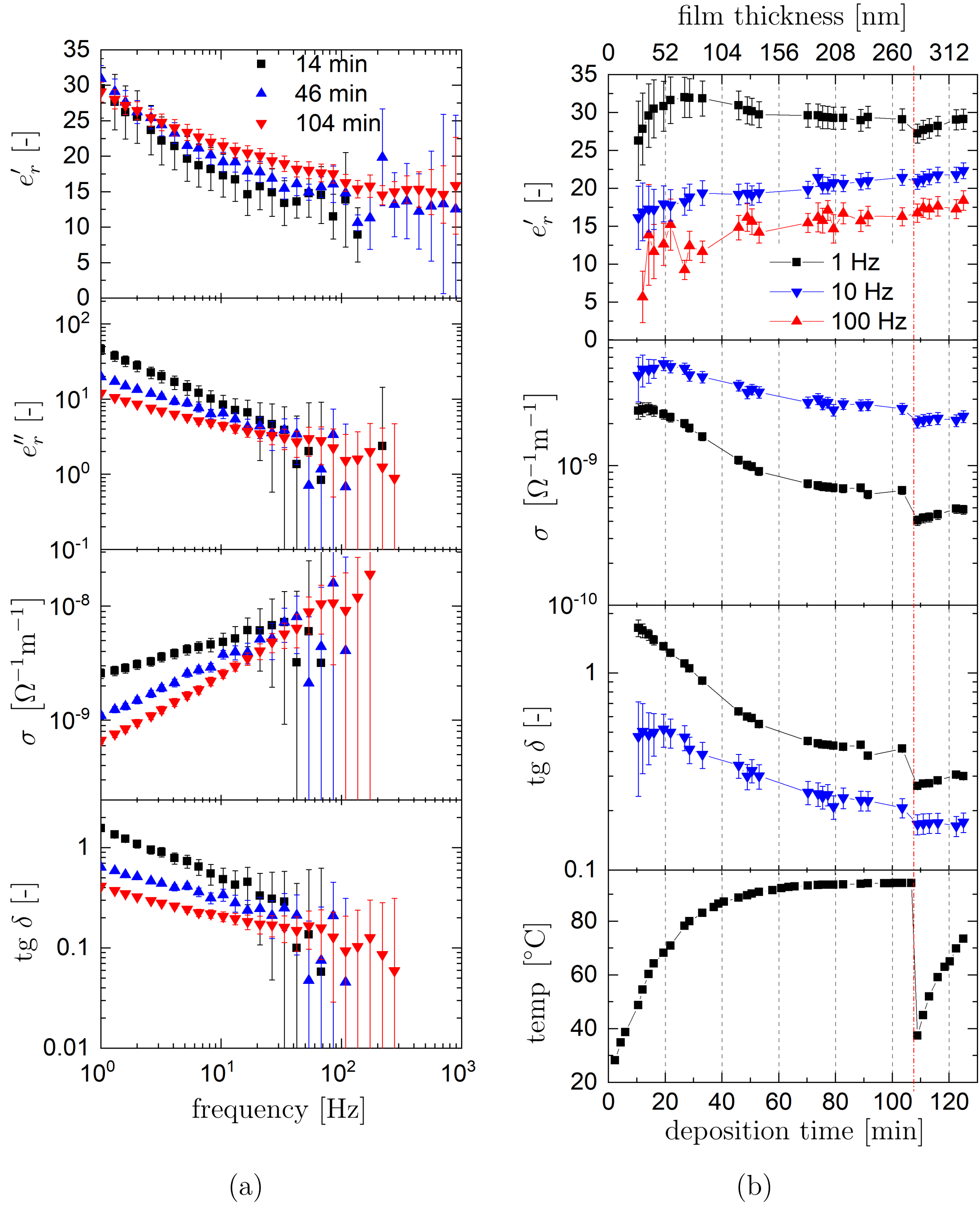

Figure 5.11: Several properties of the TiO_2 (#3) film; (a) frequency dependence for the three instants during deposition, (b) temporal evolution of the film dielectric properties and the substrate temperature during deposition. These data have been retrieved from the impedance spectra some of which are shown in Fig. 5.3. The vertical red dashed line depicts the instant, when the deposition was purposely interrupted, to let the substrate and the thin film cool down.

5.4 Ex-situ characterization of the films

The deposited films were analyzed by colleagues from the Institute of Physics of the Czech Academy of Sciences. Raman spectroscopy measurements were made by means of Renishaw Raman microscope RM 1000 (unpolarized beam in back scattering mode of a 514.5 nm Ar^+ laser). The film cross-sectioning was performed by FIB (Focused Ion Beam) milling technique by means of the FEI Quanta 3D Dual-Beam SEM/FIB system utilizing Ga^+ ion source. The same system was used for SEM (scanning electron microscope) measurements using electron beam of 5 keV and EDS analysis (Energy-dispersive X-ray spectroscopy) using electron beam of 5 keV for assessment of the elemental composition of the films.

According to the Raman spectra shown in Fig. 5.12a the Fe_2O_3 (#1) film can be said to be crystalline with the hematite structure. There are seven phonon modes expected in the Raman spectrum of hematite at ambient conditions as predicted and experimentally observed [73, 74]. There are expected two A_{1g} modes (at 225 and 498 cm^{-1}) and five E_g modes (at 247, 293, 299, 412 and 613 cm^{-1}). In the spectrum of the sample (#1), the peak corresponding to E_g mode at 247 cm^{-1} is not recognizable. The peaks corresponding to E_g modes at 293 and 299 cm^{-1} are probably overlapping. Almost all the peaks (probably except from A_{1g} at 498 cm^{-1}) are down-shifted of about 10 cm^{-1} than expected. Such shifts of peaks correspond to increase in the length of the chemical bonds, which may be caused e.g. due to internal stress in the film. On the contrary, increase of the Raman peaks of hematite for increasing pressure above the ambient pressure was studied in [74].

From the Raman spectra of both the TiO_2 samples (#2) and (#3) shown in Fig. 5.12b, it can be concluded, that they predominantly exhibit an amorphous structure. An amorphous structure of TiO_2 was observed also in [75] deposited in the the same plasma-jet system, yet at different conditions (100 Pa, 100 and 300 sccm Ar flow, 42 mm substrate distance, 200 mA discharge current). Annealing of the samples at 400 °C was needed in [75] to obtain anatase crystalline structure, see also [76].

In Fig. 5.15 you can see the SEM cross-sectional images after the cross-sectioning by FIB. On top of the film the protective Pt layer can be seen, which protected the film from being damaged during Ga^+ ion milling.

The SEM scans of the surface morphology of Fe_2O_3 (#1) film, see Fig. 5.16a,b and Fig 5.14a, show distinct grains with a shape of nano-pyramids. Very similar morphology with comparable size of the grains of Fe_2O_3 films deposited by means of hollow-cathode has been reported in [77]. Moreover, the cross-sectional SEM scans in Fig. 5.15a,b show a high porosity of the (#1) film. The SEM analysis of the TiO_2 (#2) film shows thickness-through nano-cracks, whose width at the surface ranged up to 70 nm, see Fig. 5.16 and Fig. 5.15c,d. Columnar TiO_2 films with micro-cracks deposited in the same hollow-cathode system were reported in [78]. No cracks were observed in the TiO_2 (#3) film.

The spectra from the EDS analysis are shown in Fig. 5.13. The quantitative analysis of the elemental composition of the films, shows higher fraction of oxygen atoms than would correspond to ideal stoichiometric composition. According to

the EDS analysis of the Fe_2O_3 (#1) film, the evaluated atomic ratio Fe:O is only 0.4, although the ideal stoichiometric ratio Fe:O for Fe_2O_3 should be 0.66. Both the samples TiO_2 (#2) and TiO_2 (#3) show an atomic ratio Ti:O of 0.4. In all three samples a rather higher amount (≈ 8 %) of carbon impurities were found, which could have been caused by contamination from atmosphere due to a longer time between the deposition of the samples and EDS analysis (2 months) or due to the presence of the Teflon tape during the deposition. A 4% carbon contamination of TiO_2 films deposited in the same system was reported in [60].

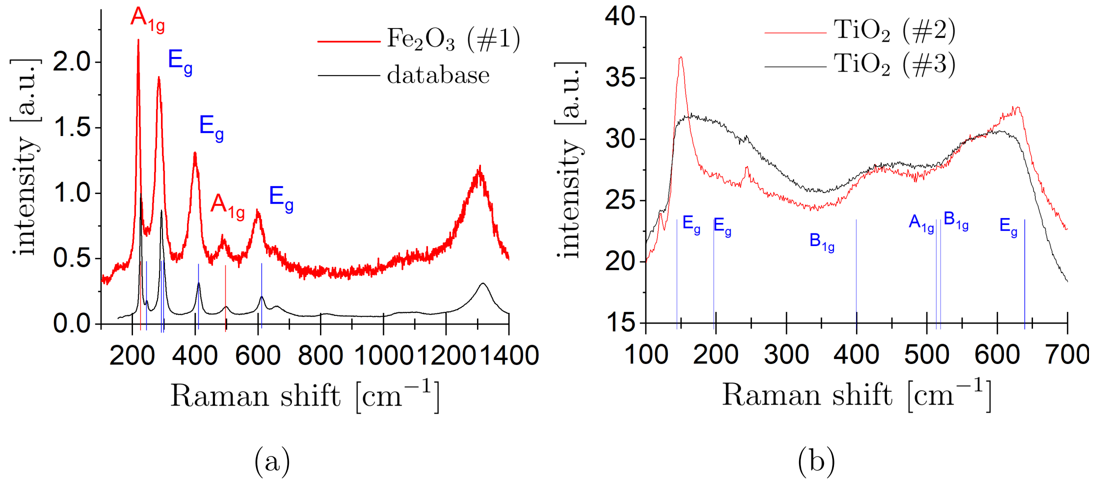

Figure 5.12: Raman spectrum of the Fe_2O_3 (#1) film (a) and TiO_2 (#2) and (#3) films (b). The hematite database spectrum is taken from [73]. In (b) the frequencies corresponding to anatase Raman modes are depicted by the lines, taken from [79].

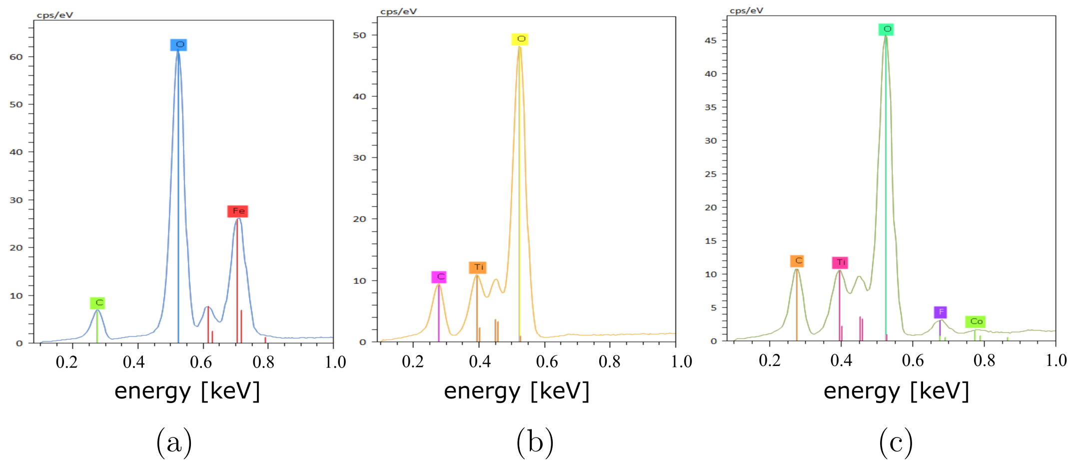

(a) (b) (c)

Figure 5.13: EDS spectra of Fe_2O_3 (#1) film (a); TiO_2 (#2) film (b) and TiO_2 (#3) film (c).

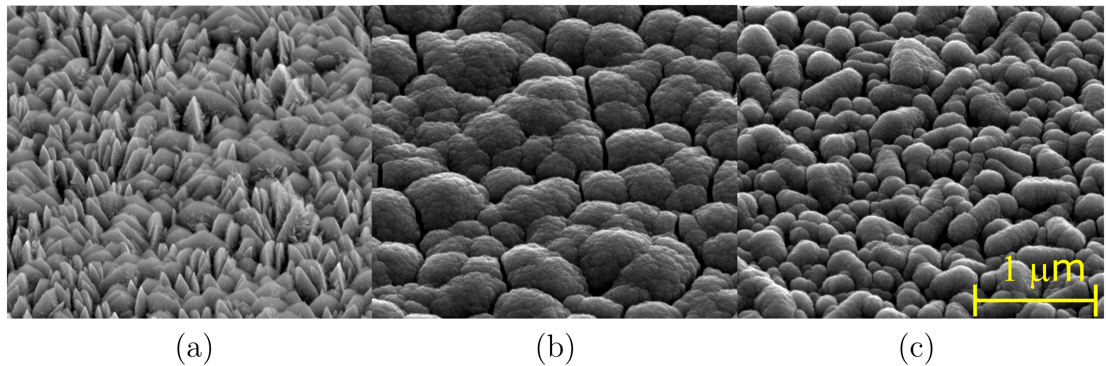

(a) (b) (c)

Figure 5.14: SEM views of the surface of the Fe_2O_3 (#1) film (a); TiO_2 (#2) film (b) and TiO_2 (#3) film (c). All the scans were taken at the tilt angle of 52° with respect to the normal of the film surface. The scale shown is the same for all three pictures.

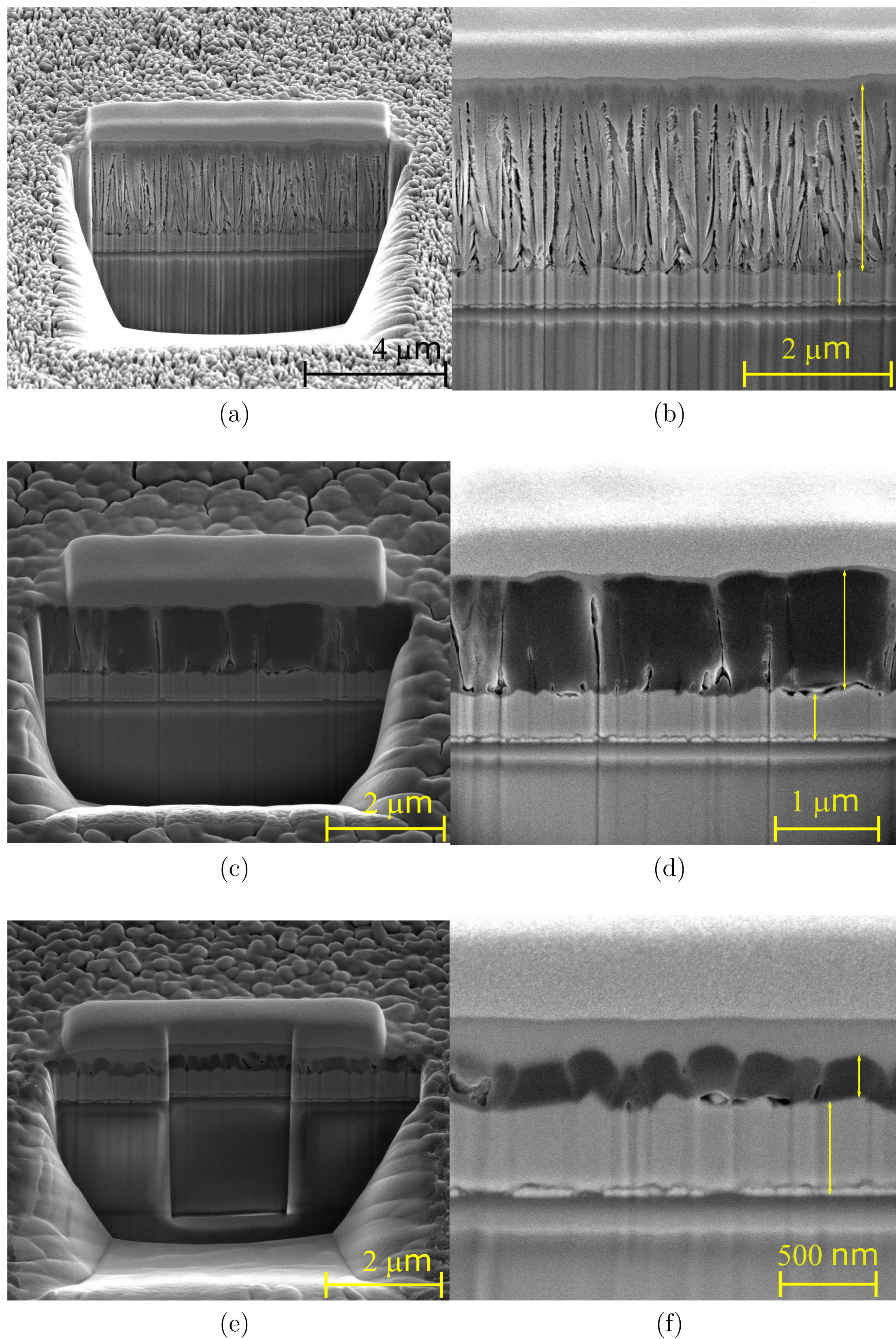

Figure 5.15: SEM views of the cross-section of the Fe_2O_3 (#1) film (a,b); TiO_2 (#2) film (c,d) and TiO_2 (#3) film (e,f). All the scans were taken at the tilt angle of 52° with respect to the normal of the film surface. The thickness of the FTO layer and of the deposited layer is indicated by the arrows.

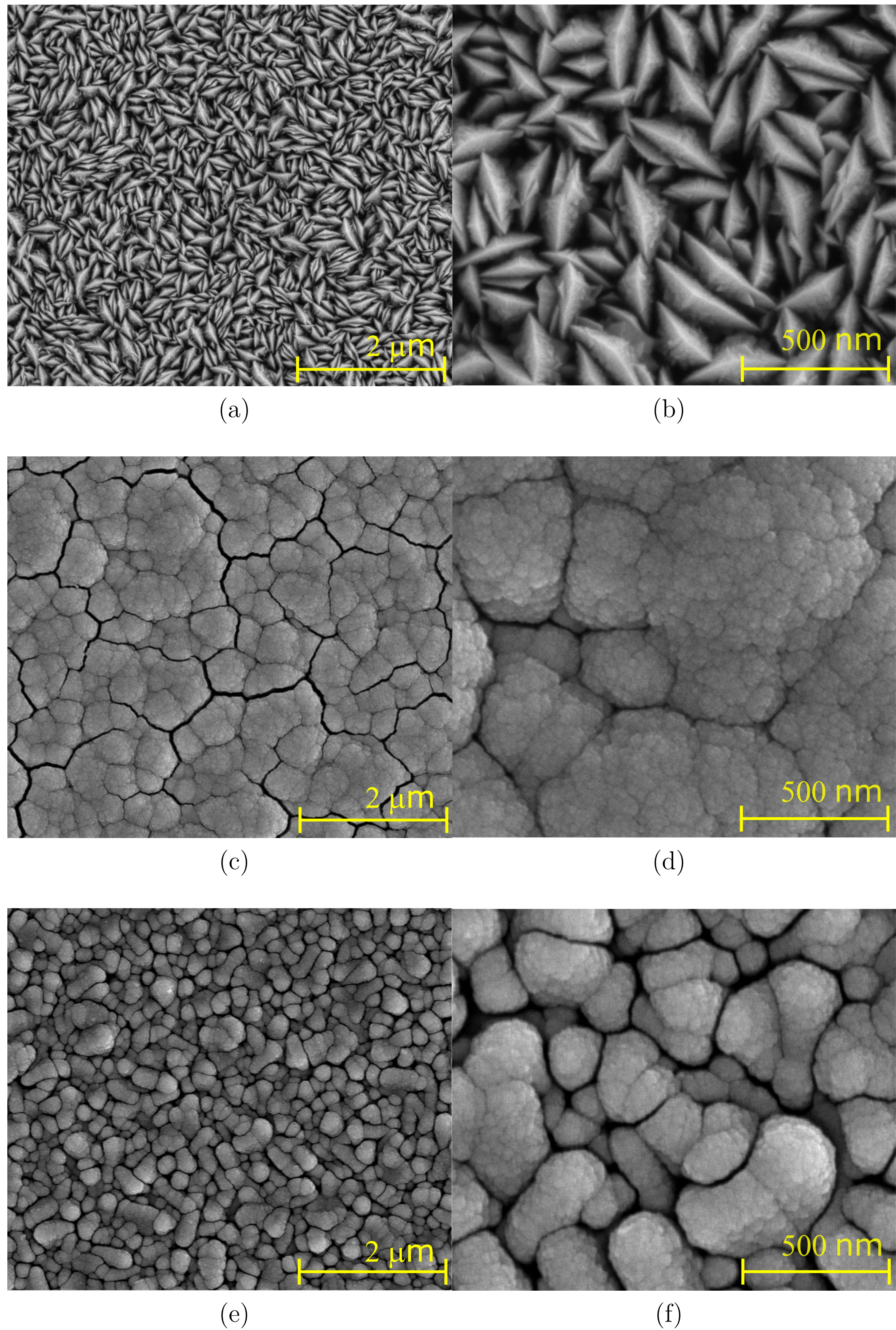

Figure 5.16: SEM views of the surface of the Fe_2O_3 (#1) film (a,b); TiO_2 (#2) film (c,d) and TiO_2 (#3) film (e,f). All the scans were taken at the tilt angle of 0° with respect to the normal of the film surface.

Conclusion

This work was dedicated to study of several new methods intended for diagnostics during plasma-aided deposition processes of non-conductive and/or semiconductive thin films. In first place, the work focused on an experimental study of a relatively novel diagnostic method called the Floating harmonic probe for measurement of the electron temperature and ion density of processing plasmas. The comparative measurements performed at a broad range of experimental conditions in the hollow-cathode plasma jet system in a DC continuous regime showed a satisfactory agreement between both the electron temperature and ion density measured by FHP and a conventional Langmuir probe. Different ion current theories were compared when evaluating the ion density. The ion density estimated by the collisionless Laframboise theory was found to be in reasonable agreement with the electron density data at the studied discharge conditions. The FHP method was proved to measure reliable data even when the probe was deposited by an iron oxide film and the IV characteristics of the Langmuir probe were highly distorted. As expected, the FHP method yields unperturbed results only when the impedance of the deposited film is much lower than the resistance of the plasma sheath around the probe. Hence, these two parameters should be considered when using the FHP. A certain disadvantage of the FHP method is, that in the case of non-Maxwellian EEDF, the probe measures the electron temperature representing the EEDF only at energies corresponding to voltages around the floating potential. Great advantage of this method is its relatively simple application during continuously driven discharges, straightforward evaluation of the data from the measured waveforms and moreover, it can be realized my means of commonly used laboratory instruments. The FHP measurements in the continuously driven plasma-jet system were published in [A2].

The FHP method was studied also due to its potential applications in diagnostics of pulsed discharges which are very often used for deposition of non-conductive or semiconductive films. The FHP method utilizing the Phase Delay Harmonic Analysis Method was studied in both the planar magnetron and hollow-cathode plasma jet systems operated in pulsed DC regime. It was showed that the reliability of the results using the FHP method in pulsed discharges highly depends on the particular discharge conditions and mainly on the temporal evolution of the floating potential. When using the single FHP method, very good results during the active pulse and in the afterglow in comparison with the time-resolved Langmuir probe method measured in non-reactive regime in magnetron were obtained at various discharge conditions, when a DC blocking capacitor with a suitably low capacitance was used. The measurement with FHP was several times faster and usually less noisy than that obtained with the time-resolved LP technique. To find the optimally lowest value of the DC blocking capacitor, one should take into account mainly the size of the probe, the maximum densities expected during the measurement and possibly also the electron temperature. However, the fact that the sheath impedance actually depends on the probe transient voltage further complicates the choice. It was shown, that it

is not generally guaranteed, that the single FHP probe will provide reliable data. During measurements in the hollow-cathode in pulsed regime, the single FHP was usually found to provide not very reliable data. To deal with the inherent problem of single FHP, I decided to study and apply the double FHP for diagnostics of the pulsed driven discharges. The double FHP is based on a similar operational principal as the single FHP. However, no DC blocking capacitor is needed which increases the capacitance of the single FHP probe to ground (the reference electrode). The double FHP was found to provide reliable measurement of the electron temperature even during fast changes of the floating potential. A limiting assumption of the double FHP is that the transient currents must be negligible and the double FHP must operate at the floating potential, unless a suitable formula to account for the transient current of double FHP is found in the future. In that case, the measurement of the probe transient current would need to be performed near the probe tip inside the vacuum chamber. It is possible to increase the response of the double FHP to the transients of the floating potential by increasing the size and the collecting area of the probes, which is not possible with the single FHP method. Another approach to improve in the future the FHP technique which might be feasible and more reliable is to use a single FHP with an active compensation of the transients of the floating potential. The FHP measurements in the pulsed DC driven magnetron system were published in [A1].

A new method for characterization of the electrical and dielectric properties of deposited dielectric films directly inside the vacuum chamber during deposition was proposed and experimentally studied. Impedance spectra measured during deposition of three different films were carefully analyzed. The impedance spectra recorded in the range 1 Hz - 1 MHz featured roughly two arcs in the Nyquist plot as predicted by the simple equivalent circuit model. The impedance of the plasma sheath and the impedance characterizing the deposited film could be separated from the measured net impedance during all three depositions. A frequency dependence of the thin film parameters - the dielectric constant, conductivity and the loss tangent, and their temporal evolution during growth of the film could be obtained, provided the thin film thickness is known. The evaluated thin parameters were in reasonable range of values reported in other works studying the properties of iron oxide and titanium oxide films. The results indicated a high perspective for future research of this method and its applicability for characterizing of deposited thin films and study of deposition processes.

Bibliography

[1] P. M. Martin. *Handbook of deposition technologies for films and coatings: Science, Applications and Technology.* Elsevier Inc., Oxford, 2010.

[2] A. Schwabedissen, C. Soll, A. Brockhaus, and J. Engemann. Electron density measurements in a slot antenna microwave plasma source by means of the plasma oscillation method. *Plasma Sources Sci. Technol.*, 8(3):440–447, 1969.

[3] R.B. Piejak, V.A. Godyak, R. Garner, and B.M. Alexandrovich. The hairpin resonator: A plasma density measuring technique revisited. *J. Appl. Phys.*, 95(7):3785, 2004.

[4] T. Styrnoll, J. Harhausen, M. Lapke, and R. Storch et al. Process diagnostics and monitoring using the multipole resonance probe in an inhomogeneous plasma for ion-assisted deposition of optical coatings. *Plasma Sources Sci. Technol.*, 22(4):045008, 2013.

[5] T. Styrnoll, S. Bienholz, M. Lapke, and P. Awakowitcz. Study on electrostatic and electromagnetic probes operated in ceramic and metallic depositing plasmas. *Plasma Sources Sci. Technol.*, 23(2):025013, 2014.

[6] N.St.J. Braithwaite, J.P. Booth, and G. Cunge. A novel electrostatic probe method for ion flux measurements. *Plasma Sources Sci. Technol.*, 5:677–684, 1996.

[7] M.A. Sobolewski. Measuring the ion current in electrical discharges using radio-frequency current and voltage measurements. *Appl. Phys. Lett.*, 72(10):1146, 1998.

[8] D. Lundin, M. Čada, and Z. Hubička. Time-resolved ion flux and impedance measurements for process characterization in reactive high-power impulse magnetron sputtering. *J. Vac. Sci. Technol. A*, 34(4):041305, 2016.

[9] S.W. Rayment and N.D. Twiddy. Time-resolved measurements of electron energy distributions. *J. Phys. D: Appl. Phys.*, 2(12):1747–1754, 1969.

[10] M-H. Lee, S-H. Jang, and Ch-W. Chung. Floating probe for electron temperature and ion density measurement applicable to processing plasmas. *J. Appl. Phys.*, 101(3):033305, 2007.

[11] Y-S. Kim, D-H. Kim, H-C. Lee, and Chung C-W. Pulsed plasma measurement method using harmonic analysis. *J. Appl. Phys.*, 117(24):243302, 2015.

[12] E. Barsoukov and J.R. Macdonald (Eds.). *Impedance Specrosopy: Theory, Experiment, and Applications, 2nd edition.* John Wiley & Sons, Inc., Hoboken, 2005.

[13] L.J. van der Pauw. A method of measuring specific resistivity and Hall effect of discs of arbitrary shape. *Philips Tech. Rev.*, 20:220–224, 1958.

[14] S-H. Jang, G-H. Kim, and C-W. CHung. In situ method for real time measurement of dielectric film thickness in plasmas. *J. Appl. Phys.*, 107(2):023303, 2010.

[15] J-Y. Kim and C-W. Chung. Real-time dielectric-film thickness measurement system for plasma processing chamber wall monitoring. *Rev. Sci. Instrum.*, 86(12):123502, 2015.

[16] K. Ellmer. *Magnetron Discharges for Thin Film Deposition v Low Temperature Plasma, Fundamentals, Technologies, and Techniques, Vol. 1, ed. R. Hippler, H. Kersten, M. Schmidt, K.H. Schoenbach.* Willey-VCH., Berlin, 2008.

[17] K. Sarakinos, J. Alami, and S. Konstantinidis. An r.f. plasma jet applied to diamond, glassy carbon and silicin carbide film synthesis. *Surf. Coat. Technol.*, 204:1661–1684, 2010.

[18] L. Bárdoš, S. Berg, T. Nyberg, H. Baránková, and C. Neder. An r.f. plasma jet applied to diamond, glassy carbon and silicin carbide film synthesis. *Diamond and Related Materials*, 2:517–522, 1993.

[19] H. Baránková, L. Bárdoš, and S. Berg. Titanium nitride deposited by high rate rf hollow cathode plasma jet reactive proces. *Vacuum*, 46:1433–1438, 1995.

[20] M. Čada, Z. Hubička, P. Adámek, and P. Ptáček at al. Investigation of RF and DC plasma jet system during deposition of higly oriented ZnO films. *Surf. Coat. Tech.*, 174-175:627–631, 2003.

[21] Z. Hubička, M. Chichina, A. Deyneka, and P. Kudrna at al. Low pressure plasma-jet systems and their application for deposition of ceramic thin films. *Journal of Optoelectronics and Advanced Materials*, 9:875–880, 2007.

[22] H. M. Mott-Smith and I. Langmuir. The theory of collectors in gaseous discharges. *Phys. Rev.*, 28(4):727–763, 1926.

[23] S. Pfau and M. Tichý. *Langmuir probe diagnostics of low-temperature plasma, Fundamentals, Technologies, and Techniques, Vol. 1, ed. R. Hippler, H. Kersten, M. Schmidt, K.H. Schoenbach.* Willey-VCH., Berlin, 2008.

[24] J.R. Sanmartin. Theory of a probe in a strong magnetic field. *Phys. Fluids*, 13(1):103–116, 1970.

[25] F.F. Chen. *Electric probes, Plasma diagnostic techniques, ed. by R.H. Huddlestone, S.L. Leonard.* Academic Press, New York, 1965.

[26] D. Bohm, E.H.S. Burhop, and H.S.W. Massey. *Characteristics of electrical discharges in magnetic fields, ed. A. Guthrie, R.K. Wakerling.* McGraw-Hill, New York, 1949.

[27] K-U. Riemann. The Bohm criterion and sheath formation. *J. Phys. D: Appl. Phys.*, 24:493–518, 1991.

[28] N. Hershkowitz. *How Langmuir probes work, Plasma Diagnostics, Vol. 1, ed. O. Auciello, D.L. Flamm.* Academic, New York, 1989.

[29] J.E. Allen, R.L.F. Boyd, and P. Reynolds. The collection of positive ions by a probe immersed in a plasma. *Proc. Phys. Soc. B*, 70:297–304, 1957.

[30] F.F. Chen. Numerical computations for ion probe characteristics in a collisionless plasma. *J. Nucl. Energy, Part C*, 7(1), 1965.

[31] S. Klagge. *Plasmadiagnostik durch elektrostatische Sonden unter nichtidealen Bedingungen.* PhD thesis, University of Greifswald, Germany, 1988.

[32] F.F. Chen and D. Arnush. The floating potential of cylindrical Langmuir probes. *Phys. Plasmas*, 8(11), 2001.

[33] J.I Fernández Palop, J. Ballesteros, V. Colomer, and M.A. Hernández. Theoretical ion current to cylindrical Langmuir probes for finite ion temperature values. *J. Phys. D: Appl. Phys.*, 29(11):2832–2840, 1996.

[34] I.B. Bernstein and J.N. Rabinowitz. Theory of electrostatic probes in a low-density plasma. *Phys. Fluids*, 2(2):112–121, 1959.

[35] J.G. Laframboise. Theory of spherical and cylindrical Langmuir probes in a collisionless, Maxwellian plasma at rest. Univ. of Toronto, Institute for Aerospace Studies (UTIAS), Report 100, 1966.

[36] O. Chudáček, P. Kudrna, J. Glosík, M. Šícha, and M. Tichý. Langmuir probe determination of charged particle number density in a flowing afterglow plasma. *Contrib. Plasma. Phys.*, 35(6):503–516, 1995.

[37] D.J. Field, S.K. Dew, and R.E. Burrell. Spatial survey of a magnetron plasma sputtering system using a Langmuir probe. *J. Vac. Sci. Technol. A*, 20(6):2032–2041, 2002.

[38] M.J. Druyvesteyn. Der Niedervoltbogen. *Z. Physik*, 64:781, 1930.

[39] R. Van Nieuwenhove and G. Van Oost. Novel Langmuir probe technique for real-time measurement of the electron temperature. *Rev. Sci. Instrum.*, 59(7):1053–1056, 1988.

[40] J. A. Boedo, D. Gray, R. W. Conn, and P. Luong et al. On the harmonic technique to measure electron temperature with high time resolution. *Rev. Sci. Instrum.*, 70(7):2997–3006, 1999.

[41] J. Pang, W. Lu, Y. Xin, and H. Wang et al. Plasma diagnosis for microwave ECR plasma enhanced sputtering deposition of DLC films. *Plasma Sci. Technol.*, 14(2):172–176, 2012.

[42] Y. Bai, J. Li, J. Xu, and W. Lu et al. Improvement of the harmonic technique of probe for measurements of electron temperature and ion density. *Plasma Sci. Technol.*, 18(1):58–61, 2016.

[43] S.-J. Oh, I.-J. Choi, J.-Y. Kim, and Ch.-W. Chung. Double probe diagnostics based on harmonic current detection for electron temperature and electropositive ion flux measurement in rf plasmas. *Meas. Sci. Technol.*, 23(8):085001, 2012.

[44] S-H. Jang, G-H. Kim, and C-W. Chung. Harmonic analysis of sideband signals generated in plasmas. *Thin Solid Films*, 519(20):7042–7044, 2011.

[45] D-H. Kim, H-C. Lee, Y-S. Kim, and C-W. Chung. Plasma diagnostic method using intermodulation frequencies in a Langmuir probe. *Appl. Phys. Lett.*, 103(8):084103, 2013.

[46] J-Y. Bang, K. Yoo, D-H. Kim, and Ch-W. Chung. A plasma diagnostic technique using a floating probe for the dielectric deposition process. *Plasma Sources Sci. Technol.*, 20(6):065005, 2011.

[47] K-H. Kim, D-H. Kim, and Ch-W. Chung. Nonlinear circuit analysis of harmonic currents in a floating Langmuir probe with a capacitive load. *Plasma Sources Sci. Technol.*, 26(2):025001, 2017.

[48] M. Abramowitz and I. A. Stegan. *Handbook of Mathematical Functions*. Dover Publications, New York, 1972.

[49] E.O. Johnson and L.Malter. A floating double probe method for measurements in gas discharges. *Phys. Rev.*, 80(1):58–68, 1950.

[50] F. Kremer and A. Schőnhals. *Theory of dielectric relaxation, Broadband dielectric spectroscopy, ed. by F. Kremer and A. Schőnhals*. Springer-Verlag, Berlin, 2003.

[51] V. Kučera. *Pulsed high power supply operating at low frequencies range for plasma generation*. Bachelor's thesis, University of South Bohemia, České Budějovice, Czech Republic, 2015. full text on `https://theses.cz/id/c99aup/KUCERA_BP_2015.pdf`.

[52] J. Klusoň. *Pulsed plasma systems*. PhD thesis, Charles University, Prague, Czech Republic, 2013.

[53] Z. Turek. *Probe diagnostics of the pulse-generated plasma*. Bachelor's thesis, Charles University, Prague, Czech Republic, 2018.

[54] M.J. Pan, M. Zhang, T.T. Li, W. Zheng, Q. Zhao, B. Rao, and G. Zhuang. Winde-band optical coupling isolation amplifier for the Joint TEXT tokamak. *Fusion Eng. Des.*, 96-97:1026–1032, 2015.

[55] F.J. Harris. On the use of windows for harmonic analysis with discrete fourier transform. *Proc. IEEE*, 66:51–83, 1978.

[56] P.R. Bevington and D.K. Robinson. *Data reduction and error analysis for the physical sciences, 3rd edition.* McGraw-Hill, Boston, 2003.

[57] E. Jones, E. Oliphant, and P. Peterson et al. Scipy: Open source scientific tools for python, 2001. `http://www.scipy.org/`.

[58] J. Klusoň, P. Kudrna, and M. Tichý. Measurement of the plasma and neutral gas flow velocities in a low-pressure hollow-cathode plasma jet sputtering system. *Plasma Sources Sci. Technol.*, 22(1):015020, 2013.

[59] R. Perekrestov, P. Kudrna, and M. Tichý. The deposition of titanium dioxide nanoparticles by means of a hollow cathode plasma jet in dc regime. *Plasma Sources Sci. Technol.*, 24(3):035025, 2015.

[60] R. Perekrestov. *The investigation of low pressure HCPJ system for TiO_2 film deposition.* PhD thesis, Charles University, Prague, 2016.

[61] J. Basu and C. Sen. Sheath thickness for a cylindrical or spherical probe placed in a plasma. *Japan. J. Appl. Phys.*, 12(7), 1973.

[62] G.Y. Yushkov and A. Anders. Origin of the delayed current onset in high-power impulse magnetron sputtering. *IEEE T. Plasma Sci*, 38(11):3028–3034, 2010.

[63] M.A. Sobolewski. Experimental test of models of high-plasma-density, radio-frequency sheats. *Phys. Rev. E*, 59(1059), 1999.

[64] J. Jacquelin. A number of models for CPA impedances of conductors and for relaxation in non-debye dielectrics. *J. Non-Cryst. Solids*, 131-133(1059), 1991.

[65] M.V. Nikolic, M.P. Slankamenac, N. Nikolic, and D.L. Sekulic et al. Study of dieletric behavior and electrical properties of hematite α-Fe_2O_3 doped with Zn. *Sci. Sintering*, 44(3):307–321, 2012.

[66] G.J. Brug, A.L.G. van Eeden, M. Sluyters-Rehbach, and J.H. Sluyters. The analysis of electrode impedances complicated by the presence of a constant phase element. *Journal of Electroanalytical Chemistry and Interfacial Electrochemistry*, 176(1-2):275–295, 1984.

[67] R.A. Lunt, A.J. Jackson, and A. Walsh. Dielectric response of Fe_2O_3 crystals and thin films. *Chem. Phys. Lett.*, 586:67–69, 2013.

[68] S.S. Shinde, R.A. Bansode, C.H. Bhosale, and K.Y. Rajpure. Physical properties of hematite α-Fe_2O_3 thin films: application to photoelectrochemical solar cells. *J. Semicond.*, 32:013001, 2011.

[69] B. Babuji, C. Balasubramanian, and M. Radhakrishnan. Dielectric properties of ion plated titanium oxide thin films. *J. Non-Cryst. Solids*, 55:405–412, 1983.

[70] W.G. Lee, S.I. Woo, J.C. Kim, and S.H. Choi at al. Preparation and properties of amorphous TiO_2 thin films by plasma enhanced chemical vapour deposition. *Thin Solid Films*, 237:105–111, 1978.

[71] P. Alexandrov, J. Koprinarova, and D. Todorov. Dielectric properties of TiO_2-films reactively sputtered from Ti in an RF magnetron. *Solid-State. Electron.*, 47:1333, 1996.

[72] V-S. Dang, H.P. Parala, J.H. Kim, and K. Xu et al. Electrical and optical properties of TiO_2 thin films prepared by plasma-enhanced atomic layer deposition. *Phys. Status Solidi A*, 211(2):416–424, 2014.

[73] D.L.A. de Faria, S. Venancio Silva, and M.T. de Oliveira. Raman microspectroscopy of some iron oxides and oxyhydroxides. *J. Raman Spectrosc.*, 28(11):873–878, 1997.

[74] S-H. Shim and T.S. Duffy. Raman spectroscopy of Fe_2O_3 to 62 GPa. *Am. Mineral.*, 87:318–326, 2001.

[75] R. Perekrestov, P. Kudrna, M. Tichý, and I. Khalakhan et al. Crystalline structure and morphology of TiO_2 thin films deposited by means of hollow-cathode plasma jet with supporting anode. *Surf. Coat. Technol.*, 291:123–129, 2016.

[76] S. Miszczak and B. Pietrzyk. Anatase-rutile transformation of TiO_2 sol-gel coatings deposited on different substrates. *Ceram. Int.*, 41:7461–7465, 2015.

[77] Z. Hubička, Š. Kment, J. Olejníček, and M. Čada et al. Deposition of hematite Fe_2O_3 thin film by dc pulsed magnetron and DC pulsed hollow cathode sputtering system. *Thin Solid Films*, 549:184–191, 2013.

[78] R. Perekrestov, P. Kudrna, S. Daniš, and M. Tichý at al. Application of microcracked columnar TiO_2 thin films deposited by dc hollow cathode plasma jet in dye-sensitized solar cells. *J. Vac. Sci. Technol. A*, 35(6), 2017.

[79] T. Ohsaka, F. Izumi, and Y. Fujiki. Raman spectrum of anatase, TiO_2. *J. Raman Spectrosc.*, 7:321–324, 1978.

List of symbols and abbreviations

AC	alternating (not necessarily current)
CPE	Constant Phase Element
DC	direct (not necessarily current)
EEDF	Electron Energy Distribution Function
EEPF	Electron Energy Probability Function
FHP	Floating Harmonic Probe
IV	current-voltage
LED	Light Emitting Diode
LP	Langmuir probe
PDHAM	Phase Delay Harmonic Analysis Method
PTFE	Polytetrafluoroethylene
QCM	Quartz Crystal Microbalance
SEM	Scanning Electron Microscope

a	normalized AC voltage amplitude, see Eq. 1.48
$T_{e,i}$	electron and ion temperature, respectively
$n_{e,i}$	electron and ion number density, respectively
λ_D	Debye length
D_λ	Debye number
ω	angular frequency
$m_{e,i}$	mass of the electron and positive ion (argon), respectively
A_p	collecting surface area of the probe/substrate electrode
k_B	Boltzmann constant
e	elementary charge
C_s	sheath capacitance
C_f	film capacitance
C_B	capacitance of the DC blocking capacitor
C_p	parasitic capacitance
R_s	sheath resistance
R_f	film resistance
Z_s	sheath impedance
Z_f	film impedance
Z	impedance of the equivalent circuit
Z_m	measured impedance
Y	admittance
ε_r'	real part of the relative dielectric constant
ε_r''	negative imaginary part of the relative dielectric constant
σ	conductivity
tg δ	dielectric loss tangent
Q	parameter of CPE

$i_{n\omega}$	FHP n-th harmonic current
i_t	transient current
$I_{e,i}$	electron and ion current, respectively
V_p	probe potential
I_p	probe current
V_{fl}	floating potential
V_0	AC voltage amplitude
Φ	plasma potential
$\bar{V}$	mean FHP potential

List of author's publications

A) Publications in impacted journals

A1. M. Zanáška, Z. Turek, Z. Hubička, M. Čada, P. Kudrna and M. Tichý. Floating harmonic probe for diagnostic of pulsed discharges. *Surf. Coat. Technol.*, 357:879–885, 2019.

A2. M. Zanáška, Z. Hubička, M. Čada, P. Kudrna and M. Tichý. Floating harmonic probe measurements in the low-temperature plasma jet deposition system. *J. Phys. D-Appl. Phys.*, 51:025, 2018.

A3. M. Zanáška, J. Adámek, M. Peterka, P. Kudrna and M. Tichý. Comparative measurements of plasma potential with ball-pen and Langmuir probe in low-temperature magnetized plasma. *Phys. Plasmas.*, 22:033516, 2015.

B) Proceedings in conference books and contributions

B1. M. Zanáška, Z. Hubička, P. Kudrna, M. Čada and M. Tichý, In-situ measurement of capacitance of deposited dielectric thin films, in 19th International Congress on Plasma Physics (ICCP), Vancouver, Canada, Oral presentation, C08-111, 2018.

B2. M. Zanáška, Z. Hubička, M. Čada, P. Kudrna and M. Tichý, Floating harmonic probe measurements in the low-temperature plasma jet deposition system, in SVC TechCon, Orlando, USA, Oral presentation, 2018.

B3. M. Zanáška, Z. Hubička, Z. Turek, M. Čada, P. Kudrna and M. Tichý, Floating harmonic probe diagnostics in dc continuous and pulsed regimes, in 28th Symposium on Plasma Physics and Technology (SPPT), Prague, Czech Republic, Oral presentation, 2018.

B4. M. Zanáška, Z. Turek, Z. Hubička, M. Čada, P. Kudrna and M. Tichý, Floating Harmonic Probe for Diagnostics of Pulsed Discharges, in WDS'18 Proceedings of Contributed Papers — Physics (eds. J. Šafránková and J. Pavlů), Prague, Czech Republic, Matfyzpress, pp. 150–155, 2018.

B5. K. Tuharin, M. Zanaska, P. Kudrna, M. Tichy, Absorption Spectroscopy of Iron Oxide Films Prepared for Dye-sensitized Solar Cells, in WDS'18 Proceedings of Contributed Papers — Physics (eds. J. Šafránková and J. Pavlů), Prague, Czech Republic, Matfyzpress, pp. 130–134, 2018.

B6. M. Zanáška, Z. Hubička, Z. Turek, M. Čada, P. Kudrna and M. Tichý Floating harmonic probe diagnostics in DC continuous and pulsed regimes, in 18th International Balkan Workshop on Applied Physics, Book of abstracts (eds. R. Vladoiu, A. Mandes and W.D. Balan), Constanta, Romania, Ovidius University Press, pp. 78, 2018.

B7. M. Zanáška, Z. Hubička, P. Kudrna and M. Tichý, Floating harmonic probe measurements in the low-temperature plasma jet deposition system, in 12th Frontiers in Low Temperature Plasma Diagnostics (FLTPD), Zlatibor, Serbia, Oral presentation, pp. 14, 2017.

B8. M. Zanáška, K. Tuharin Z. Hubička, P. Kudrna, M. Čada and M. Tichý, Floating harmonic probe diagnostics during deposition of hematite thin films by hollow cathode sputtering system, in 8th International Workshop on Polymer Metal Nanocomposites, Prague, Czech Republic, Poster presentation, 2017.

B9. M. Zanáška, Z. Hubička, M. Čada, P. Kudrna and M. Tichý, Floating Harmonic Probe Measurements in the Low-Temperature Plasma Jet Deposition System, in WDS'17 Proceedings of Contributed Papers — Physics (eds. J. Šafránková and J. Pavlů), Prague, Czech Republic, Matfyzpress, pp. 82–87, 2017

B10. K. Tuharin, M. Zanaska, P. Kudrna and M. Tichy, Deposition of Iron Oxide Films by Plasma Jet Sputtering System for Dye-sensitized Solar Cell„ in WDS'17 Proceedings of Contributed Papers — Physics (eds. J. Šafránková and J. Pavlů), Prague,Czech Republic, Matfyzpress, pp. 76–81, 2017

B11. M. Zanáška, P. Kudrna and M. Tichý, The AC probes for diagnostics of processing plasmas, in 17th International Balkan Workshop on Applied Physics, Conference proceedings (eds. R. Vladoiu, A. Mandes and W.D. Balan), Constanta, Romania, Ovidius University Press, pp. 81–82, 2017.

B12. M. Zanáška, C. Denker, R. Hippler, H. Mohamad, C. Helm, M. Münzenberg, M. Medvidov and M. Delcea, Optimisation of Ion Beam Etching Process for Fabrication of CoFeB/MgO Magnetic Tunnel Junctions, in WDS'16 Proceedings of Contributed Papers — Physics (eds. J. Šafránková and J. Pavlů), Prague, Matfyzpress, pp. 150–154, 2016.

Attachments

1. M. Zanáška, Z. Turek, Z. Hubička, M. Čada, P. Kudrna and M. Tichý. Floating harmonic probe for diagnostic of pulsed discharges. *Surf. Coat. Technol.*, 357:879–885, 2019.

2. M. Zanáška, Z. Hubička, M. Čada, P. Kudrna and M. Tichý. Floating harmonic probe measurements in the low-temperature plasma jet deposition system. *J. Phys. D-Appl. Phys.*, 51:025, 2018.